Bias Spectroscopy of Coulomb Drag Between Vertically Integrated Quantum Wires

Frédérik Poitevin

Department of Physics
McGill University
Montréal, Québéc, Canada

March 25, 2026

A thesis submitted to McGill University in partial
fulfillment of the requirements of the degree of
Doctor of Philosophy

“Don’t drink and drag.”

– Guillaume Gervais

Acknowledgements

None of this work would have been possible without the unwavering support, encouragement, and expertise of my supervisor, Guillaume Gervais. I am deeply grateful to him for placing his trust in me, notably by allowing me to conduct research at Sandia National Laboratories — a formative experience that extended far beyond physics. Working with Guillaume has been intellectually enriching and personally transformative. Among his many admirable qualities, I particularly value his candid honesty. From the outset of our discussions on the Coulomb drag project, he was forthright about its complexity, describing it as one of his most challenging endeavors. He was not wrong. Yet, through perseverance and his guidance, I am proud of what we have accomplished together. I cannot thank Guillaume enough for his mentorship and for believing in me throughout this journey.

I would also like to express my sincere gratitude to Mike Lilly, our collaborator at Sandia National Laboratories, without whom this project would simply not exist. Despite his demanding schedule, Mike consistently made time to meet with us and provided invaluable insights that helped us navigate the many challenges we encountered along the way.

I am also grateful to Dominique Laroche, my predecessor on this project, whose foundational work greatly facilitated my own. His enthusiasm and willingness to discuss the intricacies of the experiment were both helpful and motivating, making it much easier for me to get started.

Throughout my Ph.D., I benefited immensely from the outstanding technical support provided by staff at both McGill University and Sandia National Laboratories. At McGill, I would like to extend special thanks to Richard Talbot for his assistance with technical drawings, Robert Gagnon for his expertise in materials, John Smeros for maintaining and servicing the equipment essential to this project, and Pascal Bourseguin for his skilled machining work. At Sandia National Laboratories, I was fortunate to receive support from a wide range of technical staff. While the list of individuals is too long to include here, I am sincerely grateful for the help I received. Work at McGill or Sandia National Laboratories would be impossible without these technical personnel.

Working long hours in a basement laboratory can sometimes be psychologically challenging, but I was fortunate to be surrounded by exceptional colleagues who made the experience both enjoyable and rewarding. I would like to thank Sujatha Vijayakrishnan, Matei Petrescu, Oulin Yu, Talia Martz-Oberlander, Frédéric Boisvin, Zachary Berkson-Korenberg, and Nick Wicklund for their friendship, support, and for making it so much more enjoyable to do the amazing work we do in this laboratory.

Finally, I would not have been able to complete this work without the support of my incredible friends and family. I am especially grateful to Jennifer Brulé, my significant other, for her patience, for listening so attentively, and for standing by me throughout this long journey. Thank you to Jean Lavoie for the many thoughtful discussions, timely distractions, and for encouraging me to broaden my intellectual horizons. And most importantly, thank you to my parents for always believing in me and for supporting me through every step of my unconventional path.

Abstract

Contrary to common intuition, reducing the dimensionality of a physical system often enriches its underlying physics. This is especially true in quantum mechanical systems, where exotic phases of condensed matter emerge, such as Luttinger liquids, fractional quantum Hall states, and Wigner crystals. Recent studies on systems previously used to investigate interacting Luttinger liquids have shown nonreciprocal behaviour in Coulomb drag measurements, suggesting contributions beyond Luttinger physics.

This thesis explores the complex interplay of electron interactions in Luttinger liquids through the eye of Coulomb drag between vertically integrated quantum wires. The experimental platform developed for this study includes a custom-designed low-temperature sample holder and a dry dilution cryostat. The fabrication of the quantum wire devices was updated to new tools and cleanroom regulations at the Center for Integrated Nanotechnologies. Initial work focused on reproducing reciprocal drag signals observed in earlier work, but most devices showed nonreciprocal behavior. This led to the development of bias spectroscopy techniques to characterize the subband structure and the drag signal. These measurements revealed that reciprocity could be improved by applying an appropriate bias, suggesting the presence of a nonlinear rectification-induced voltage component in the system.

Abrégé

Bien que l'on cherche souvent à réduire la dimensionnalité d'un problème physique pour en simplifier l'analyse, la physique en basse dimension s'avère parfois plus riche et plus surprenante que celle en trois dimensions. C'est notamment le cas en mécanique quantique, où émergent des états impossibles à observer en trois dimensions, tels que le liquide de Luttinger, l'effet Hall fractionnaire ou encore les cristaux de Wigner. Des résultats récents obtenus avec des dispositifs conçus pour étudier les interactions entre liquides de Luttinger ont mis en évidence un comportement non réciproque de la traînée de Coulomb, suggérant que le système ne se comporte pas comme une paire idéale de liquides de Luttinger.

Cette thèse explore les interactions électroniques dans les liquides de Luttinger à l'aide de la traînée de Coulomb entre deux fils quantiques intégrés verticalement dans une hétérostructure d'arséniure de gallium. L'étude a été réalisée à l'aide d'un cryostat à dilution *sec* et d'un support d'échantillon conçu sur mesure. La fabrication des dispositifs a dû être adaptée aux nouvelles réglementations et aux outils disponibles au *Center for Integrated Nanotechnologies.* Les travaux ont débuté par des tentatives de reproduction des mesures de traînée de Coulomb précédemment obtenues avec des dispositifs similaires. Toutefois, les résultats se sont révélés incompatibles avec les relations de réciprocité. Des techniques de spectroscopie de biais ont alors été employées afin de mieux caractériser la structure des sous-bandes des fils quantiques. Ces techniques ont ensuite été adaptées pour réaliser une mesure spectroscopique de biais de la traînée de Coulomb, révélant que les relations de réciprocité pouvaient être partiellement restaurées par l'application d'un biais approprié. Dans

l'ensemble, les données recueillies suggèrent qu'un mécanisme de compensation du voltage induit par la rectification non linéaire résulte de l'application du biais.

Contributions and Statement of Originality

This thesis presents original contributions to the field of low-temperature condensed matter physics. Prior research on Coulomb drag between quantum wires is also reviewed. The author's specific contributions are outlined below:

- *Commissioning of a dilution cryostat fitted with a tri-axis vector magnet and custom-made support and pumping system:* Upon joining Professor Guillaume Gervais's laboratory, the author (FP) contributed to the implementation of a newly awarded Canada Foundation for Innovation grant, which funded the acquisition of a dry dilution cryostat equipped with a tri-axis magnet. FP was tasked with designing a mechanical support frame to accommodate the new cryostat, replacing an obsolete wet cryostat system. Due to fundamental differences in operational requirements between the two systems, significant ingenuity was required to adapt the new hardware to the existing infrastructure. Under the supervision of Prof. Gervais, FP designed and constructed a robust support frame and custom pumping system that minimized vibration transmission and ensured stable operation of the cryogenic system.
- *Design and implementation of a custom low temperature sample holder:* FP designed and implemented a custom modular sample holder optimized for low-temperature quantum transport measurements. The new cryostat, equipped with a tri-axis magnet, required a sample mounting solution compatible with

its geometry, electrical, and thermal constraints. The design accounted for mechanical stability, thermal anchoring, and electrical connectivity, while minimizing vibrational coupling. The sample holder was fabricated and integrated into the cryogenic system with a modular architecture, enabling both reliable measurements of quantum devices and easy interchangeability with other experimental setups. This contribution was carried out under the supervision of Prof. Guillaume Gervais and represents an original engineering solution tailored to the specific needs of the experimental setup.

- *Adaptation of the Coulomb drag fabrication to the new tool and regulation at the Center for Integrated Nano Technologies (CINT):* The fabrication process for Coulomb drag devices was adapted by FP, with the help of the technical staff at CINT, to comply with the capabilities of newly acquired equipment and the regulatory framework. This involved modifying existing lithography procedures to align with the specifications of the new fabrication tools. Additionally, FP navigated and implemented procedural changes required by CINT's cleanroom standards and safety regulations. These adaptations enabled the successful production of high-quality quantum wire devices suitable for low-temperature drag measurements, representing a significant technical contribution to the experimental workflow.

- *Bias spectroscopy characterization of the subband structure of two vertically integrated quantum wires:* FP performed bias spectroscopy measurements to characterize the subband structure of the two vertically integrated quantum wires. These measurements provided detailed insight into the linearity and occupancy of the subbands, which are critical for understanding interwire interactions and Coulomb drag phenomena. The experimental setup required precise control of gate voltages and bias conditions to resolve the subband features in both layers independently. Zachary Berkson-Korenberg (ZBK) contributed to the development of Python-based control routines used to operate the instrumentation and automate the measurement process. The results demonstrated clear subband quantization and enabled the identification of regimes suitable for drag measurements. This characterization represents a key contribution to the understanding of quantum wire behavior in vertically coupled systems.

- *First bias spectroscopy characterization of the Coulomb drag between vertically integrated quantum wires:* Under the supervision of Prof. Gervais, the author carried out the first bias spectroscopy characterization of Coulomb drag between vertically integrated quantum wires and discovered that the reciprocity relation could be improved. The exact mechanism for reciprocity improvement under DC current bias remains to be explained, but a compensation mechanism in which the DC bias cancels the nonlinear rectification effects is suspected. This work represents a pioneering contribution to the experimental investigation of Coulomb drag in vertically coupled quantum wires, and a manuscript is in preparation.

Contents

List of Figures

List of Abbreviations

QW	Quantum wire
1D	One-dimension
2D	Two-dimension
3D	Three-dimension
2DEG	Two-dimensional electron gas
SdH	Shubnikov-de Haas
MBE	Molecular beam epitaxy
QPC	Quantum point contact
PT1	Pulse tube plate 1
PT2	Pulse tube plate 2
MC	Mixing chamber
JT	Joule-Thompson
RTD	Resistive temperature detector
PID	Proportional integral derivative
SNL	Sandia national laboratories
CINT	Center for integrated nanotechnologies
EBASE	Epoxy bond and stop-etch
e-beam	Electron-beam
SEM	Scanning electron microscopy
TPO	Top pinch-off gate
BPO	Bottom pinch-off gate
TPL	Top plunger gate
BPL	Bottom plunger gate

1

Introduction

1.1 Introduction

One-dimensional (1D) systems may appear deceptively simple — particles are constrained to move along a single spatial direction. At first glance, this might seem unremarkable. However, real-world 1D systems composed of interacting electrons are, in fact, rich and intricate, offering deep insights both theoretically and experimentally. The theoretical description of an infinitely long 1D system of electrons is known as a Luttinger liquid. In a Luttinger liquid, electrons strongly interact with one another because they cannot pass through each other. As a result, they do not behave as individual particles but instead move collectively as waves. More specifically, they propagate as separate waves of spin and charge — a phenomenon known as spin-charge separation.

In low-dimension physics, symmetry principles govern the behavior of quasiparticles and determine the measurable transport properties. One such principle is the reciprocity relation, which arises from time-reversal symmetry and microscopic reversibility. In the context of Coulomb drag — a proximity effect happening between low-dimensional systems — reciprocity relations dictate that the drag signal should remain invariant when the roles of the drive and drag wires are exchanged or when the direction of the drive current is inverted, provided the system remains in equilibrium and no symmetry-breaking mechanisms are present. Deviations from these relations can signal the presence of non-equilibrium effects, nonlinear rectification, or Wigner crystallization. The study of proximity effects between Luttinger liquids is not only of academic interest but also holds long-term commercial relevance. As electronic devices continue to miniaturize and integrated circuits grow in complexity, these effects will eventually become non-negligible in practical applications.

The primary motivation behind the work presented in this thesis was to investigate thermal drag between Luttinger liquids using vertically integrated quantum wires (QW). The initial objective was to reproduce the reciprocal drag signal previously observed by my predecessor on this project. This proved to be a significant challenge, as most devices consistently exhibited nonreciprocal drag signals. In an effort to better characterize the QWs, bias spectroscopy measurements of conductance were performed. This led to the idea of applying a similar spectroscopic approach to the drag signal itself. The hypothesis was that reciprocity might be broken due to a directional voltage arising from nonlinear rectification, and that applying a bias could potentially counteract this effect. Through a combination of careful experimentation and a bit of serendipity, it was discovered that reciprocity could indeed be improved by tuning the applied bias appropriately.

1.2 Thesis Outline

This thesis summarizes the work that led to the observation of bias-dependent reciprocity in Coulomb drag between vertically integrated QWs, along with the relevant technical and experimental contributions made throughout the project. It begins by introducing, in Chapter 2, the key theoretical concepts necessary to understand the main results, and reviews relevant prior work in the field. Chapter 3 details the commissioning of the dry dilution cryostat used in this work. Chapter 4 outlines the fabrication process of the vertically integrated QW platform, with emphasis on the modifications made to the original recipe developed by my predecessor. The low-temperature characterization of the devices is presented in Chapter 5, followed by the main experimental results on bias spectroscopy of Coulomb drag in Chapter 6. Finally, Chapter 7 concludes the thesis and discusses some of the many potential future directions.

2

Theory and Background

Coulomb drag between quantum wires (QWs) is a rich and intricate phenomenon, presenting significant challenges for both experimental investigation and theoretical modeling. This chapter introduces the background and theoretical framework necessary to understand the work presented herein. It begins by laying out the fundamental concepts of low-dimensional physics. The discussion then turns to quantum transport in one-dimensional (1D) constrictions, presented from both conceptual and historical perspectives. Finally, the chapter outlines the theoretical foundations of Coulomb drag in 1D systems, accompanied by a brief review of the key experimental studies conducted to date.

2.1 Low-Dimensional Systems

One of the most pragmatic motivations for investigating low-dimensional systems — beyond pure scientific curiosity — has been the relentless drive toward the miniaturization of electronic devices. A decade after the invention of the transistor in 1947 [1], Jack Kilby developed the first integrated circuit during his first year at Texas Instruments, as part of an effort to reduce the size of electrical circuits [2]. This innovation marked the beginning of what would later be known as Moore's law, which predicted that the complexity of integrated circuits — typically measured by the number of transistors per chip — would double approximately every year; a trend that has mostly held for decades.

Contemporary research on low-dimensional systems is largely focused on two-dimensional electron gases (2DEGs) formed in semiconductor heterostructures. However, several alternative platforms have proven equally compelling for realizing low-dimensional physics. These include atomically thin materials such as graphene [3], surface states in topological insulators[1] [4], and cold atom systems in optical lattices [5]. Notably, the first experimental realization of a 2DEG did not occur in semiconductors or integrated circuits, but rather on the surface of liquid helium [6], underscoring the diversity of physical systems in which low-dimensional behavior can emerge.

A central motivation for studying low-dimensional systems is to elucidate the role of particle interactions. As dimensionality is reduced, particles become increasingly confined, thereby amplifying the effects of interactions[2]. In semiconductor-

---

[1] Although most implementations rely on integrated circuits, such systems could, in principle, be realized without them.

[2] This enhancement arises because the available phase space for scattering diminishes with reduced dimensionality, forcing particles into closer proximity and enhancing the role of interactions.

based systems, the relevant particles are electrons[3], and electron–electron interactions in two-dimensions (2D) give rise to a rich variety of exotic quantum phases in mesoscopic regimes. Notable examples include Luttinger liquids[4] [7], fractional quantum Hall states [8–10], and Wigner crystals [11]. Additionally, superconductivity in 2D — only recently observed — exhibits profound differences from its three-dimensions (3D) counterpart [12, 13].

2.1.1 Fermi Liquid Theory and Landau Levels in Magnetic Fields

Fermi liquid theory[5] was developed by Landau in 1957. The ingenuity of this theory lies in the realization that the low-energy excitations of an interacting fermionic system behave as emergent quasiparticles with an effective mass[6], m^*, which mimic the behavior of a free electron gas. In GaAs, $m^* = 0.067\,m_e$, where m_e is the free electron mass. The Fermi liquid model generally holds for excitation energies satisfying $T \ll E_F/k_B \sim 70\,\mathrm{K}$, provided that interactions do not induce symmetry-breaking ground states or phase transitions.

The different Fermi parameters of a typical 2DEG formed in an AlGaAs heterostructure used in the present work are given in Table 2.1. Fermi liquid theory is particularly useful for describing the qualitative behavior of a 2DEG in the absence of a magnetic field. When a magnetic field is applied, the energy of the electrons becomes quantized into discrete values known as Landau levels, given by $E_N = \hbar\omega_c(N + 1/2)$, with $N \in \mathbb{N}$ and where $\omega_c = eB/m^*$ is the cyclotron frequency.

---

[3] In semiconductors, electrical conduction can also occur via the propagation of holes, which represent the absence of electrons in the valence band. This phenomenon arises through the process of doping, whereby impurity atoms are introduced into the semiconductor lattice to modulate its electronic properties. Depending on the type of dopant, either electrons (n-type) or holes (p-type) become the dominant charge carriers.

[4] The Luttinger liquid is one of the few many-body systems that admits an exact analytical solution.

[5] Fermi liquids are mathematical descriptions of 2DEGs that include interactions. Without interactions, the 2DEG is described as a Fermi gas.

[6] The effective mass is a tensor, but in isotropic cases near an energy minima, it can be approximated as a scalar.

2DEG Property	**Symbol**	**Value**
Effective mass	m^*	$0.067m_e$
Spin degeneracy	g_s	2
Valley degeneracy	g_v	1
Dielectric constant	ϵ	$13.1\epsilon_0$
Effective Lande g-factor	g^*	-0.44
Density of states	$g(E) = g_s g_v (m^*/2\pi\hbar^2)$	2.8×10^{10} cm^{-2} meV^{-1}
Level spacing	$1/g(E)$	3.57 μeV μm^2
Fermi wave vector	$k_F = \sqrt{4\pi n_e/g_s g_v}$	1.04×10^8 m^{-1}
Fermi energy	$E_F = (\hbar k_F)^2/2m^*$	6.18 meV (or $T_F = 71.7$K)
Fermi wavelength	$\lambda_F = 2\pi/k_F$	60.3 nm
Fermi velocity	$v_F = \hbar k_F/m^*$	1.8×10^5 m/s
Scattering time	$\tau = m^*\mu_e/e$	30.4 ps
Mean free path	$l = v_F\tau$	5.48 μm
Resistivity	$\rho = (n_e e\mu_e)^{-1}$	45 Ω per square
Diffusion constant	$D = v_F^2\tau/2$	0.494 m$^2/s$

Table 2.1: Parameters for a 2DEG formed in GaAs with $n_e = 1.73 \times 10^{11}$ cm^{-2} and $\mu_e = 798\,484$ cm^2/sV. Here, $e = 1.602 \times 10^{-19}$ C is the elementary charge of the electron, $k_B = 1.381 \times 10^{-23}$ J/K is the Boltzmann constant, $\epsilon_0 = 8.9 \times 10^{-12}$ F/m is the vacuum permittivity, $\hbar = 1.05 \times 10^{-34}$ Js is the reduced Planck constant, and $m_e = 9.11 \times 10^{-31}$ kg is the electron mass. Adapted from Refs. [14, 15].

In weak magnetic fields[7], these Landau levels can be treated as a perturbation, allowing Fermi liquid theory to remain applicable. In this regime, one can show that the number of states per Landau level, known as the Landau level degeneracy, is $g_{LL} = eB/h = 2\pi eB/\hbar$.

Experimentally, these Landau levels manifest as Shubnikov–de Haas (SdH) oscillations in the measured resistance of a 2DEG, as shown in Fig. 5.1. The filling factor ν, corresponding to magnetic fields B_ν at which an integer number of Landau levels are filled, is defined as

$$\nu = \frac{n_e h}{B_\nu e}, \quad \text{for } \nu \in \mathbb{N}. \tag{2.1}$$

---

[7] At higher magnetic fields, the field can no longer be treated as a perturbation, and non-Fermi liquid states begin to emerge. The high-field regime gives rise to many interesting phenomena such as the quantum Hall effect, the emergence of edge states, and fractional statistics, which are beyond the scope of the present work.

Since $\nu \in \mathbb{N}$, the spacing between any two consecutive Landau levels is exactly one:

$$\Delta\nu = (\nu+1) - \nu = 1 = \frac{n_e h}{B_{(\nu+1)} e} - \frac{n_e h}{B_\nu e} = \frac{n_e h}{e}\left(\frac{1}{B_{(\nu+1)}} - \frac{1}{B_\nu}\right).$$

This relation can be used to express the electron density of the 2DEG as a function of the spacing between two adjacent minima in resistance, plotted in units of $1/B$, as

$$n_e = \frac{1}{(1/B_{(\nu+1)} - 1/B_\nu)}\frac{e}{h} = \frac{1}{\Delta\left(1/B_\nu\right)}\frac{e}{h} = f_B\frac{e}{h}, \tag{2.2}$$

where $\Delta(1/B_\nu)$ is the period of the SdH oscillations in $1/B$, and f_B is the corresponding oscillation frequency in $1/B$. This enables a direct measurement of the electron density in the 2DEG.

2.1.2 Requirement for the 2D Mesoscopic System

One way to confine electrons to 2D is to engineer the electrical potential experienced by the electrons in one of the three spatial dimensions, such that it forms a potential well. Electrons will be trapped in this well if their Fermi energy[8], E_F, is smaller than the height of the potential barrier, and if the well width is smaller than the Fermi wavelength of the electrons[9], λ_F.

If the conduction band of the material (solid black line in Fig. 2.1) dips below E_F, electron motion is restricted in that direction to discrete energy levels. If the energy separation between these levels is sufficiently large, electrons will predominantly occupy the ground state, effectively freezing out motion in that direction[10].

Molecular beam epitaxy (MBE) is a powerful technique for achieving such con-

---

[8] The Fermi energy is the highest energy level occupied by electrons at absolute zero temperature in a system of fermions, such as electrons in a metal or semiconductor. At finite temperatures, electrons near the Fermi energy can be thermally excited to higher energy levels. The Fermi energy depends on the density of charge carriers and their effective mass.

[9] The Fermi wavelength is a quantum mechanical property that characterizes the wavelength of electrons at the Fermi energy in a material. It depends on the density of charge carriers.

[10] With the electron densities used in this work, the second subband of the potential well lies roughly 150 meV above the first. This gap is much larger than the measurement temperature $Tk_B \leq (1.5\ \text{K})k_b = 0.129$ meV, and much larger than the source-drain bias $eV_{sd} \leq 4$ meV.

finement. As illustrated in Fig. 2.1, by growing alternating layers of doped semiconductors, one can engineer the conduction band profile to form a potential well. The conduction electrons then appear to be confined within this well.

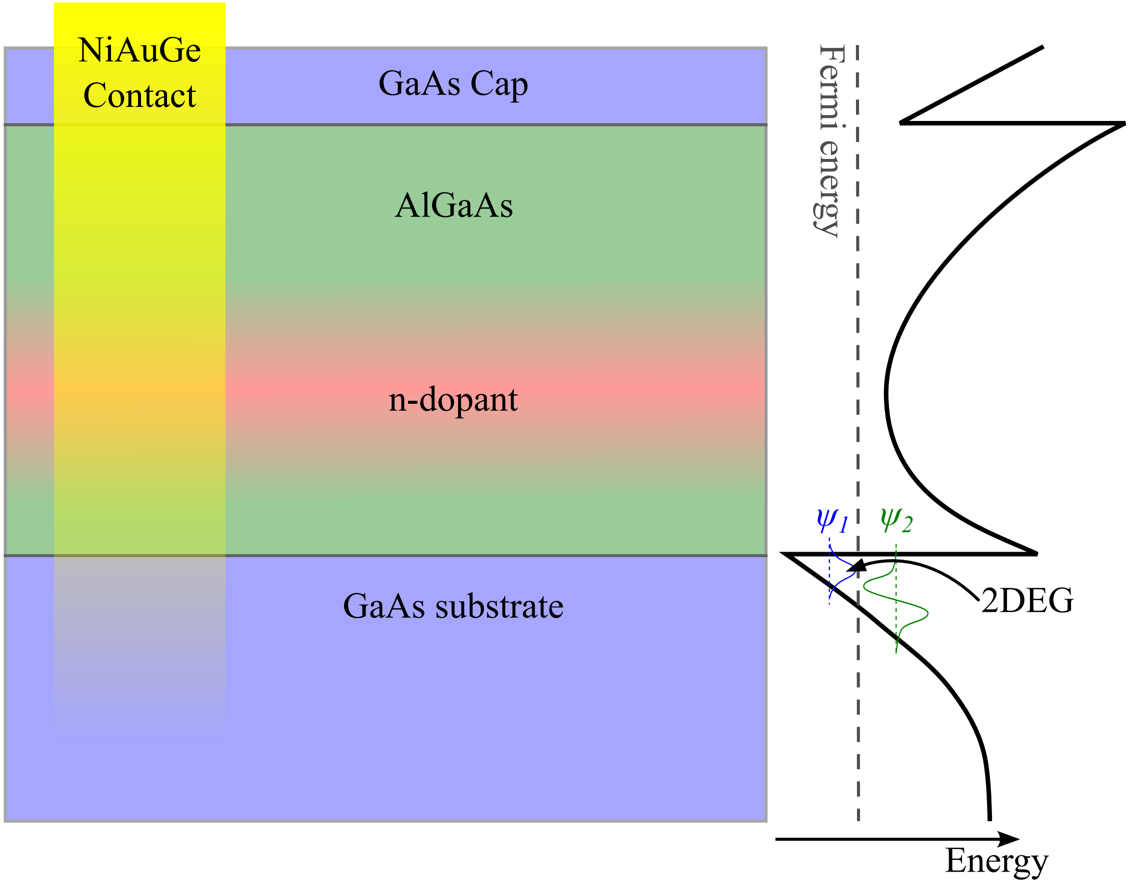

Figure 2.1: A cross-sectional diagram of a GaAs/AlGaAs heterostructure grown by MBE (left) and potential landscape diagram showing the conduction band profile and the location of the 2DEG (right). Adapted from Ref. [14].

Mesoscopic systems are characterized by their small size — large enough to exhibit collective behavior, yet small enough for quantum effects to dominate. To observe such effects, the system must be smaller than the electron phase coherence length, L_ϕ, which is the distance over which the electron's phase remains coherent. The primary sources of phase decoherence include electron–phonon interactions (which are strongly temperature-dependent), magnetic impurities, external electromagnetic noise, certain electron–electron interactions (*e.g.*, inelastic scattering), and charge fluctuations or two-level systems [16,17]. At low temperatures, and in devices like those used in this work, L_ϕ can easily exceed 20 microns. L_ϕ can be measured using ballistic weak localization as described in Ref. [18].

As mentioned above, the relative strength of electron–electron interactions in a system significantly influences its physical behavior. A common measure of the importance of these interactions is the ratio of the Coulomb interaction potential energy[11] between two electrons separated by a distance r, $E_{Pot} = e^2/4\pi\epsilon r$, to the kinetic energy of the electrons, $E_K = m^* v_F^2/2 = \hbar^2 \pi n_e/m^*$. This ratio is usually expressed as a dimensionless parameter known as the gas parameter[12],

$$r_s = \frac{E_{Pot}}{E_K} = \frac{e^2/4\pi\epsilon r}{\hbar^2/m^* r^2} = \frac{r}{4\pi\epsilon\hbar^2/e^2 m^*} = \frac{r}{a^*_{Bohr}}, \tag{2.3}$$

where r_s is the ratio of the average inter-electron spacing over the effective Bohr radius for the material, defined as $a^*_{Bohr} = 4\pi\epsilon\hbar^2/m^* e^2$. In high-density 2DEGs, the kinetic energy is large, resulting in $r_s \ll 1$, and interactions can be treated as perturbations to the kinetic energy. In contrast, in low-density 2DEGs, the kinetic energy is small and interactions dominate, leading to $r_s \gg 1$. In this regime, electrons may even form a lattice-like structure known as a Wigner crystal [19]. For a 2DEG with the properties listed in Table 2.1, $r_s = 1.3$, indicating that interactions are significant in mesoscopic devices fabricated from this 2DEG, though not strong enough to induce Wigner crystallization [14].

2.2 Quantum Transport in 1D Constrictions

Since the experimental study of electronic transport through 1D constrictions was first proposed in 1965 by Y. V. Sharvin [20], this field has consistently attracted significant attention [21]. A landmark moment occurred in 1988, when two inde-

---

[11] Although the 2DEG is a 2D system, the interaction potential is often modeled using the 3D Coulomb potential. This is because the electric field lines from an electron extend into the third dimension, resulting in interactions governed by the 3D Coulomb potential rather than a strictly 2D one.

[12] In a 2DEG with charge carrier density n_e, the average inter-electron spacing is $r = 1/\sqrt{\pi n_e}$, allowing the kinetic energy to be rewritten as $E_K = \hbar^2/m^* r^2$.

pendent research groups simultaneously reported the quantization of conductance in quantum point contacts[13] (QPCs) [22, 23]. Their results are shown in Fig. 2.2. At the time, it was still debated whether a ballistic QW[14] (*i.e.*, one free of impurities) would exhibit any resistance at all [24, 25]. The discovery of quantized conductance in such systems sparked widespread interest and firmly established the importance of this geometry[15].

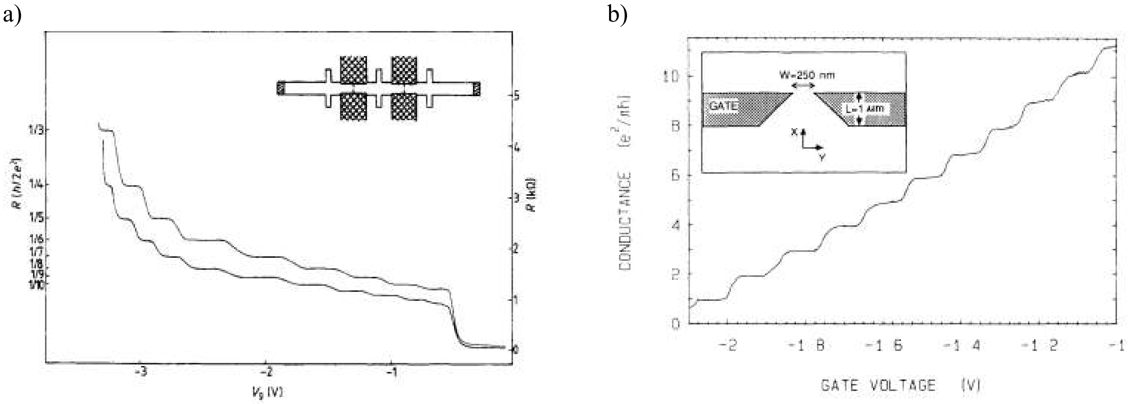

Figure 2.2: Quantized conductance discovery. a) Data from Ritchie's group [22]. b) Data from Kouwenhoven's group [23].

Since then, analogues of quantized conductance have been observed in various domains: the optical analogue involving photons [27], the superconducting analogue involving Cooper pairs [28], and the thermal analogue [29]. While the optical and thermal analogues are well-established, the superconducting case is relatively recent and still requires further statistical investigation across large arrays of devices to conclusively determine the origin of the observed effect.

Perhaps one of the most unexpected sources of excitement surrounding QPCs and QWs was the discovery of the mysterious 0.7 structure — a conductance plateau appearing near $0.7 \times 2e^2/h$, just below the first quantized conductance plateau. Although formally studied in 1996 [30], traces of this anomaly were visible in earlier work.

---

[13] QPCs are shaped like narrow constrictions that pinch the electron flow.

[14] QWs are elongated versions of QPCs, shaped like narrow channels that guide electrons.

[15] An elegant study investigating the influence of gate geometry and wire length on the conductance of 1D constrictions in GaAs heterostructures was conducted in 2022 [26].

Adding to the intrigue, another anomaly known as the zero-bias anomaly often appears in transconductance measurements under a finite DC source-drain bias when the 0.7 structure is present. Despite nearly three decades of investigation, neither of these QW anomalies has a definitive theoretical explanation. No single model has emerged as universally accepted, and the topic remains an active area of theoretical research. However, there is broad consensus that both effects arise from many-body physics, specifically electron–electron interactions [31].

Other exotic phenomena have also been explored in QWs, including charge fractionalization [32], spin–charge separation [33], and correlated-electron insulating states resembling Wigner crystals [34, 35]. More recently, researchers have begun using QWs to construct more complex devices — similar to those used in this work — to study systems of interacting electrons, such as Coulomb drag, as demonstrated here and in Refs. [36, 38–46].

QWs have also garnered significant attention due to their potential to host Majorana zero modes — non-Abelian quasiparticles that are topologically protected from noise and decoherence. This property forms the foundation of fault-tolerant topological quantum computing [47], making QWs a promising platform for future quantum technologies.

2.2.1 Quantized Conductance and Subbands

When the electrons in a 2DEG are further confined by an additional perpendicular potential well — such as one created by depletion gates on the surface of the heterostructure — a QPC or QW can be formed, depending on the length of the confinement in the third (and final) spatial dimension. In this newly confined direction, a situation analogous to the original 2DEG arises: the electron motion becomes quantized into discrete energy levels. This is illustrated at the top of Fig. 2.3, where two 2DEG reservoirs (source and drain) are connected by a confined conduction region.

As the confining potential narrows the width of the conduction channel[16], quantized conduction emerges. If the confinement in the 2DEG is along the z-direction and the QPC potential is modeled as a parabolic potential[17], $V(x) = 1/2m^*\omega_0^2x^2$, along the x-direction, then the energy levels are given by

$$E_n = (n - 1/2)\hbar\omega_0 + \frac{\hbar^2 k_y^2}{2m^*}, \quad \text{for } n \in \mathbb{N}, \tag{2.4}$$

where k_y is the wave vector along the remaining unconfined y-direction[18], and n is the subband number. The velocity of electrons in each subband is then given by

$$v_n = \frac{1}{\hbar}\frac{\mathrm{d}E_n}{\mathrm{d}k_y}. \tag{2.5}$$

Following the formalism developed by Landauer and Büttiker [50], applying a voltage V_{SD} between the source and drain reservoirs results in a chemical potential difference $\mu_S - \mu_D = eV_{SD}$. At zero temperature, the current through the quantum constriction is given by

$$I = \frac{e}{2}\sum_{n=1}^{N}\int_{\mu_D}^{\mu_S} g_n^{(1D)}(E)v_n(E)T_n(E)\mathrm{d}E, \tag{2.6}$$

where $g_n^{(1D)}(E)$ is the 1D density of states and $T_n(E)$ is the transmission probability for the $\mathrm{n^{th}}$ subband. The quantization of conductance arises from the fact that in one dimension, the density of states $g_n^{(1D)}(E) = 2/\pi(\mathrm{d}E_n/\mathrm{d}k_y)^{-1}$ and velocity (Eq. 2.5) cancel each other's energy dependence, leaving only the transmission probability $T_n(E)$ inside the integral [14]. For small source-drain bias V_{SD}, this transmission probability will be dominated by the transmission probability at the Fermi energy,

---

[16] In the first subband, the width of the conduction channel is approximately half the Fermi wavelength λ_F of the electrons in the original 2DEG. For a 2DEG like the one described in Table 2.1, this width is roughly 30 nm.

[17] Parabolic potentials are commonly used to illustrate energy quantization in 1D constrictions, although quantization occurs for any confining potential [48].

[18] The potential along the y-direction, which describes the transition from the 2DEG reservoirs to the confined region, can be neglected if the transition is adiabatic, that is, sufficiently smooth [49].

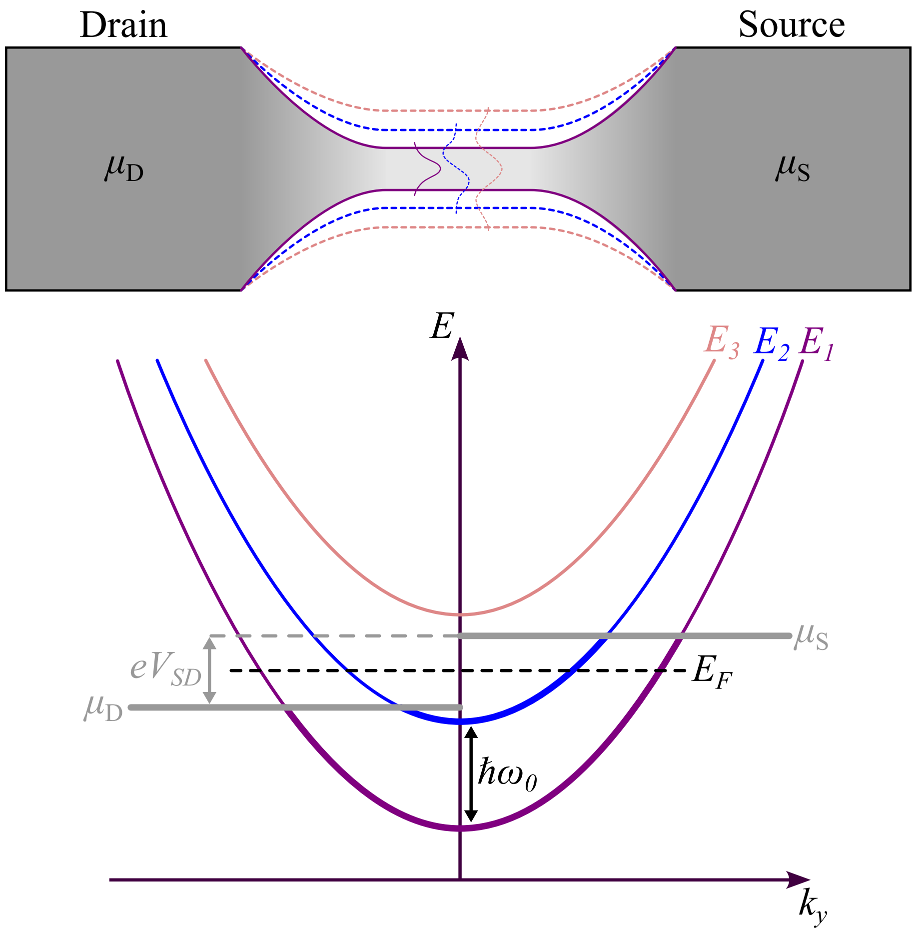

Figure 2.3: Schematic representation of a tunable-width 1D quantum constriction (top) and the corresponding energy dispersion relations for the first three subbands (bottom). The adiabatic (smooth) transition regions connecting the 2DEG source and drain reservoirs to the quantum constriction are shown. The first, second, and third subbands are represented in purple, blue, and pink, respectively. Each subband appears when the width of the wire increases by approximately half a Fermi wavelength relative to the previous one. Electrons in the reservoirs fill the available states in the wire (bold lines) up to the chemical potential of the corresponding reservoir (gray lines). The energy dispersion shown corresponds to a case where the constriction is wide enough to allow two subbands (purple and blue) to contribute to conduction. The current arises from the imbalance of occupied states in the energy interval $\mu_S - \mu_D$. With the source chemical potential higher than that of the drain, electrons flow from the drain to the source, resulting in a net current from the source to the drain.

yielding

$$I = \frac{2e}{h}(\mu_S - \mu_D)\sum_{n=1}^{N} T_n(E_F). \tag{2.7}$$

From this equation for the current through a 1D constriction, the famous Landau-

Büttiker formula for conductance G can be obtained by noting that $G = I/V_{SD} = eI/(\mu_S - \mu_D)$. The Landau-Büttiker formula is then

$$G = \frac{2e^2}{h}\sum_{n=1}^{N} T_n(E_F), \tag{2.8}$$

and for ballistic transport[19], the transmission probability for each subband is unity, *i.e.* $T_n(E_F) = 1$, leading to

$$G = \frac{2e^2}{h}N. \tag{2.9}$$

The fact that conductance in a ballistic 1D constriction is quantized is far from trivial. In a perfectly ballistic system, the constriction itself exhibits no intrinsic resistance. Instead, the quantized conductance arises from the scattering processes that equilibrate left- and right-moving electrons in the wire with the local chemical potentials of the source and drain reservoirs. In this sense, the quantized conductance is better understood as a form of contact resistance rather than resistance within the wire itself. This interpretation has been confirmed through four-terminal resistance measurements of QWs, which isolate the intrinsic resistance of the constriction from that of the contacts [51].

Just as in a 2DEG, the relative strength of the electron-electron interaction in a 1D system can be estimated using its 1D gas parameter:

$$r_s^{(1D)} = \frac{1}{2n_e^{(1D)} a^*_{Bohr}}, \tag{2.10}$$

where $n_e^{(1D)} \approx n_e W = n_e \lambda_F/2 = \sqrt{\pi n_e/2}$, for a ballistic constrictions in the first subband[20] [11,53,54]. For a 1D constriction defined in a 2DEG with the parameters listed in Table 2.1, the gas parameter for the first subband is approximately $r_s^{(1D)} \approx 0.92$. Wigner crystallization is expected to affect the Coulomb drag signal — the

---

[19] Ballistic transport refers to a regime in which electron backscattering from impurities or defects is negligible.

[20] Adding the second subband conduction increases the electron density in the wire by approximately 70% [52], further decreasing $r_s^{(1D)}$.

main experimental observable of this thesis, introduced later in this chapter — when $r_s^{(1D)} \geq 4$, which is not the case here [55].

Finally, it is essential to note that current through 1D constrictions is not constant in time. The measured conductance only probes the time-average of the fluctuating current [21]. These fluctuations are due to the discrete nature of the charge carriers and lead to a measurable characteristic power spectrum of shot noise, which varies with the occupancy of 1D subbands [56]. They are also the basis for the charge fluctuation model of Coulomb drag discussed in Sec. 2.3.3.

2.2.2 Biased 1D Constrictions

Bias spectroscopy measurements of 1D constrictions provide valuable insight into the transition from linear to nonlinear transport regimes. Although such measurements have become relatively common in condensed matter physics, their initial application to 1D constrictions in 2000 [57, 58] revealed an unexpected feature: a pronounced peak at zero bias, located below the first subband. This feature, illustrated in Fig. 2.4, became known as the zero-bias anomaly (ZBA). By that time, the so-called 0.7 structure had already been the subject of extensive investigation by several research groups. However, it was only through DC bias-dependent conductance measurements that the ZBA could be clearly identified. A comprehensive discussion of the ZBA and nonlinear transport in 1D constrictions can be found in Refs. [31, 59].

Bias spectroscopy measurements are now widely used to characterize 1D constrictions. They enable a comprehensive evaluation of the subband structure in both linear and nonlinear transport regimes, as well as provide additional insights into the system's electronic properties. Fig. 2.4 illustrates the underlying physics of such measurements. When the chemical potentials of both reservoirs lie below the energy of the first subband of the QPC, as shown in panel a) of Fig. 2.4, conduction depends entirely on thermal broadening of the conductance plateau. At zero temperature

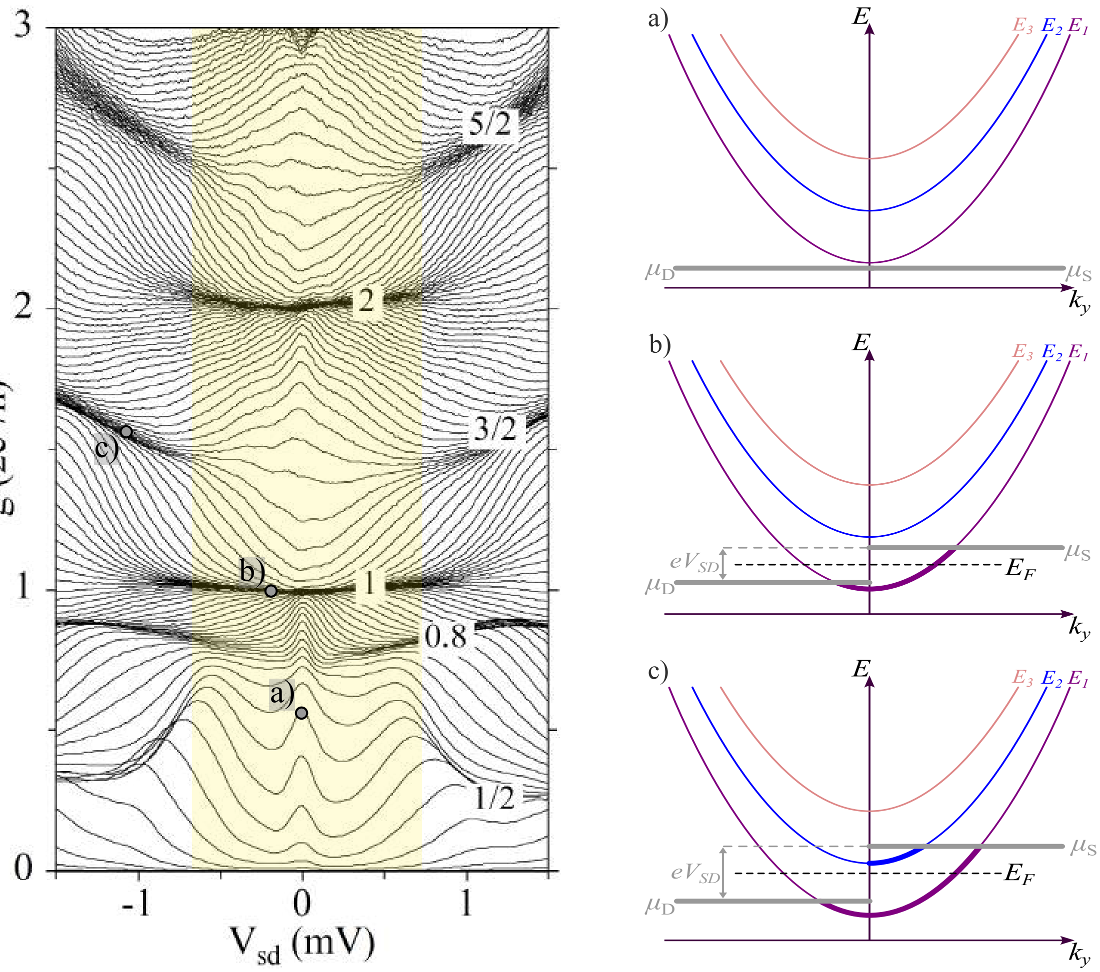

Figure 2.4: Bias spectroscopy measurement of a QPC at 80 mK and zero magnetic field, taken from Ref. [60]. The ZBA appears as a peak in all conductance traces below $g = 2e^2/h$ centered at $V_{SD} = 0$ mV. a) The chemical potentials of both reservoirs are lower than the energy of the first subband of the QPC. b) The chemical potentials of both reservoirs are situated between the first and second subbands. c) The chemical potential of the source lies between the first and second subbands, while that of the drain is between the second and third subbands.

and in a perfect ballistic QPC, no conduction would occur here. In panel b), the chemical potentials of both reservoirs are between the first and second subbands. Here, current flow results from the presence of uncompensated states within the bias window defined by $eV_{SD} = \mu_S - \mu_D$. Panel c) depicts the situation where the chemical potential of the source lies between the first and second subbands, while that of the drain lies between the second and third subbands. In this case, current also flows due to uncompensated states; however, the presence of a subband within the bias window introduces a half-plateau in the conductance, indicating a departure from the linear transport regime.

In this work, bias spectroscopy was used to validate the linear-response conductance measurements and to achieve a more complete characterization of our quasi-ballistic QWs. This will be discussed in detail in Sec. 5.4.2.

2.2.3 Luttinger Liquid

As of now, we have looked at 1D constriction in terms of Fermi liquid theory, which treats electron-electron interactions as small perturbations. In 1D systems, this could not be farther from the truth. In fact, the electrons in a 1D system are forced to interact with each other, and only collective excitations are permitted. Furthermore, there is no energy window for which the lifetime of the quasiparticle in the Fermi liquid picture diverges due to the importance of interaction in 1D [61]. To describe these systems, a powerful theoretical technique known as bosonization is employed, which reformulates the Hamiltonian in terms of bosonic operators. The resulting model is referred to as the Luttinger liquid, whose modern formulation emerged from the foundational work of Tomonaga, Luttinger, Mattis, and Lieb over a span of approximately 15 years. Haldane later unified and generalised these developments in 1981[21]. The remarkable feature of this model is that it describes a macroscopic number of particles interacting collectively according to an exactly solvable Hamiltonian with elementary excitations given by independent density waves of charge ρ and spin σ [22]. The Luttinger liquid Hamiltonian takes an elegant form: $H = H_\rho + H_\sigma$, with

$$H_{(i=\rho,\sigma)} = \frac{\hbar}{2\pi} \int \left[\frac{u_i K_i}{\hbar^2} (\pi \Pi_i(y))^2 + \frac{u_i}{K_i} (\nabla \phi_i(y))^2 \right] \mathrm{d}y, \tag{2.11}$$

---

[21] Tomonaga first introduced the model in 1950 [62]; Luttinger relaxed certain constraints in 1963 [63]; and Mattis and Lieb corrected Luttinger's formulation in 1965 [64]. Haldane subsequently demonstrated in 1981 that the model applies to any 1D system and that the resulting wavefunction corresponds to the first harmonic approximation of the general solution [65].

[22] A 2022 study reports the observation of separate spin and charge Fermi seas beyond the low-energy limit of the Tomonaga-Luttinger model, using arrays of QWs coupled to a 2DEG [66].

where $\phi_i(y)$ is a labeling bosonic field associated with displacement ($\nabla\phi_i(y)$ is related to density of charge $i = \rho$ and spin $i = \sigma$). Its canonically conjugate field, $\Pi_i(y)$, represents the phase of the bosonic excitations in the charge, $i = \rho$, or the spins, $i = \sigma$, sector [61]. The dimensionless Luttinger liquid parameters u_i and K_i denote the density wave velocity and the interaction strength[23], respectively. Some physical intuition can be gained by comparing the Luttinger liquid Hamiltonian to that of an elastic string,

$$H_{str} = \frac{1}{2}\int \left[v_{str}(\Pi_{str}(y))^2 + \frac{v_{str}}{K_{str}}(\phi_{str}(y))^2 \right] \mathrm{d}y. \tag{2.12}$$

Here, K_{str} and v_{str} represent the stiffness and the velocity of the different elements of the string, respectively [67].

Some properties of a Luttinger liquid are expressed similarly to those of a weakly interacting Fermi liquid, *e.g.*, the specific heat of a Luttinger liquid is equivalent to that of a Fermi liquid with a renormalizing factor for the interactions. However, other properties diverge drastically from their Fermi liquid counterparts. A particularly relevant example in the context of this work is the temperature dependence of Coulomb drag resistance between pairs of Luttinger liquids. In identical Fermi liquids, the Coulomb drag resistance is expected to decrease linearly with temperature. In contrast, for Luttinger liquids, it is predicted to increase exponentially as the temperature decreases[24]. Another example of this is the conductance of a QW in its first subband. The Hamiltonian of Eq. 2.11 implies the conductance for a Luttinger liquid is given by

$$G_{LL} = \frac{2e^2}{h}K_\rho, \tag{2.13}$$

which differs from the Landauer–Büttiker conductance for the first subband ($N = 1$ in Eq. 2.9), except for the non-interacting case ($K_\rho = 1$). At first glance, this discrepancy might appear to contradict the formation of a Luttinger liquid in long,

---

[23] For $0 < K_i < 1$, the interactions are repulsive; for $1 < K_i < \infty$, they are attractive. The non-interacting case corresponds to $K = 1$.

[24] Further discussion of this phenomenon is provided in Sec. 2.3.1.

single-mode QWs, since experimental observations consistently validate Eq. 2.9, even in QWs extending over a few microns [26, 68]. However, all experimental realizations of QWs involve contacts to Fermi liquid reservoirs at their extremities, which effectively mask the intrinsic Luttinger liquid behavior of the wire[25]. As a result, conventional conductance measurements alone are insufficient to reveal Luttinger liquid characteristics. To probe Luttinger liquid behavior directly, more sophisticated experimental techniques are required. One particularly suitable approach involves studying interactions between pairs of coupled QWs — commonly referred to as Coulomb drag experiments — which are well-suited for investigating the collective transport properties predicted by Luttinger liquid theory.

2.3 Coulomb Drag Between 1D Constrictions

Coulomb drag between QWs is illustrated in Fig. 2.5 in its simplest form. Electrons from the reservoirs attached to the drive QW of length L are driven through the wire (in the opposite direction from current flow) due to an applied voltage difference $V_{Drive} = R_{Drive} I_{Drive}$. If the distance d between the drag and drive QWs is sufficiently small, electrons in the drive wire can induce motion of the electrons in the drag wire via inter-wire Coulomb interactions. In a typical Coulomb drag experiment, the drag circuit is connected to a voltmeter to measure the accumulated voltage between the drag wire reservoirs. Due to the induced motion, electrons tend to accumulate in the left reservoir of the drag wire. When the voltage across the drag wire is measured with the same polarity as the drive wire, the resulting drag voltage is negative. To define a positive and experimentally meaningful quantity that captures the strength of this effect, the drag resistance is introduced as

$$R_D = -\frac{V_{Drag}}{I_{Drive}}. \tag{2.14}$$

---

[25] The underlying physics is more nuanced than this simplified explanation. For a more comprehensive discussion, see Refs. [69–71].

While extensive experimental work has been conducted on Coulomb drag between pairs of 2DEGs, significantly less attention has been given to QWs. This disparity can be attributed, in part, to the complexity of the device architectures required for such studies, as well as the fabrication challenges associated with producing long QWs, essential for investigating Coulomb drag in the Luttinger liquid regime. Among the few experimental groups that have explored Coulomb drag in QWs, two primary research motivations stand out: the search for evidence of Luttinger liquid behavior, and the investigation of Wigner crystal formation. A third avenue of research, known as the charge fluctuation model for drag, has received comparatively less experimental attention[26], yet it remains a particularly intriguing avenue for future research.

The very first Coulomb drag experiment on quasi-ballistic QWs was conducted in 2001 by Debray *et al.* [36]. This experiment used laterally coupled QWs defined by lithographically fabricated gates atop a 2DEG formed in a GaAs heterostructure. A key challenge with this approach is the difficulty in generating a sufficiently high potential barrier between the two QWs to suppress tunneling, without significantly increasing the barrier width d, because of lithography limitations and shadow effects. A large inter-wire separation d is problematic because the drag voltage is expected to decay exponentially with increasing d. More critically, phonon-mediated drag becomes the dominant mechanism above 100 mK when $k_F d \gtrsim 10$, and remains non-negligible for $k_F d \gtrsim 5$ [37]. Using the reported inter-wire distance $d \sim 0.2$ μm and estimating k_F from their carrier density yields $k_F d \sim 26$, well above the threshold where phonon drag is expected to dominate[27]. Despite these concerns, Luttinger liquid theory was used to interpret several aspects of their experimental results.

Shortly after the initial study by Debray *et al.*, a second group (Yamamoto *et al.*) undertook the challenging task of experimentally investigating Coulomb drag,

---

[26] To date, only the Gervais group and the Laroche group — formed by a former student of the Gervais group — have studied this regime experimentaly.

[27] Debray *et al.* experimentally estimated a much smaller value of k_F than typically observed in similar 2DEG systems. Based on their estimate — approximately six times smaller — they obtained $k_F d \sim 3$, placing their experiment in a regime where phonon drag could be neglected.

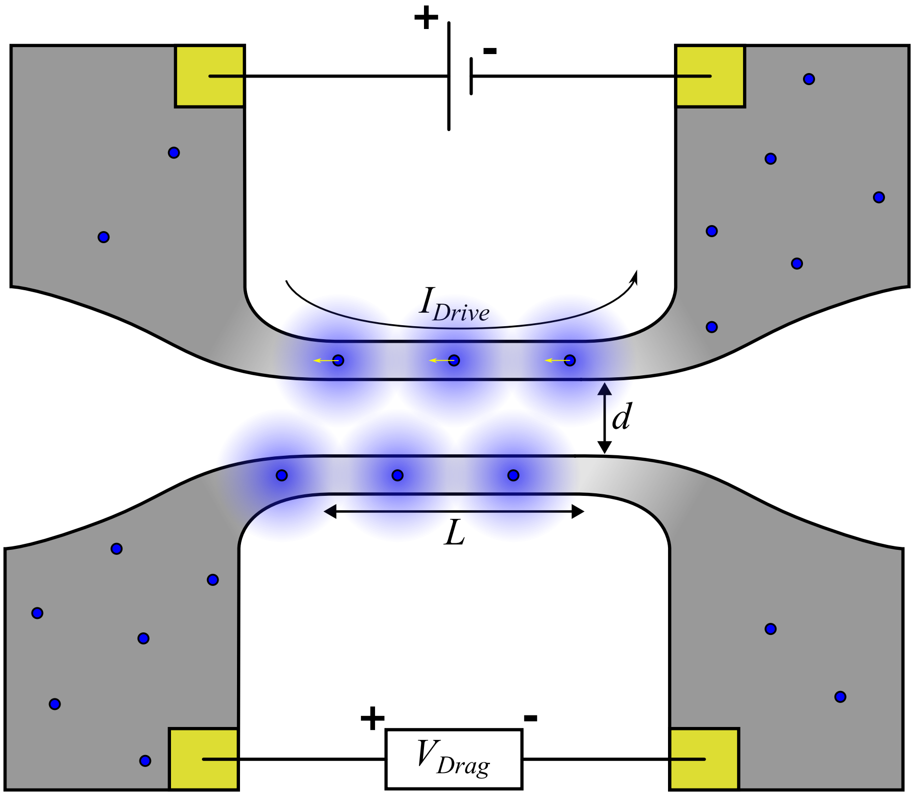

Figure 2.5: Schematic illustration of a Coulomb drag experiment between two QWs. A drive current flows from the left reservoir to the right reservoir of the drive QW (corresponding to electron motion from right to left). The drag voltage is measured across the drag QW with the same polarity as the drive wire. The inter-wire separation is denoted by d, and the length of the QWs is L.

again using laterally coupled QWs [38–40]. In their experiments, the observation of negative Coulomb drag resistance in the presence of a magnetic field was interpreted as evidence for Wigner crystal formation. However, as in the earlier study, their results may have been influenced by phonon-mediated drag. Based on their reported parameters, they have $3 < k_F d < 7$, placing their system in a regime where phonon drag is expected to be non-negligible.

In 2011, a new platform for studying Coulomb drag was introduced by Laroche *et al.* [42], which addressed the issue of phonon drag by vertically integrating QWs in two separate 2DEGs formed within a single GaAs/AlGaAs heterostructure. These layers were separated by an AlGaAs barrier, whose aluminum concentration could be tuned to control the tunneling resistance, *i.e.* the barrier height. Thanks to

MBE techniques, barrier layers as thin as 15 nm could be reliably fabricated, significantly reducing the inter-wire separation d [41]. This design eliminates phonon drag as a dominant mechanism, since for typical 2DEG parameters (see Table 2.1), the estimated value $k_F d \sim 1 < 5$ places the system well below the threshold where phonon drag becomes significant. Using this platform, Laroche *et al.* studied the dependence of the drag signal on subband occupancy, and both momentum transfer and charge fluctuation models could be applied to their observations, which included negative drag resistance [42]. Subsequent temperature-dependent measurements revealed the presence of a crossover temperature T^*, which was interpreted as a potential signature of Luttinger liquid behavior [42]. More recently, the same platform was employed to investigate nonreciprocal effects in quasi-1D wires, as predicted by charge fluctuation models [44]. At low temperatures, an increase in drag resistance with decreasing temperature was observed, despite strong evidence for charge fluctuation drag. Shortly thereafter, the ability to selectively tune between drag regimes — reciprocal and nonreciprocal — was demonstrated in this device architecture [45], enabling the study of nonlinear Coulomb drag between Luttinger liquids in the presence of disorder [46].

2.3.1 Fermi Liquid Formalism for Drag

The type of Coulomb drag illustrated in Fig. 2.5 is referred to as the momentum-transfer picture of Coulomb drag. Within this framework, two primary theoretical models coexist: the Fermi liquid model and the Luttinger liquid model. In both cases, Coulomb drag arises from momentum transfer between charge carriers in the drive wire — driven by a current I_{Drive} — and those in the drag wire, located at a separation d. This interaction results in a potential difference V_{Drag} across the drag wire, which is the measurable quantity of the drag effect.

As mentioned earlier, a 2DEG is well-described by a non-interacting Fermi gas. Fermi liquid theory models the elementary excitations of this system as quasiparticles just outside the Fermi surface and quasiholes just inside it. These quasiparticles are effectively dressed by interactions, allowing the system to behave as if it were non-interacting. Fermi liquid theory has been highly successful in describing Coulomb drag between pairs of 2DEGs. In one dimension, however, the situation is fundamentally different, and Luttinger liquid theory is in principle required to capture the strongly correlated nature of the system. Nevertheless, Fermi liquid theory can still be used to try to derive an expression for the drag resistance in 1D systems. For aligned subbands and small excitations ($eV/k_BT \ll 1$), the Fermi liquid model for identical wires yields a 1D drag resistance at a temperature T,

$$R_D^{(FL)} = \frac{Lk_BT|V(k_F)|^2}{2\hbar^2 e^2 v_F^3}, \tag{2.15}$$

where $V(k_f)$ characterizes the inter-wire Coulomb-assisted backscattering probability. The drag resistance in Fermi liquid theory is therefore expected to be directly proportional to temperature for identical QWs. For larger excitations, *i.e.* $1 \ll eV/k_BT$, the Coulomb drag resistance becomes proportional to $\cosh^{-4}(p^2/4m^*k_BT)$, where p is the momentum of the Fermi quasiparticles [72].

For QWs occupying the same subband but with differing Fermi wave vectors k_F and velocities v_F, the temperature dependence of the Coulomb drag resistance deviates from the linear behavior observed in identical wires. In this case, the drag resistance exhibits an exponential decay with temperature, governed by the mismatch in Fermi parameters between the wires[28].

2.3.2 Luttinger Liquid Formalism for Drag

Luttinger liquid theory predicts an exponential increase in drag resistance with decreasing temperature in the strong coupling limit, regardless of whether only backscattering or both forward and backward scattering processes are considered. Even in the spin-incoherent regime, *i.e.* when the spins are thermally disordered but the charges are still coherent, the temperature dependence remains exponential

---

[28] Drag resistance is also expected to decrease exponentially with the inter-wire separation.

under strong coupling conditions [73]. This behavior stands in stark contrast to the linear temperature dependence predicted by Fermi liquid theory. In fact, the Coulomb drag between strongly coupled infinitely long Luttinger liquids is expected to follow

$$R_D \sim e^{\frac{T^*}{T}}, \tag{2.16}$$

where T^* is the crossover temperature separating strong and weak coupling regimes [74]. This crossover temperature depends on the inter-wire separation d, the wire width W, the effective Bohr radius a_B^*, and the mean (intrawire) charge separation $r = \pi/k_F$. In general, T^* is a complicated function of these parameters, but in specific limiting cases, its dependence simplifies and reveals distinct scaling behavior (see section 2.3.2). Conceptually, below T^*, the charge density waves (CDW) in the drag and the drive wire are expected to be locked together as shown schematically in Fig. 2.5. Above this crossover, multiple drag regimes may emerge, depending on the relative ordering of key length scales: the Fermi wavelength, λ_F, the length of the wires, L, the thermal length[29], $L_T = \hbar v_F / K_\rho^- k_B T$, the soliton width[30], L_s, and the density of charges in the wires. A detailed discussion of these models can be found in Refs. [75, 76][31]. Here, only the main results of these models are presented.

Backscattering Model

For an identical pair of QWs, the main idea behind the theoretical treatment of Coulomb drag between Luttinger liquids introduced by Klesse *et al.* is to describe the excitations of the double QW systems using a pair of displacement fields $\phi_1(y)$ and $\phi_2(y)$ for wire 1 and wire 2, respectively. The eigenmodes of the system are

---

[29] Conceptually, when $L < L_T$, electrons injected from the 2DEG reservoir do not spend sufficient time within the QW to fully acclimate with the Luttinger liquid state. As a result, the system does not reach the idealized Luttinger liquid regime, and corrections to the expected drag signal may arise.

[30] The soliton width is the length scale at which the renormalization breaks down and a localized packet of spin or charge, *i.e.* a soliton, forms due to backscattering, umklapp processes, or coupling to a potential (in the sine-Gordon model).

[31] Additionally, a nonequilibrium many-body model of Coulomb drag developed by Guo and Zhou predicts a power-law dependence of the drag resistance on temperature [77]. Dimitriev *et al.* also developed a model of small-angle backscattering for Coulomb drag [78, 79].

then expressed as symmetric (in-phase, +) and antisymmetric (out-of-phase, −) combinations of these fields, representing collective density oscillations. The total Hamiltonian for Coulomb drag between Luttinger liquids is then $H_{LLD} = H^+ + H^- + H_b$, where $H^\pm$ are Luttinger liquid Hamiltonians of the form given in Eq. 2.11 with new interaction constants $u_i^\pm$, and $K_i^\pm$ that reflect the symmetric and antisymmetric modes of the spin and charge sectors. H_b represents the backscattering Hamiltonian, which accounts for inter-wire scattering processes and can be derived analytically.

In this formalism, the crossover temperature for a widely separated pair of QWs, $r \ll d$, is expected to decay exponentially with the inter-wire distance as

$$T^* \sim T_F e^{-\frac{k_F d}{1-K_\rho^-}}, \tag{2.17}$$

where K_ρ^- is the Luttinger liquid interaction parameter of the relative charge-density sector. In contrast, for closely spaced QWs, $d \ll r$, T^* is exponentially suppressed as

$$T^* \sim T_F e^{-\frac{\pi^3 c(k_F)}{r_s^{(1D)} k_F d}}, \tag{2.18}$$

with $c(k_F)$ being a logarithmic function of k_F, typically of order unity. As the temperature rises above T^*, thermal fluctuations begin to disrupt the locking of charge density waves between the wires. In this regime, perfect locking does not occur; instead, electrons in the drive wire experience backscattering due to the fluctuating potential generated by charge density variations in the drag wire. This backscattering mechanism results in momentum transfer between the QWs, giving rise to a measurable drag signal. Perturbative calculations by Klesse *et al.* have shown that, in this regime, the drag resistance scales with temperature as

$$R_D \sim \overline{\lambda}^2 \frac{hk_F}{e^2} \left(\frac{T}{E_F}\right)^{4K_\rho^- - 3}, \tag{2.19}$$

where $\overline{\lambda}$ is the interwire backscattering potential [74]. This result implies that for sufficiently strong repulsive interactions, the drag resistance increases as temperature decreases. In contrast, for weakly repulsive or attractive interactions ($K_\rho^- > 1$), the drag resistance decreases with decreasing temperature.

When the QWs are not matched, the temperature dependence of the drag resistance becomes highly sensitive to the specific drag regime. Considering only backscattering in the strong coupling limit with $T < T^*$,

$$R_D \sim \begin{cases} a(T)e^{\frac{(T^*-W)}{T}}, & \text{if } W < T^* \\ \frac{b(T)}{\sqrt{(W^2-(T^*)^2)}}, & \text{if } W > T^* \end{cases}, \tag{2.20}$$

where $W = |\mu_1 - \mu_2|/k_B$ is the chemical potential difference between the two wires, and the coefficients $a(T)$ and $b(T)$ are prefactors whose exact forms remain unknown and might be temperature-dependent [80]. For small mismatches in chemical potential ($W < T^*$), the temperature dependence of the drag resistance resembles that of the matched-wire case, though the exponential growth with decreasing temperature is slower. In the weak coupling regime ($T > T^*$), a density imbalance between the QWs leads to an exponential suppression of the drag resistance of Eq. 2.19.

Forward scattering Model

For an identical pair of QWs, the inclusion of forward scattering leads to three distinct regimes of temperature dependence for the drag resistance,

$$R_D \sim \begin{cases} \frac{1}{l_0}\left(\frac{T_0}{E_F}\right)^2\left(\frac{T}{E_F}\right)^{-3/2}, & \text{if } T_F = E_F/k_B < T \\ \frac{1}{l_0}\left(\frac{T_0}{E_F}\right)^2, & \text{if } T_0 \sim v_F/d < T < T_F \\ \frac{c_i}{l_0}\left(\frac{T}{E_F}\right)^2, & \text{if } T^* < T < T_0 < T_F \end{cases}, \tag{2.21}$$

where l_0 is the forward scattering length. The transitions between regimes occur at T_0 and T_F [81]. For temperatures below T^*, charge density wave locking is still expected to dominate, leading to an exponential increase in drag resistance as temperature decreases, as in Eq. 2.16.

When the QWs are not matched, the temperature dependence of the drag resistance deviates substantially from the exponential behavior observed in the backscattering-only scenario. In the presence of a large density imbalance, the exponential growth of R_D with decreasing temperature is suppressed, and a power-law dependence emerges instead [82]. The drag resistance in this regime is given by

$$R_D \sim \begin{cases} \left(\frac{T_1}{E_F}\right)^4 \left(\frac{T}{T_1}\right)^5, & \text{if } T < T_1 = \hbar k_F (v_{F1} - v_{F2})/k_B \\ \left(\frac{T_1}{E_F}\right) \frac{T}{T_1} e^{-\frac{T_1}{T}}, & \text{if } T > T_1 \end{cases}, \tag{2.22}$$

where v_{F1} and v_{F2} are the Fermi velocities of the drive and drag wires, respectively, and T_1 characterizes the energy scale associated with the velocity mismatch.

Spin-incoherent regime

In QWs with sufficiently low electron density, where the dimensionless parameter $n_e^{(1D)} a^*_{Bohr} \ll 1$, the system can enter the spin-incoherent regime. In this regime, spin-density waves become thermally disordered, while charge-density waves remain coherent, and the spin exchange energy between neighboring electrons J becomes suppressed such that $J \ll k_B T \ll E_F$.

When the density of the QWs are matched, and the temperature satisfies $T < T^*$, an exponential dependence on temperature, as described by Eq. 2.16, is still expected. However, for higher temperatures, two distinct regimes emerge,

$$R_D \sim \begin{cases} T^{\alpha_{2k_F}} e^{-\frac{\bar{c}T}{J}}, & \text{if } T^* < T < J/k_B \\ T^{\alpha_{4k_F}}, & \text{if } T > J/k_B \end{cases}, \tag{2.23}$$

where $\bar{c}$ is a constant of order one. The exponents depend on the cleanliness of the wires: for clean QWs, $\alpha_{2k_F} = 2K_\rho^- - 1$ and $\alpha_{4k_F} = 8K_\rho^- - 3$; for disordered QWs, $\alpha_{2k_F} = 2K_\rho^-$ and $\alpha_{4k_F} = 8K_\rho^- - 2$ [73].

When the densities of the QWs are not matched, the behavior of the drag resistance is qualitatively similar to that of the identical wire case. However, the drag resistance is expected to drop sharply as the density mismatch increases. Numerical results presented in Ref. [73] show that, at low temperatures, the drag resistance decreases approximately exponentially with increasing density mismatch. The effect of disorder in the spin-incoherent regime was also theoretically investigated by Fiete *et al.* [73]. It was found that disorder can enhance the robustness of the drag signal against density mismatches, effectively mitigating the suppression of drag resistance that would otherwise occur in a clean system.

It is worth noting that for a QW formed in a 2DEG with parameters listed in Table 2.1, we have $n_e^{(1D)} a_{Bohr}^* \approx 0.43 < 1$, suggesting that the system may lie near the spin-incoherent regime in the weakly interacting limit (for $T > T^*$). However, since $n_e^{(1D)} a_{Bohr} \approx 1$ and not $n_e^{(1D)} a_{Bohr} \ll 1$ a fully spin-incoherent state is not expected. Either way, this should not change the strong coupling behavior of the drag when $T < T^*$.

Finite length effects

Finite length effects of the QWs on the drive current and temperature dependence of the Coulomb drag resistance were theoretically studied in Ref. [84]. One of the key finite-size effects is the suppression of charge density wave (CDW) locking below the crossover temperature T^* when the wire length L is smaller than $\hbar v_F / k_B T^*$. For QWs formed in a 2DEG with parameters listed in Table 2.1 and a length of 5 μm, as in this work, finite-size effects are expected to suppress the charge density wave locking for T^* values below $T^* = 0.27$ K. Finite-size effects are also expected to cause a non-monotonic drive current and temperature dependence of the drag voltage. This becomes particularly relevant when $u/\theta \gg 1$, where $u = eV_{drive}/\hbar\omega_L$, and $\theta = k_B T/\hbar\omega_L$, with $\omega_L = v_F / K_\rho^- L$ being the collective plasmonic excitation frequency of the wires. An experimental method to assess the importance of finite-length effects is to examine the linearity of the drag voltage versus the drive current. Any observed non-monotonicity may indicate that the drive voltage (drive current) is sufficiently large for finite-size effects to become non-negligible at a given temperature[32].

2.3.3 Charge Fluctuation Model

The charge fluctuation model, introduced in 2008 by Alex Levchenko and Alex Kamenev [85], describes Coulomb drag by emphasizing the role of charge and energy fluctuations and their rectification by the drag wire. In this model, the thermal charge fluctuations in one wire can induce a DC voltage in the adjacent wire via a rectification mechanism, even in the absence of significant momentum transfer from a drive current. These fluctuations become particularly relevant when the system length L is comparable to or smaller than both the voltage length $L_v = \hbar v_F / eV_{drive}$, and the thermal length $L_T = \hbar v_F / K_\rho^- k_B T$. Under such conditions, the drag signal may be dominated by fluctuation-induced effects rather than conventional momentum-transfer mechanisms.

When a fluctuation induces a local charge accumulation in one wire, the adjacent wire experiences a corresponding localized reduction in charge density. The lower density of charge is then rectified, and the strength and direction of this rectification depends on the potential landscape of the wire[33]. In particular, asymmetries in electron-hole transmission probabilities or in the measurement circuitry are predicted to strongly influence the observed Coulomb drag resistance resulting from the rectification of these fluctuations. These asymmetries can even lead to a drag voltage that is independent of the direction of the drive current, thereby violating the reciprocity relations typically expected in linear response theories such as the momentum-transfer models discussed above. To date, only the charge fluctuation model can account for violations of reciprocity relations in Coulomb drag.

---

[32] Linearity of the Coulomb drag signal also serves as a diagnostic for self-heating in the drive wire. Since drag resistance is highly temperature-dependent, any temperature variation due to Joule heating would manifest as a non-monotonic drag voltage response to increasing drive current.

[33] The potential landscape is shaped by the heterostructure design, the dopant, the impurities and the geometry of the depletion gates. Irregularities in the depletion gate inevitably translate to irregularities in the confining potential.

Charge fluctuation equations for the Coulomb drag resistance have been derived in the context of intrinsic coupling between quantum dots [86], intrinsic coupling between non-ballistic QWs (diffusive regime) [44], and for QPCs [85]. In coupled QPCs and non-ballistic QW, the Coulomb drag arising from charge fluctuations can be decomposed into two principal contributions. The first is a linear component originating from the rectification of near-equilibrium thermal noise. The second, more prominent at high drive currents, is a nonlinear contribution resulting from the rectification of quantum shot noise[34]. For QPCs in the ballistic transport regime with no interaction, the temperature dependence of the charge fluctuation-induced Coulomb drag — considering both the reciprocal and nonreciprocal drag — follows a quadratic scaling, $R_D \sim T^2$ [85]. In diffusive QWs with short-ranged electron-electron interaction, an inverse temperature dependence of the drag resistance is expected, $R_D \sim T^{-1}$ [44].

---

[34] Higher-order nonlinear terms may also contribute to the drag signal, particularly under strong driving conditions.

2.4 Summary and Conclusion

In this chapter, we introduced the key concepts of low-dimensional experimental quantum physics necessary to fully grasp the main results of this thesis. The primary theoretical framework for one-dimensional transport — the Luttinger liquid model — was presented. Unlike conventional Fermi liquids, Luttinger liquids exhibit strong electron-electron interactions due to the spatial confinement that prevents particles from passing each other. As a result, excitations in these systems propagate as collective spin and charge waves, a phenomenon known as spin-charge separation. The relevant length scales for the formation of a Luttinger liquid were discussed and are summarized in Table 2.2.

Length Scales	**Values and estimates**	**Thresholds**
1D gas parameter	$r_s^{1D} = \frac{1}{2n_e^{(1D)}a^*_{Bohr}} \approx 0.92$	Wigner crystal effect on drag for: $r_s^{(1D)} \geq 4$
Phonon drag	$k_F d \sim 1$	Phonon drag is significant for : $k_F d \geq 5$
Crossover temperature	$T^* = T_F e^{-\frac{k_F d}{1-K_\rho^-}}$ For $K_\rho^- = 0.65$, $T^* = 0.831$ K	For $r \ll d$
Spin incoherence	$n_e^{(1D)}a^*_{Bohr} \approx 0.43$	Spin incoherent regime: $n_e^{(1D)}a^*_{Bohr} \ll 1$
Thermal length	$L_T = \hbar v_F / K_\rho^- k_B T$ For $K_\rho^- = 0.65$ and at 300 mK, $L_T = 7.05\ \mu$m	For Luttinger liquid behavior $L_T \lesssim L$
Voltage length	$L_v = \hbar v_F / eV_{drive}$ For $V_{drive} = 50\mu$V, $L_v = 2.4\mu$m	Mesoscopic effects are important for $L \lesssim L_v$
Finite size effects	$T^* < \frac{\hbar v_F}{k_B L}$	CDW locking suppressed for $T^* < 0.27$ K

Table 2.2: Important length scales with estimates and thresholds for device parameters in Table 2.1.

The temperature dependence predicted by different theoretical models of Coulomb drag in 1D QWs was also introduced. Two main scenarios were considered: drag between identical QWs and drag between non-identical ones. In the case of identical wires, strong coupling leads to an exponential temperature dependence of the drag resistance, $R_D \sim e^{T^*/T}$. For weaker coupling, several theoretical models have been proposed, and their predictions are summarized in Fig. 2.6.

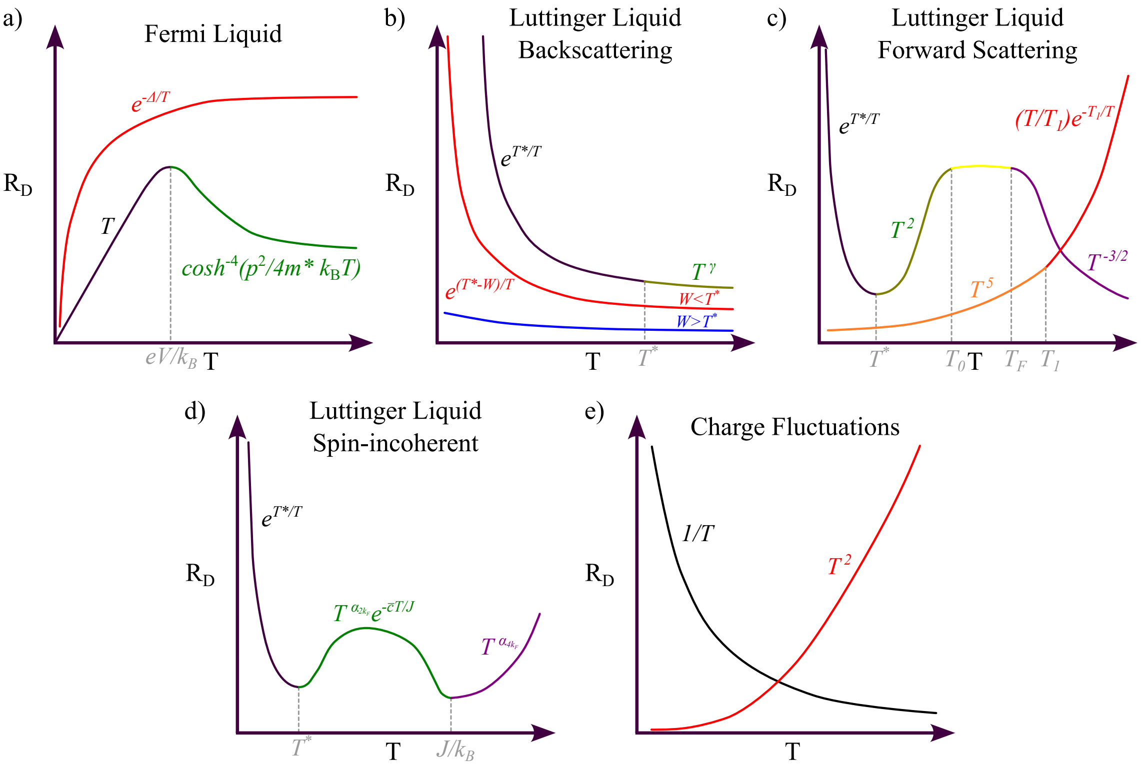

Figure 2.6: Summary of the temperature dependence predicted by various Coulomb drag models in 1D QWs. a) Fermi liquid: black and green lines represent identical QWs; the red line corresponds to mismatched QWs, with Δ denoting the difference in Fermi parameters between the QWs. b) Backscattering model: black and green lines represent identical QWs with γ denoting the power law exponent of Eq. 2.19; red and blue lines correspond to mismatched QWs. c) Forward scattering model: black, green, yellow, and purple lines represent identical wires; red and orange lines correspond to mismatched wires. d) Spin-incoherent model. e) Charge fluctuation models: the black line corresponds to diffusive QWs; the red line corresponds to ballistic QPCs.

For non-identical QWs, the temperature dependence becomes more complex and highly sensitive to the specific drag regime. Factors such as subband mismatch and density imbalance can significantly alter the drag response. These various temperature dependencies are also summarized in Fig. 2.6.

3

Design and Commissioning of a Cryostat Optimized for Quantum Devices

One could argue that the field of cryogenics originated with Michael Faraday's work on liquefying gases in the mid-1800s [87]. However, his achievements were made possible by earlier advancements in vacuum technology. In 1643, Evangelistae Torricellii invented the mercury barometer [88], and seven years later, Otto von Guericke developed the first vacuum pump [89] — both foundational contributions to the creation and control of low-pressure environments. Today, cryogenics plays a vital role in both industry and research, while vacuum technologies, once revolutionary, are now so widely used that they are often taken for granted in everyday applications.

This chapter provides a brief introduction to the dry dilution refrigerator. It then highlights specific aspects of commissioning a commercially available cryostat that are either unique to the Triton system manufactured by Oxford instruments or uncommon among dry dilution refrigerators typically employed in quantum measurement experiments. Finally, the design and development of the low-temperature tail is described in detail.

3.1 Dry Dilution Refrigerator

To provide a relevant introduction to the dry dilution refrigerator, this section outlines the procedure required to bring the cryostat to its base temperature — that is, the lowest achievable operational temperature. Achieving base temperature in a Cryofree® cryostat involves three critical processes: precooling to 4 K, condensing the helium mixture, and the dilution process. For the Triton system, the cooldown time to base temperature typically requires four days.

3.1.1 Reaching 4 K

Dry cryostats utilize a device known as a pulse tube to achieve temperatures near 4 K. Pulse tube coolers operate by generating pressure oscillations in helium gas, enabling cooling in a region devoid of moving parts. This design significantly reduces mechanical vibrations in the cold section of the system. Vibrations can adversely affect the cooling process. A detailed explanation of pulse tube operation can be found in Ref. [90].

As illustrated in Fig. 3.1, the Triton cryostat has six horizontal plates. The only plate maintained at room temperature is the top plate, located at the uppermost part of the cryostat. All of the other plates are under vacuum and thermally isolated from each other. The first stage heat exchanger of the pulse tube is thermally anchored to the pulse tube plate 1 (PT1), while the second-stage heat exchanger is connected to the PT2 plate.

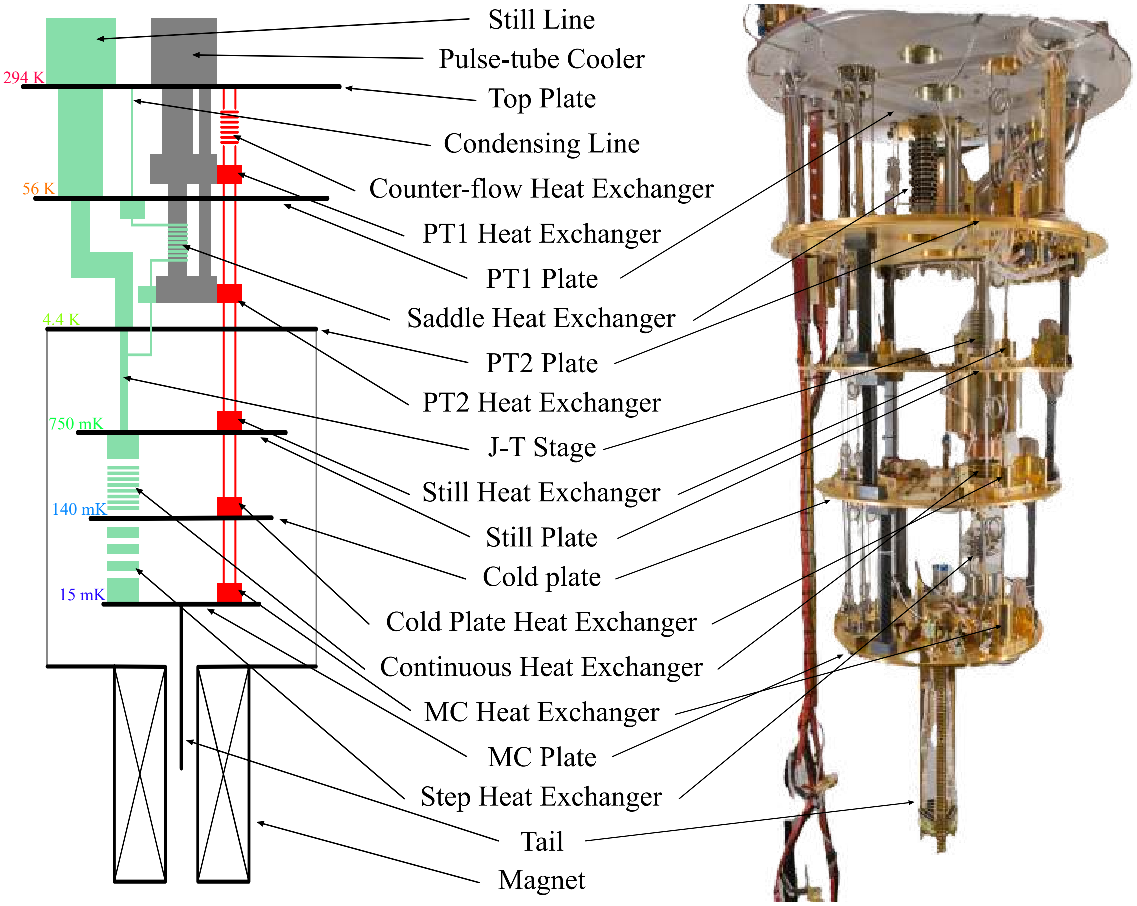

Figure 3.1: The Triton cryostat. On the left, a schematic highlighting the internal components, with the dilution unit shown in green and the pre-cool loop in red. Adapted with permission from Ref. [91]. On the right, a photograph of the Triton cryostat.

Since the remaining plates are thermally decoupled from the pulse tube's heat exchangers, the Triton employs a system known as the precool loop (depicted in red in Fig. 3.1) to bring the still plate, cold plate, and mixing chamber (MC) plate in thermal contact with the PT2 plate, thereby cooling them to approximately 10 K[1]. In this loop, a high-pressure[2] exchange gas[3] is circulated to establish thermal contact between the plates. This gas can then be evacuated from the preecool loop to re-establish thermal isolation. In the Triton system, the precool process is stopped

---

[1] A default value of 10 K is configured; this parameter can be modified via the system registry settings.

[2] The pressure in the precool loop is 1.5 bar at room temperature and is 0.2 bar at 5 K. The pressure is lowered as the temperature drops to balance thermal conductivity and minimize heat transfer from room temperature.

[3] The exchange gas is the same ^{3}He/^{4}He mixture used in the dilution unit.

once the MC plate reaches 10 K. At the end of this process, only the PT2 plate and the magnet are effectively at 4 K.

3.1.2 Condensing

Once all cryostat plates have reached their target temperatures and the exchange gas in the precool loop has been fully evacuated, condensation of the ^{3}He/^{4}He mixture can begin[4]. To do so, the mixture is pressurized to a few bars (typically 1-3 bar) and passed through the saddle heat exchanger, where it thermalizes to approximately 4 K. It is then further cooled *via* isenthalpic expansion through a Joule-Thomson (JT) cooler. This expansion sufficiently cools the mixture so that it condenses at the pressure present in the MC. Once the ^{3}He/^{4}He mixture has fully liquified, the dilution process can begin.

3.1.3 Dilution Process

The liquid–vapor boundary is located at the still plate, such that the majority of the dilution unit downstream of the Joule–Thomson stage is filled with liquid mixture (grey-blue in Fig. 3.2). When pumping begins, ^{3}He mainly evaporates due to its significantly higher vapor pressure compared to ^{4}He. Below approximately 0.87 K, the ^{3}He/^{4}He mixture undergoes a phase separation, which, when combined with the preferential evaporation of ^{3}He, results in the creation of a dilute and concentrated phase of ^{3}He.

The cooling effect arises from the enthalpy difference between the concentrated and diluted phases of the ^{3}He/^{4}He mixture. For efficient operation, the boundary between these two phases must reside within the MC. Its position is determined by the initial ^{3}He concentration in the gas mixture and the volume of the MC. The osmotic pressure difference between the higher-temperature mixture near the still plate and the lower-temperature mixture in the MC drives a continuous flow of ^{3}He

---

[4] Condensation occurs in the green region shown in Fig. 3.1.

isotope from the MC to the still.

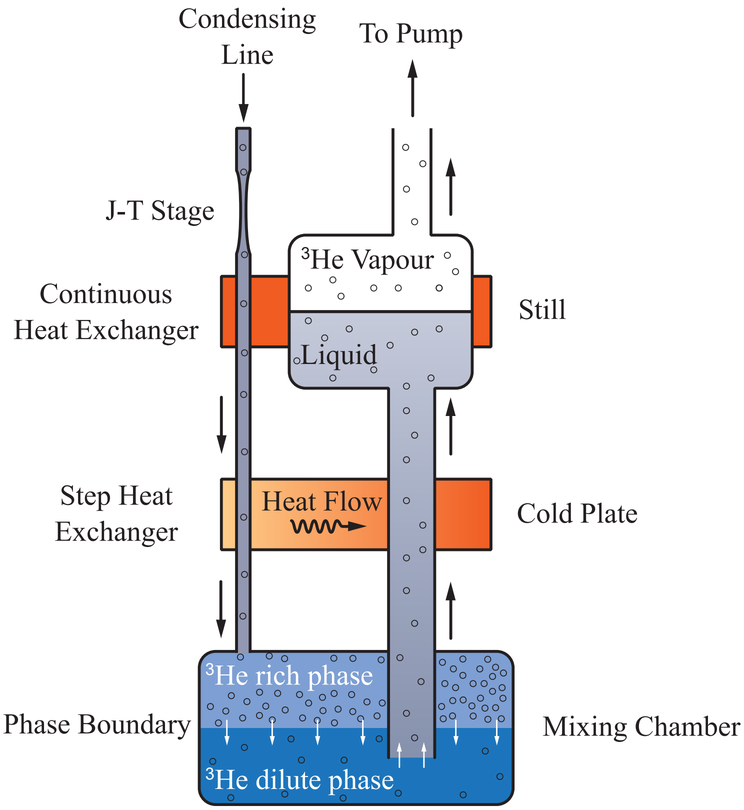

Figure 3.2: Schematic of a dilution unit. Modified with permission from Ref. [92].

The evaporated ^{3}He gas is then returned to the condensation line, passing sequentially through the saddle heat exchanger, the Joule-Thomson stage, and — most critically — the continuous heat exchanger and step heat exchangers, before re-entering the concentrated phase in the MC and sustaining the dilution process.

3.2 Triton Infrastructure

Several quantum devices typically operate at cryogenic temperatures on the order of a few millikelvin, where phonons are very weakly coupled to charge carriers. Achieving and maintaining such low temperatures requires the careful consideration of numerous components within the cryostat, many of which can be easily overlooked. The mechanical frame supporting the cryostat, as well as the connected piping, must be designed to minimize the transmission of external vibrations from the surrounding environment. Additionally, the pulse tube cooler must be sufficiently powerful to compensate for all heat loads, including those originating from magnet leads, internal structural supports, and wiring.

3.2.1 Frame

Experiments conducted at cryogenic temperatures, particularly in the millikelvin regime, are highly sensitive to mechanical vibrations. These vibrations can significantly impact measurement precision and device stability. Consequently, the design of a cryostat must carefully address all potential sources of vibration transmission from the surrounding environment to the structure of the dilution refrigerator. The primary means of mitigating such disturbances is the mechanical frame that supports the cryostat.

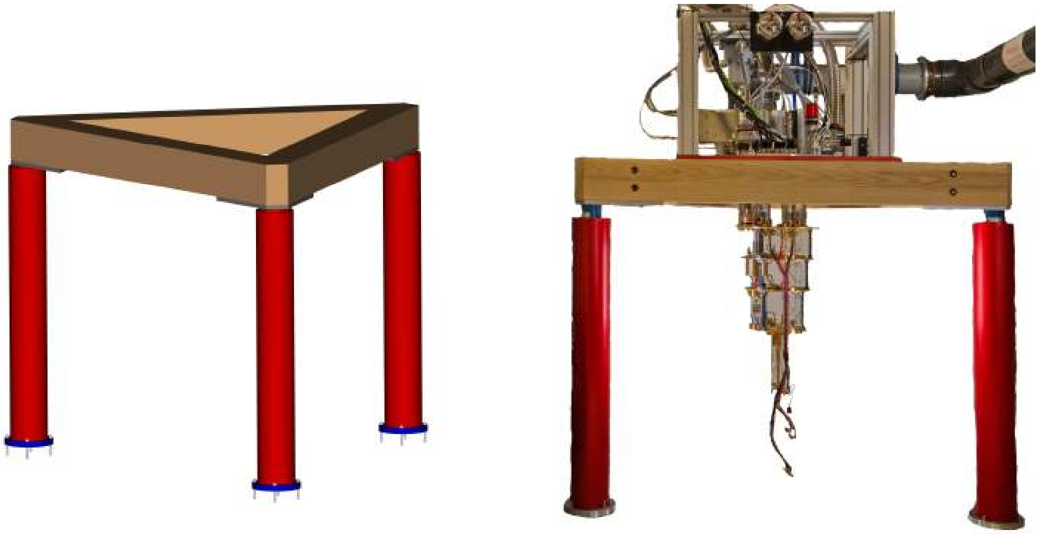

Figure 3.3: The Triton frame consists of an ash wood triangle supported by three aluminum cylinders, anodized red and filled with sand (left). Photograph of the complete cryostat assembly (right).

The ability of a material to dampen mechanical vibrations is commonly characterized by its loss factor, denoted as η, or equivalently by its quality factor, $Q = 1/\eta$. The loss factor is defined in terms of the vibrational energy E stored in the sys-

Material	**Loss Factor η**
Aluminum	0.000002 - 0.002
Steel	0.002 - 0.01
Concrete	0.02 - 0.06
Wood	0.005 - 0.01
Rubber	0.1 - 1
Lead	0.1 - 0.2
PVC	0.05 - 0.1

Table 3.1: Approximate vibrational loss factor values for common materials [95,96].

tem [94], and the amount of that energy lost every cycle of vibration ΔE as

$$\eta = \frac{\Delta E}{2\pi E}.$$

Materials with higher loss factors exhibit superior vibration damping capabilities[5]. Representative values for common materials are provided in Table 3.1.

The Triton top plate is a white-painted aluminum disk that sits on a larger red-anodized aluminum square plate. Electrical isolation between the two plates is achieved using a G-10 insulating ring inserted between them. The red-anodized plate is supported by a solid ash wood triangle[6]. This 300 pounds wood triangle rests on three vertical aluminum cylinders filled with sand, further enhancing the vibration damping performance of the frame (see Fig. 3.3). These cylinders are anchored to a concrete slab, which is itself mechanically isolated from the building structure via a rubber gasket[7]. The total mass of the assembled frame is close to 700 pounds.

---

[5] The effective loss factor of a mechanical system also depends on the geometric configuration and material distribution. A complete analytical or numerical treatment of the frame's vibrational response is beyond the scope of this thesis.

[6] Wood is selected for its substantial mass, mechanical strength, vibration damping properties, and ease of modification.

[7] Polymer rebars are used in the concrete slab to eliminate stray magnetic fields that would otherwise be introduced by steel reinforcement.

3.2.2 Pumps and Piping

Mechanical pumps are a significant source of vibration, which can be transmitted to the cryostat both through the floor — particularly if the pumps are located nearby — and *via* the connected piping. To mitigate floor-transmitted vibrations, all pumps on the Triton system are installed in a separate room, physically isolated from the cryostat. This configuration requires the use of extended piping, which, if not properly designed, can degrade the system's base temperature performance. Consequently, the two primary challenges in designing the Triton's piping infrastructure were minimizing vibration transmission through the pipes, and maintaining or improving the conductance of the longer piping relative to the original specifications provided by Oxford Instruments.

Piping Conductance

The cooling power of a dilution refrigerator is fundamentally determined by its ability to extract ^{3}He from the dilute phase. This extraction is achieved by pumping on the still using a turbomolecular pump backed by a multi-stage roots pump. In the original design by Oxford Instruments, the turbopump is connected to the refrigerator *via* a 5 m long bellow with an inner diameter of 100 mm. Under typical operating conditions — when the system is at base temperature — the pressure in the still line is on the order of 10^{-2} mbar, placing the ^{3}He flow within the molecular flow regime. In this regime, the conductance of the pipe is given by $C = 3.81D^3 s/l$ where D and l are the diameter and length of the pipe, respectively, and s is a constant that depends on the temperature and composition of the gas [93]. To achieve comparable or improved conductance with our extended polyvinyl chloride (PVC) line, we selected pipes with a diameter of 200 mm. Despite its greater length — approximately 11 m — this configuration yields a conductance that is 3.63 times higher than that of the original still line.

Pumps Vibrations

The use of extended piping is already an effective strategy for attenuating vibrations transmitted from the pumps to the cryostat. To further enhance vibration isolation, PVC was selected for the longest piping segments. PVC offers several advantages over stainless steel: it is significantly less expensive, easier to cut and assemble, and possesses a vibration loss factor approximately an order of magnitude greater than that of steel (see Table 3.1). Additionally, a large, heavy section of lead pipe is installed immediately before the cryostat to act as a vibration reflector. Due to its substantially higher vibrational impedance compared to PVC, this lead segment reflects a majority of the incoming vibrational energy, thereby preventing its transmission to the cryostat. Lead is also an excellent damping material, with a loss factor η in the range of 0.1 to 0.2.

3.2.3 Pulse Tube Cooler

The Triton's pulse tube cooler must provide greater cooling power than standard cryostat configurations, primarily to compensate for the additional heat load introduced by the three pairs of leads connected to the tri-axis vector magnet. For reference, the Bluefors PT410-RM pulse tube cooler delivers a cooling power of 0.9 W at 4.2 K, whereas the Triton is equipped with a PT415-RM model, which offers an enhanced cooling capacity of 1.35 W at 4.2 K.

An additional distinguishing feature of the Triton's pulse tube system is its use of a linear power supply. Unlike conventional square-wave drives, this power supply excites the pulse tube motor with a sinusoidal waveform, significantly reducing radio-frequency (RF) noise generated by the motor, which is an important consideration in sensitive quantum measurements.

3.2.4 Tri-Axis Vector Magnet

Many experiments involving quantum devices require the application of strong magnetic fields and, in some cases, the ability to precisely control the orientation of the field relative to the device. To enable such experiments, high-performance superconducting magnets are essential. The Triton system is equipped with a tri-axis superconducting vector magnet that provides full directional control of the magnetic field.

In earlier setups within the Gervais Lab, field orientation was adjusted using a mechanical sample rotator actuated by a pull string, which allowed rotation only within a single plane [97]. In contrast, the tri-axis vector magnet integrated into the Triton system enables magnetic field alignment in any spatial direction. The magnet assembly consists of five superconducting coils: one coil aligned along the z-axis, capable of generating magnetic fields up to 5.9 T, and two pairs of split coils aligned along the x- and y-axes, each capable of producing fields up to 1 T. A detailed map of the magnetic field distribution is provided in Appendix A.

3.2.5 Thermometry

All thermometry in the Triton cryostat was installed at the factory by Oxford Instruments. In cryogenic systems, thermometry serves critical roles in diagnostics, control, and measurement. Each thermometer must be carefully selected based on its intended function and the temperature range it monitors. As is standard in most cryogenic systems, the temperature measurements in the Triton are performed using a commercially available resistance bridge from LakeShore Cryotronics (Model 372). This instrument reads the resistance of various resistive temperature detectors (RTDs) and converts these readings into temperature values using factory-provided calibrations. Three types of thermometers are used in the Triton system: platinum, Cernox®, and ruthenium oxide (RuOx). A complete list of thermometers and their respective locations within the Triton cryostat is provided in Table 3.2.

Location	**Type**	**Model**	**Range**
High Power Heaters	Platinum	PT103	480 - 14 K
PT1 Head	Platinum	PT100	480 - 14 K
PT1 Plate	Platinum	PT100	480 - 14 K
PT2 Head	Cernox	CX-1050-CU-HT-1.4L	325 - 1.4 K
PT2 Plate	Cernox	CX-1050-CU-HT-1.4L	325 - 1.4 K
Magnet	Cernox	CX-1050-AA-1.4L	325 - 1.4 K
Still Plate	RuOx	RX-202A	40 K - 10 mK
Cold Plate	RuOx	RX-202A	40 K - 10 mK
Mixing Chamber	Cernox	CX-1050-CU-HT-1.4L	325 - 1.4 K
Mixing Chamber	RuOx	RX-202A	40 K - 10 mK

Table 3.2: Triton main thermometry.

Platinum thermometers operate over a wide temperature range (14 K to 873 K) and exhibit a negative temperature coefficient, with resistance decreasing as temperature increases. Their consistency can be optimized (±5 mK at 77 K) by controlling the purity of the platinum. These sensors are interchangeable and follow a standardized calibration curve, making them cost-effective and easy to implement.

Cernox® thermometers are made from a zirconium oxynitride thin film deposited on a sapphire substrate. They are excellent for use in magnetic fields and can be used at temperatures as low as 100 mK and as high as 420 K. Constructed from thin resistive films, they offer fast thermal response times and are easily thermally anchored to flat surfaces due to their compact form factor. While commonly used for diagnostics, they can also serve as measurement-grade sensors when their sensitivity is sufficient.

Ruthenium oxide (RuOx) thermometers are negative temperature coefficient RTDs designed for low-temperature applications, typically from 5 mK to 40 K. Their resistance and sensitivity increase as temperature decreases, making them particularly effective at ultra-low temperatures, up to the point where self-heating becomes significant. The Triton is equipped with three interchangeable Rox™ thermometers from Lake Shore (Model RX-202A), calibrated by Oxford Instruments for use across the 5 mK to 300 K range.

3.2.6 High-Power Heaters

The Triton cryostat is equipped with four high-power heater blocks, each rated at 80 W. These heaters are mounted on the PT1, PT2, still, and MC plates, enabling rapid thermal cycling and efficient warm-up of the system. However, caution must be exercised when using these heaters, particularly during warm-up procedures. Certain experimental devices — such as the Coulomb drag devices studied in this work — are fabricated from thin layers of materials with significantly different thermal expansion coefficients[8]. Rapid temperature changes can induce large thermal gradients, which in turn generate mechanical stress at material interfaces. This stress may lead to delamination or other mechanical failures of the devices.

Each high-power heater is paired with a platinum resistance thermometer for accurate temperature monitoring. The heaters are controlled *via* a Mercury iTC temperature controller, which supports proportional–integral–derivative (PID) regulation. The controller is pre-configured with optimized PID coefficients, allowing for stable and precise temperature control.

3.2.7 Wiring

Wiring within a cryostat can be broadly categorized into two types: instrumental wiring and experimental wiring. Instrumental wiring encompasses all connections essential for the operation of the cryostat, including thermometer wiring, heater wiring, and magnet leads. This type of wiring is typically installed by the cryostat manufacturer.

The experimental wiring from room temperature to the MC plate was installed by Oxford Instruments but designed in conjunction with Gervais Lab. It consists of eight looms, each containing 24 twisted-pair DC wires. Between the PT2 plate and the MC, all wires are made of superconducting material to minimize thermal

---

[8] For example, gallium arsenide (GaAs) and epoxy used in the EBASE process.

load and electrical resistance. Between the top plate and the PT2 plate, two of the looms are made of low-resistance copper wires, while the remaining six are made of constantan, chosen for its low thermal conductivity. The low-resistance copper wires are specifically used for measuring high-conductivity devices, where minimal series resistance is essential. However, this comes at the cost of increased thermal leakage due to copper's inherently high thermal conductivity.

In addition to DC wiring, high-frequency coaxial lines are also installed. CuNi coaxial cables are used from the top plate to the PT2 plate, and NbTi coaxial cables are employed from the PT2 plate to the MC.

3.3 Low Temperature Tail Design for Quantum Measurements

Although commercially available dilution cryostats have been on the market for some time, they have traditionally been sold without integrated sample holders[9]. As a result, it has become standard practice for low-temperature physics laboratories to design and fabricate their own sample holders in-house to meet the highly specific requirements of their experiments.

In the case of the Triton cryostat, two custom sample holders — commonly referred to as “tails" in the low-temperature physics community — were developed: one for DC measurements and another for high-frequency measurements in the microwave regime. This section focuses on the DC measurement tail, as it is the configuration used for the experiments presented in this thesis.

---

[9] Recently, several manufacturers have begun offering sample holders tailored for specific, frequently repeated measurements. Some also provide custom sample holder design services.

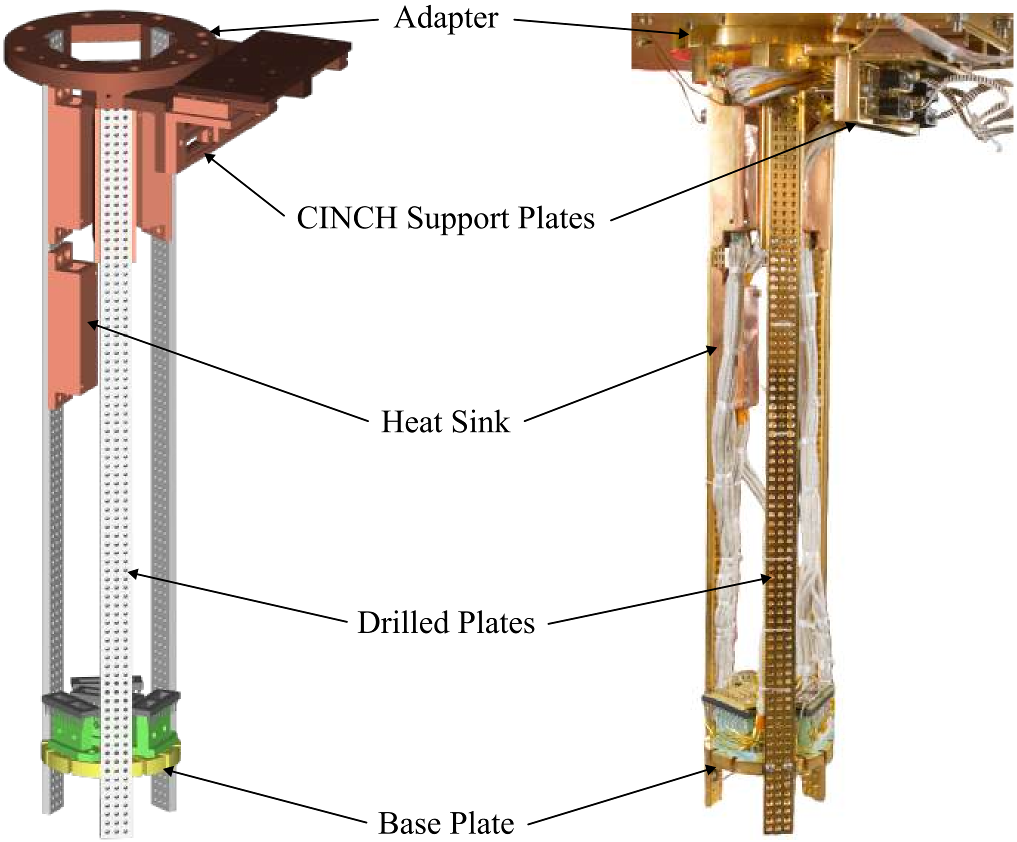

Figure 3.4: Design of the Triton sample holder. On the left, a schematic representation of the tail assembly. Components shown in orange are fabricated from OFHC copper, those in gray from coin silver, and those in yellow from high-purity silver. Sample headers are depicted in green and black. On the right, a photograph of the fully assembled tail mounted on the Triton cryostat. All metallic components are electroplated with gold to a thickness of approximately 470 nm. Multiple samples are visible, mounted on each of the headers.

3.3.1 Requirements

The design of the tail must satisfy a range of highly specific requirements, which can be categorized into three domains: electrical and magnetic, structural, and thermal. These requirements are inherently interdependent, as fulfilling one often imposes constraints on the others. For example, while the tail must be mechanically robust, it cannot be constructed from steel or nickel-based alloys due to their magnetic properties and the availability of materials with superior thermal conductivity at cryogenic temperatures. As a result, design compromises are frequently necessary, and these trade-offs are guided by the particular demands of the experiments to be conducted using the tail.

Electrical and Magnetic Requirements

It is essential that the entire tail assembly be constructed from non-magnetic materials. Additionally, the experimental wiring connecting the MC plate to the base plate must satisfy several criteria: it should be non-magnetic, exhibit high electrical and thermal conductivity, and minimize nuclear demagnetization effects[10]. Furthermore, the wiring layout must accommodate the potential integration of cryogenic RC filters.

Structural Requirements

To ensure mechanical stability, the tail must be structurally rigid so that transmitted vibrations result in minimal displacement of the samples relative to the cryostat's main axis. This requirement is met by employing three vertically mounted, drilled support plates instead of circular rods to hold the base plate (see Section 3.3.2). In addition to providing enhanced stiffness, these vertical plates facilitate the integration of additional hardware and offer flat surfaces that are more effective for thermal anchoring compared to cylindrical geometries (see below).

The wiring must also be mechanically robust and securely fastened to the structural elements of the tail. This minimizes the risk of wire movement in the presence of magnetic fields, which could otherwise expose the charge carriers in the wires to spatial variations in the magnetic field[11], potentially inducing eddy currents and noise into the measurements.

Furthermore, the tail must be modular and easy to install or remove. This is

---

[10] This requirement does not apply to the wiring used for devices mounted directly on the MC plate. The headers located on the MC plate are intended for preliminary device testing or for experiments that do not involve magnetic fields.

[11] The magnetic field is not uniformly distributed along the length of the tail.

particularly important because a second tail, designed for high-frequency microwave applications, was also constructed for use with the Triton system. Consequently, a mechanism is required to allow for the straightforward connection and disconnection of the DC wiring without exerting mechanical stress on the tail-side connectors. Given the stiffness of the tail-side wiring, it is crucial to minimize movement of the CINCH connectors that link the superconducting DC lines and the tail wiring, in order to prevent mechanical failure at the solder joints (see Section 3.3.3).

Thermal Requirements

Rapid thermalization of the tail to the MC plate is essential for maintaining thermal stability during experiments. Thermally, the tail can be modeled as a series of components: the base plate in series with three drilled plates arranged in parallel, which together are in series with the adapter. The thermalization time τ can be estimated as

$$\tau = \frac{K_{\text{adapter}}^{-1} + K_{\text{base plate}}^{-1} + \left(3K_{\text{drilled plate}}\right)^{-1}}{C_{\text{adapter}}^{-1} + C_{\text{base plate}}^{-1} + \left(3C_{\text{drilled plate}}\right)^{-1}}, \tag{3.1}$$

where C_i and K_i denote the heat capacity and thermal conductance of component i, respectively. To minimize τ, materials with high thermal conductance and low heat capacity should be selected for each component. This is crucial for ensuring that the tail reaches thermal equilibrium with the MC plate as quickly as possible. The Triton tail we designed has an estimated thermalization time of $\tau = 0.6$ ms.

Minimizing eddy current generation within the tail is also a critical design consideration. This can be achieved by optimizing three key factors: the material, geometry, and volume of conductive components. Reducing the volume of conductive material directly decreases the magnitude of eddy currents; thus, drilling multiple holes in the vertical support plates is an effective strategy for mitigation. From a geometrical standpoint, potential current loops in planes perpendicular to the applied magnetic field are disrupted by introducing slits into the base plate. These slits break the continuity of conductive paths that would otherwise support circulating eddy currents. A more detailed analysis and approximations of eddy current heating effects are provided in Appendix B.

Achieving effective electron thermalization at cryogenic temperatures remains as much an art as a science. Various research groups employ different techniques to thermally anchor their wiring to the MC plate, reflecting the lack of a universally optimal method. However, a widely accepted rule of thumb is that the thermal contact area between the wires and the MC plate should be maximized. Increasing this contact surface enhances phonon coupling and improves the efficiency of heat transfer from the electrons in the wires to the cryogenic environment.

3.3.2 Materials Selection

Selecting appropriate materials for the tail involves balancing the various design requirements discussed above, with compromises made based on their relative importance to the specific experiments conducted in the cryostat. In some cases, certain constraints can be relaxed to better satisfy more critical requirements.

The base plate of the tail is fabricated from pure silver to minimize nuclear demagnetization effects. To reduce eddy current heating, slits and holes are machined into the plate to eliminate conductive loops and reduce material volume. As with all components of the sample holder, the base plate is gold-coated to enhance thermal contact at interfaces. Notably, substituting pure silver with coin silver for the base plate increases the estimated thermalization time by a factor of eight, underscoring the importance of material purity in achieving efficient thermal anchoring.

The base plate is mechanically supported by three drilled plates made of coin silver — a silver-copper alloy chosen for its superior structural strength. Plates are used instead of rods to increase the rigidity of the tail and to provide flat surfaces for mounting the wiring heat sinks (see Section 3.3.3). These heat sinks are installed on the top surfaces of the drilled plates, on the interior side of the tail. Like the adapter and CINCH plates, the heat sinks are made from oxygen-free high-conductivity

(OFHC) copper. The key physical properties of these materials are summarized in Table 3.3.

	Density (g/m^3)	Magnetic Field (T)	Electrical Resistivity (Ω m)	Thermal Conductivity (W/Km)	Specific Heat (J/gK)
Coin Silver (10% Cu)	1.02×10^{7}	6	2.92×10^{-9}	7.912	-
		0	2.70×10^{-9}	11.80	1.60×10^{-5}
Copper (OFHC)	8.94×10^{6}	6	4.60×10^{-11}	-	-
		0	1.80×10^{-11}	642.3	9.94×10^{-5}
Silver (5N)	1.05×10^{7}	0	7.02×10^{-7}	41.4	1.23×10^{-4}

Table 3.3: Key properties of the materials used in the construction of the Triton tail. Density values are reported at 293.15K, while electrical resistivity, thermal conductivity, and specific heat are provided at 4 K. The properties of coin silver are sourced from Ref. [98]. The density and electrical resistivity of copper are taken from Refs. [99, 100], while its thermal conductivity and specific heat are obtained from Ref. [101]. The corresponding properties for silver are drawn from Refs. [102–105].

3.3.3 Custom Experimental Wiring and Thermalization

The experimental wiring in the tail connects the device headers to the cryostat's superconducting wiring looms. Here, the design rationale, material selection, thermal anchoring strategy, and modularity of the wiring system are outlined.

Since the cryostat is used to test drag devices, the tail must accommodate as many devices as possible. Each vertically integrated drag device requires 12 wires — four for gate control, and eight for ohmic contacts. Since the Triton's DC wiring is organized into looms of 24 wires, it was natural to adopt 24-pin headers on the tail, in contrast to the 8- or 16-pin headers used in other cryostats in Gervais Lab. The tail includes four 24-pin headers, with an additional four 24-pin headers mounted on the MC plate for preliminary testing or for experiments that do not require magnetic fields.

The wiring is composed of annealed 4N (99.99%) silver wires with a diameter of 0.643 mm, chosen for their high electrical conductivity and mechanical rigidity.

Silver is preferred over copper in the tail to avoid nuclear demagnetization effects. The wires are arranged in twisted pairs and soldered to CINCH connectors and sample headers using Sn60-Pb40 solder, which is then coated with silver paint. This combination is selected for its mechanical robustness across multiple thermal cycles and for its enhanced thermal conductivity at cryogenic temperatures. Although Sn60-Pb40 solder becomes superconducting below 7.05 K [106], resulting in poor thermal conductivity in zero magnetic field, the silver paint mitigates this limitation. On the MC plate, copper wires of the same diameter are used, as magnetic effects are not a concern in that region.

To ensure effective thermal anchoring, each 24-wire bundle is thermally anchored using custom-made sintered silver heat sinks housed in gold-plated OFHC copper enclosures. These heat sinks are mounted on the vertical, gold-plated coin silver drilled plates. They are fabricated by pressing silver powder around the wires in successive layers to achieve a packing density of approximately 50% pure silver. Given the excellent thermal conductivity of silver (see Table 3.3), this design ensures that each wire maintains good thermal contact with the MC plate for the entire length of the heat sink.

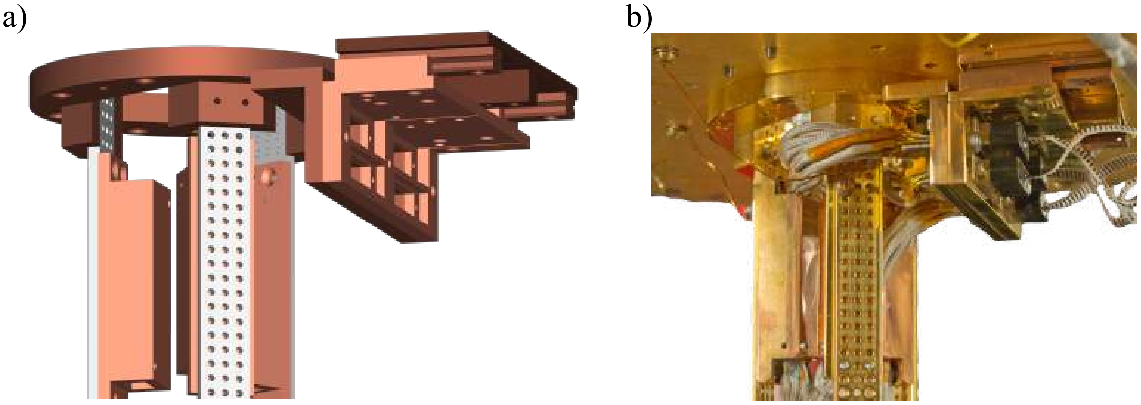

Figure 3.5: Connecting/disconnecting mechanism for the tail wiring. a) Schematic. b) Picture of the mechanism mounted on the Triton. No RC filters mounted

As outlined in the design requirements, the tail wiring must withstand frequent connection and disconnection cycles without degradation. The tail wiring is connected to the cryostat superconducting wire loom with CINCH connectors. The 8 CINCH connectors are fixed to two support plates — one fixed to the tail and the other to the MC plate (see Fig. 3.5). The support plate on the tail is rigidly attached to the tail's adapter plate, ensuring that the wiring remains undisturbed during tail removal or installation. Meanwhile, the support plate on the MC plate is mounted on a rail system, allowing for smooth and reliable engagement and disengagement of the connectors. The optional RC filters are mounted on the support plate on the MC plate side. The system is specifically designed to accommodate the Therma-uD25-G-L RC filter modules from Aivon.

4

Sample Fabrication

The first cleanroom was developed in 1960 by Willis Whitfield, an engineer at Sandia National Laboratories (SNL). At the time, Whitfield was working in a division responsible for manufacturing components used in nuclear weapons and was confronted with persistent contamination issues. As a solution, he designed a room in which clean air is pushed downward from the ceiling and evacuated through the floor, creating a laminar airflow in which any contaminent would be immediately dragged out of the room [107]. This innovation was rapidly adopted across various industries, including aerospace, pharmaceuticals, surgery, and semiconductor manufacturing. The fabrication of vertically integrated QWs would not be possible without a cleanroom and without the Center for Integrated Nano Technologies (CINT) located at SNL. This chapter describes the fabrication process of these devices. It begins by quickly introducing how the double quantum well wafer is fabricated, followed by a detailed summary of the nanofabrication steps, with a particular focus on the differences from the process developed by Laroche [76], a former PhD student in the Gervais group.

4.1 The Bilayer Structure

Before electrons can be confined to one dimension, their motion must be restricted to a two-dimensional (2D) plane. MBE is a powerful technique for achieving this, as it enables the growth of atomically precise, ultra-clean heterostructures in which electrons can be confined to one or more 2D layers. MBE allows for the deposition of thin films composed of various materials with distinct electronic properties, stacked with sub-nanometer precision.

Among the many material systems available, the GaAs/AlAs pair stands out for low-dimensional electronic transport experiments. Gallium arsenide (GaAs) is a semiconductor with a bandgap of 1.52 eV, while aluminum arsenide (AlAs) is a near-insulator with a wider bandgap of 3.13 eV. Alloys of these materials, such as $\mathrm{Al}_x\mathrm{Ga}_{1-x}\mathrm{As}$, offer tunable bandgaps depending on the aluminum concentration[1]. Moreover, GaAs and AlAs exhibit an exceptionally low lattice mismatch, resulting in nearly defect-free interfaces. For these reasons, the base material for our device fabrication is a modulation-doped GaAs/AlGaAs heterostructure grown by MBE.

By alternating layers of low-bandgap GaAs and tunable-bandgap AlGaAs, and incorporating dopants, a quantum well can be formed along the growth direction[2]. The quantum well itself is formed within a GaAs layer. Although GaAs is a semiconductor and would not conduct electrons on its own, when sandwiched between AlGaAs layers and appropriately doped, its conduction band can be lowered below the Fermi level, enabling electron conduction. Low temperatures are required to ensure that the thermal energy of the electrons remain below the energy of the first

---

[1] The bandgap increases with higher aluminum content.

[2] The devices used in this work are modulation-doped with silicon donors. In modulation doping, dopants are placed outside the quantum well, thereby reducing charge carrier scattering from ionized impurities.

quantized subband in the well, to support the formation of a 2DEG.

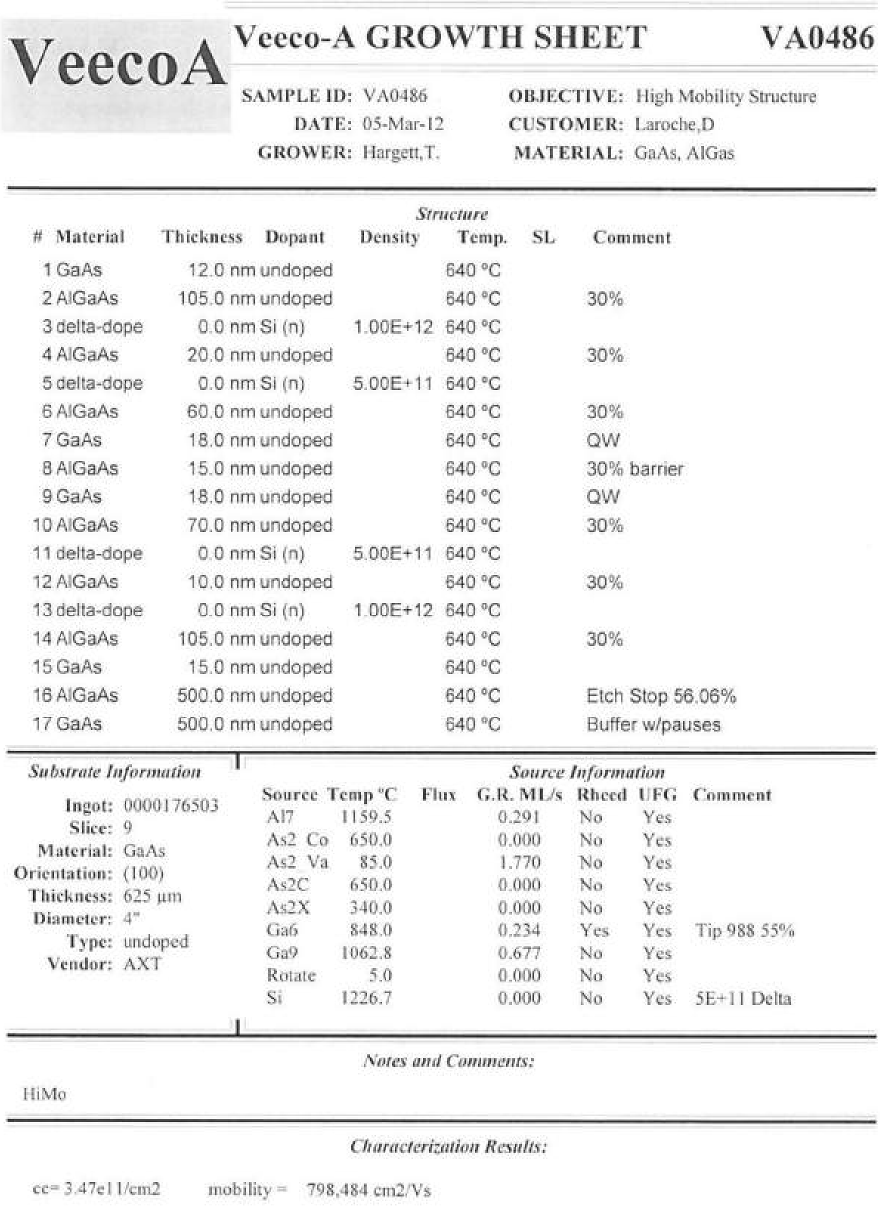

VeecoA

Veeco-A GROWTH SHEET **VA0486**

SAMPLE ID: VA0486
DATE: 05-Mar-12
GROWER: Hargett,T.
OBJECTIVE: High Mobility Structure
CUSTOMER: Laroche,D
MATERIAL: GaAs, AlGas

Structure

#	Material	Thickness	Dopant	Density	Temp.	SL	Comment
1	GaAs	12.0 nm	undoped		640 °C		
2	AlGaAs	105.0 nm	undoped		640 °C		30%
3	delta-dope	0.0 nm	Si (n)	1.00E+12	640 °C		
4	AlGaAs	20.0 nm	undoped		640 °C		30%
5	delta-dope	0.0 nm	Si (n)	5.00E+11	640 °C		
6	AlGaAs	60.0 nm	undoped		640 °C		30%
7	GaAs	18.0 nm	undoped		640 °C		QW
8	AlGaAs	15.0 nm	undoped		640 °C		30% barrier
9	GaAs	18.0 nm	undoped		640 °C		QW
10	AlGaAs	70.0 nm	undoped		640 °C		30%
11	delta-dope	0.0 nm	Si (n)	5.00E+11	640 °C		
12	AlGaAs	10.0 nm	undoped		640 °C		30%
13	delta-dope	0.0 nm	Si (n)	1.00E+12	640 °C		
14	AlGaAs	105.0 nm	undoped		640 °C		30%
15	GaAs	15.0 nm	undoped		640 °C		
16	AlGaAs	500.0 nm	undoped		640 °C		Etch Stop 56.06%
17	GaAs	500.0 nm	undoped		640 °C		Buffer w/pauses

Substrate Information

Ingot: 0000176503
Slice: 9
Material: GaAs
Orientation: (100)
Thickness: 625 µm
Diameter: 4"
Type: undoped
Vendor: AXT

Source Information

Source	Temp °C	Flux	G.R. ML/s	Rheed	UFG	Comment
Al7	1159.5		0.291	No	Yes	
As2 Co	650.0		0.000	No	Yes	
As2_Va	85.0		1.770	No	Yes	
As2C	650.0		0.000	No	Yes	
As2X	340.0		0.000	No	Yes	
Ga6	848.0		0.234	Yes	Yes	Tip 988 55%
Ga9	1062.8		0.677	No	Yes	
Rotate	5.0		0.000	No	Yes	
Si	1226.7		0.000	No	Yes	5E+11 Delta

Notes and Comments:

HiMo

Characterization Results:

cc= 3.47e11/cm2 mobility = 798,484 cm2/Vs

Figure 4.1: Example growth sheet for wafer VA0486.

An example MBE growth sheet for wafer VA0486 grown at SNL is presented in Fig. 4.1. This wafer, which serves as the primary substrate for the devices discussed in this thesis, features a double quantum well structure (layers 7 and 9), separated by a 30% Al-content AlGaAs barrier (layer 8). A notable feature of this wafer is the inclusion of a 500 nm AlGaAs etch-stop layer with 56% aluminum content, located deep within the structure. This layer is critical for the epoxy bond and stop-etch

(EBASE) step of the fabrication process (see Section 4.2.2).

Before proceeding with the costly and time-intensive fabrication of vertically integrated QWs, it is essential to verify that the wafer contains exactly two quantum wells and to measure the carrier density in each. To this end, a small piece of the wafer is cleaved, and a Hall bar is patterned into the heterostructure. Electrical contacts are deposited and annealed following the procedures described in Section 4.2.1. This Hall bar device is then used to characterize the charge density in the two quantum wells, as discussed in Section 5.1.

4.2 Fabrication of the Vertically Integrated Quantum Wires Devices for Coulomb Drag Measurement

Fabricating these devices requires patterning QWs on both sides of a heterostructure containing two 2D quantum wells. An effective method for achieving this is the epoxy bond and stop-etch (EBASE) technique, originally developed at SNL [108]. The devices presented in this work were fabricated at SNL within the Center for Integrated Nanotechnologies (CINT), and the overall process closely follows the methodology established by Laroche in his earlier work [76].

However, several of the tools and procedures used by Laroche have since been modified or improved, necessitating adaptations to the original process. In this section, we summarize the fabrication steps for a vertically integrated 1D–1D drag device. Key differences between this process and Laroche's original method are then highlighted. A complete fabrication recipe is provided in Appendix C.

As in Laroche's work, the final product of the fabrication process is a chip containing three devices, as illustrated in Fig. 4.2. To increase the likelihood of obtaining multiple functional devices, chips were fabricated in batches of two, three, or four.

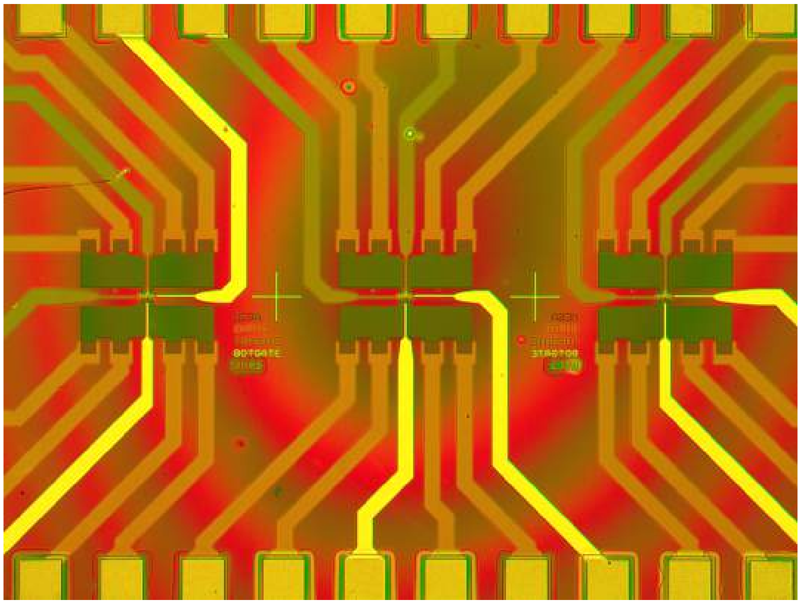

Figure 4.2: Photograph of a completed chip containing three vertically integrated 1D–1D drag devices. This particular chip is from batch 2.

4.2.1 Top Quantum Wire Patterning

The fabrication process begins by cleaving small chips from a double quantum well heterostructure and cleaning them using a standard solvent sequence: acetone, methanol, and isopropanol, followed by nitrogen drying[3]. The chips are then prepared for mesa definition *via* phosphoric acid etching. A photolithographic mask is used to selectively protect the regions that will form the mesa. The phosphoric acid etch is rapid — typically requiring around 30 seconds to etch through both quantum wells, the exact time depending on the heterostructure design[4].

Following the etch, the photoresist is removed by soaking the chip in acetone overnight, then rinsing with methanol and isopropanol, and drying with nitrogen.

---

[3] This cleaning procedure is repeated before every electron-beam or photolithography step.

[4] The goal of this step is to isolate the quantum wells to a small region (the mesa), which can later be electrostatically pinched off using surface gates.

The etch depth is verified using profilometry[5]. If the etch depth is insufficient, a new photolithographic mask is applied and the etch is continued for a few additional seconds until both quantum wells are fully exposed. The result of this step is shown in Fig. 4.3 a), where the mesa is visible at the center of the chip and the exposed quantum wells are in blue.

Next, a new photolithographic mask is applied to define the ohmic contacts. A Ge/Au/Ni/Au metal stack is deposited via electron-beam (e-beam) evaporation to form the contacts to the quantum well, shown in orange in Fig. 4.3 b). After deposition, the chip is soaked in acetone overnight to facilitate liftoff of the unwanted metal. The total thickness of the deposited layers is verified using profilometry; if the thickness deviates from the expected value, the device is discarded. The contacts are then annealed in a rapid thermal annealer to allow the metal to diffuse into the heterostructure and eliminate the Schottky barrier. After annealing, the contacts form ohmic connections to both quantum well.

The top gates are deposited in two steps. First, a photolithography step defines the coarse gate that will connect to the fine gate. Then, an e-beam lithography step defines the fine gates that form the QW. The cleaning and preparation steps for both lithography processes are similar to those described above, with minor differences detailed in Appendix C. The top gates are yellow in Fig. 4.3 c). For each fabrication batch, it is good practice to include a sacrificial device, which can be inspected under a scanning electron microscope (SEM) to verify the quality of the fine gate patterns. Although dose tests are performed weekly during the fabrication process, inspecting one device per batch helps ensure pattern fidelity.

---

[5] Profilometry is used extensively throughout the fabrication process to monitor the depth of all etching and deposition steps. Measurements should be taken at non-critical locations, such as alignment marks or the corners of soldering pads, to avoid damaging functional areas of the device.

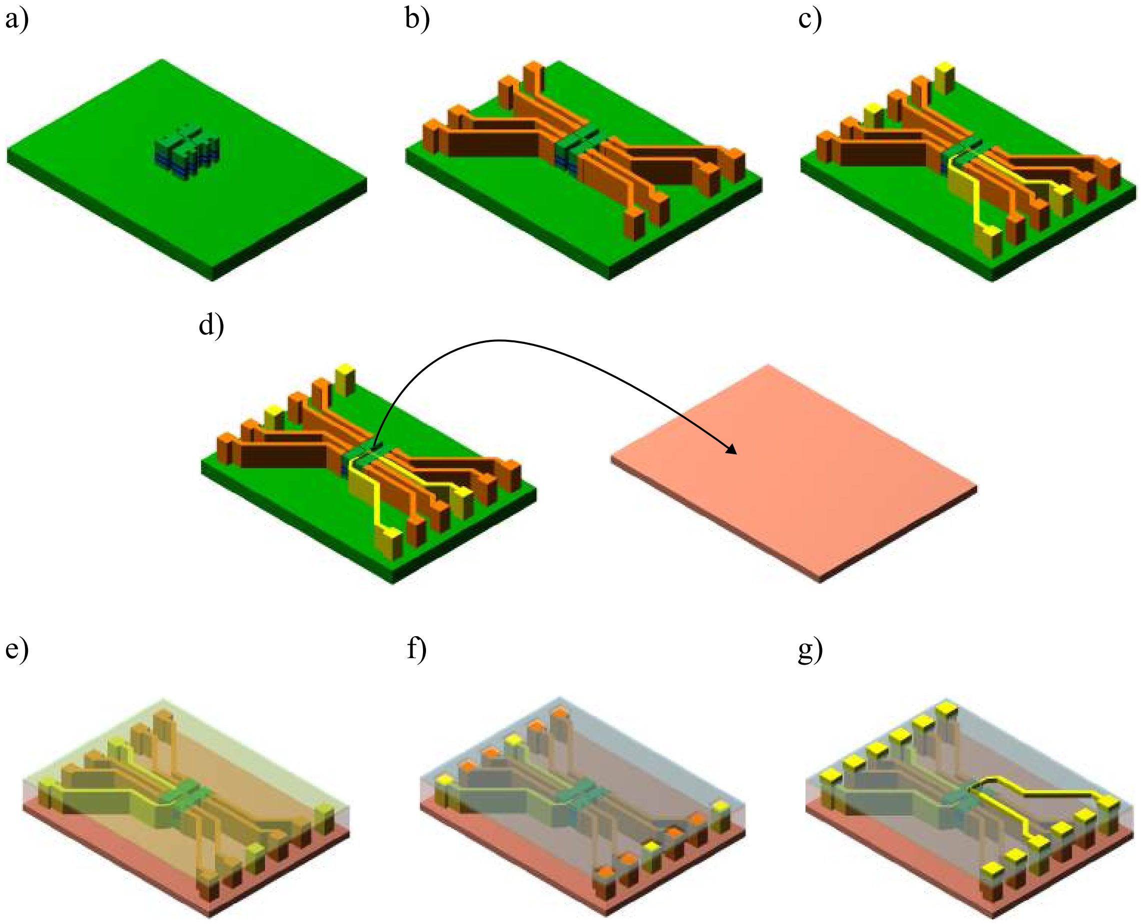

Figure 4.3: Fabrication process of a vertically integrated QWs device (not to scale). a) The mesa is etched in the heterostructure (quantum wells are in blue). b) Contacts (orange) are deposited and annealed. c) Top gates (yellow) are deposited. d) The device is glued to a new GaAs wafer upside down. e) The back of the initial wafer is lapped and etch. f) A thin layer of dielectric is deposited by Atomic layer deposition and vias are etched to expose the soldering pads of the contacts and top gates. g) Bottom gates are deposited.

4.2.2 EBASE Method

The patterned heterostructure, now equipped with the necessary gates to define the top QW, is bonded upside down onto a new GaAs carrier wafer using epoxy. This carrier wafer is represented in pink in Fig. 4.3 d). The back side of the original heterostructure is then mechanically lapped and chemically etched down to the AlGaAs etch-stop layer. At this point, the top gate pattern and QW structure become visible again due to the reduced thickness of the remaining heterostructure, as shown in Fig. 4.3 e).

To prevent electrical leakage between the bottom and top gates — particularly through pinholes introduced by the multiple wet etching steps — a thin dielectric layer is deposited over the entire device. Vias[6] are then etched through this dielectric to expose the soldering pads for the ohmic contacts and top gates, as illustrated in Fig. 4.3 f).

4.2.3 Bottom Quantum Wire Patterning

The patterning of the bottom gates follows the same procedure as that used for the top gates. However, due to the presence of a dielectric layer on the device at this stage, the optimal e-beam lithography dose may differ slightly from that used for the top gate patterning. To account for this, a sacrificial device is useful to calibrate the exposure dose and to verify the alignment between the top and bottom gates. An example of such alignment verification is shown in Fig. 4.4.

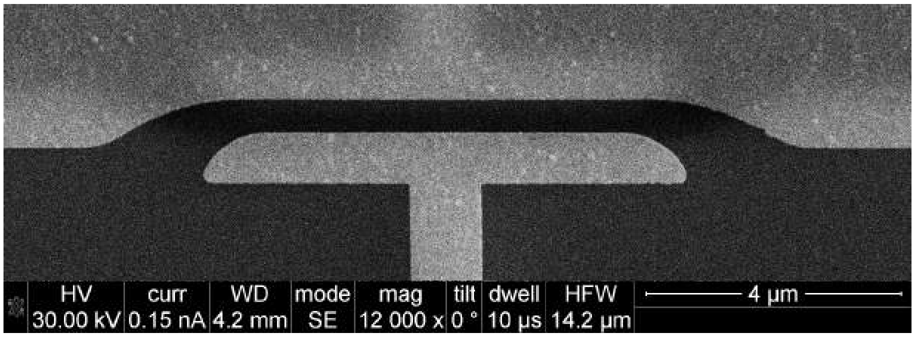

Figure 4.4: Scanning electron microscope (SEM) image of the gate structure on a sacrificial device from batch 28, written with an e-beam dose of 220 μC/cm^2. The bottom gates are in focus, while the top gates — located deeper within the device — appear blurred. The bottom plunger (BPL) gate is visible in the lower portion of the image, and the bottom pinch-off (BPO) gate is partially visible at the top. The QW forms in the heterostructure between these two gates.

---

[6] Vias are vertically oriented pathways in integrated circuits often employed to establish electrical connections between different heterostructure layers.

4.2.4 Differences from Laroche's Process

Four fabrication steps were updated to comply with new regulations at CINT and to take advantage of the modernized equipment now available: photolithography, e-beam lithography, e-beam metal deposition, and mechanical lapping. In addition, new masks were designed to improve the alignment accuracy of the various device components. The updated e-beam lithography process now utilizes four alignment marks per device, while the photolithography process employs eight alignment marks per chip.

Photolithography

CINT recently acquired a maskless aligner, the MLA150 from Heidelberg Instruments, which enables ultraviolet (UV) photolithography on small chips without the need for physical masks. The MLA150 was used in place of traditional mask-based lithography to reduce the risk of introducing impurities into the photoresist, which can occur through direct contact with physical masks. Given the large number of photolithography steps involved in the fabrication process, the use of the MLA150 significantly improved the reproducibility and cleanliness of the patterning. Detailed procedures for photolithography using the MLA150 are provided in the full fabrication recipe in Appendix C.

E-beam Lithography

Due to updated health and safety regulations in the CINT Integration Laboratory, the e-beam resist used in the fabrication process was changed from PMMA 495 C-4 to PMMA 495 A-6. The new resist formulation is processed by baking at 180 °C for 90 seconds. This adjustment ensures compliance with current laboratory standards while maintaining compatibility with the existing lithography workflow.

E-beam Metal Deposition

The metal deposition system previously employed by Laroche was unavailable during this work. Instead, a comparable e-beam deposition system was utilized successfully. E-beam deposition processes are known for their reproducibility across different systems, provided that the vacuum conditions are equivalent and the quartz crystal monitor is relatively new.

Lapping

A new lapping and polishing system from Allied was acquired by CINT to enhance sample preparation capabilities. This upgraded tool improves the automation and reproducibility of the lapping process through the integration of an onboard micrometer gauge, which allows for precise control of material removal. For this work, a single grade of polishing paper was employed — 600 grit, 15 microns.

5

Device Characterization

The characterization of a Coulomb drag device entails a sequence of critical steps designed to ensure the integrity and functionality of the system. The process begins with the determination of the electron density and mobility in the 2DEG using the SdH oscillation frequency. Subsequently, the ohmic contacts are evaluated to identify those with the lowest resistance, and the existence of two distinct 2DEGs is confirmed via pinch-off measurements. Independent electrical access to each 2DEG is then verified through tunneling spectroscopy. Following this, the subband structure of each QW is identified. The final step involves the measurement and validation of the Coulomb drag signal.

This chapter details the characterization methodology applied to vertically integrated QW devices employed in Coulomb drag experiments. While several devices were fabricated and tested, the results presented herein focus exclusively on device

B28C1-C, selected for its representative behavior and to maintain clarity and consistency throughout the discussion.

5.1 Characterization of Heterostructure

Before initiating the costly fabrication process of vertically integrated QWs, verifying that the wafer contains exactly two quantum wells and determining their respective electron densities is essential. To this end, a small piece of the wafer is cleaved, and a Hall bar is patterned onto the heterostructure. Ohmic contacts are then deposited and annealed following the procedures described in Sec. 4.2.1. The device is subsequently cooled to approximately 16 mK, and its resistance is measured as a function of an increasing magnetic field applied perpendicularly to the plane of the device.

The magnetoresistance of a Hall bar fabricated from the VA0486 wafer is shown in Fig. 5.1 a). From the low-field SdH oscillation frequency, the electron density of a 2DEG, denoted as n_e, can be extracted using Eq. 2.2,

$$n_e = f_B \frac{e}{h}.$$

In a bilayer system, two distinct 2DEG densities result in two superimposed oscillation frequencies, producing a characteristic beating pattern, as observed in Fig. 5.1 b). This confirms the presence of two quantum wells. Performing a Fourier transform of the magnetoresistance signal reveals two principal frequency components, corresponding to the spin-degenerate frequencies, as indicated by the blue dashed lines in Fig. 5.1 c). When calculating the electron densities, these frequencies must be multiplied by a factor of two to account for spin degeneracy.

Additional peaks corresponding to frequencies where spin degeneracy is lifted (red dashed lines) also appear in the Fourier spectrum due to the inclusion of data

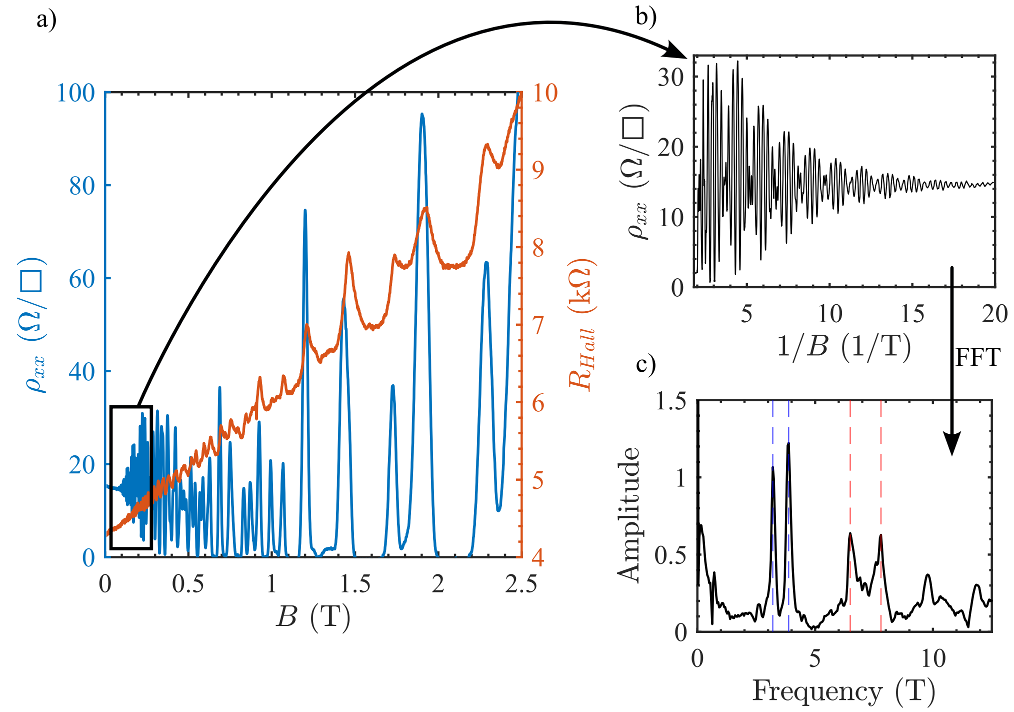

Figure 5.1: Density measurement technique for a bilayer system using data from wafer VA0486. a) Longitudinal resistivity and Hall resistance as functions of the perpendicular magnetic field. b) Longitudinal resistivity plotted as a function of the inverse magnetic field $1/B$ in the low-field regime, highlighting the SdH oscillations. c) Fourier transform of the data in panel b). The vertical axis represents the amplitude of the spectral components. Blue dashed lines indicate the spin-degenerate frequencies of the two layers, while red dashed lines denote the spin-resolved components arising from spin degeneracy lifting at higher magnetic fields.

from magnetic field ranges where spin degeneracy is lifted[1]. Using Eq. 2.2, the extracted electron densities for the two 2DEGs are 1.57×10^{11} cm^{-2} and 1.88×10^{11} cm^{-2}.

Finally, the zero-field resistivity provides a means to extract the combined mobility of the bilayer system, given by

$$\mu_{combined} = \frac{n_1 e \mu_1 + n_2 e \mu_2}{(n_1 + n_2)e} = \frac{1}{\rho_{xx}(n_1 + n_2)e}, \tag{5.1}$$

---

[1] There exist several established techniques for determining the electron density in single-layer 2DEG structures (see, for example, Refs. [97, 109]). However, these methods are not well-suited for bilayer systems due to their inability to resolve the individual contributions from each layer. Consequently, a Fourier transform-based approach was employed to extract the density information in the bilayer configuration.

where μ_i and n_i denote the mobility and electron density of layer $i = 1, 2$, respectively. For wafer VA0486, the combined mobility is found to be $\mu_{combined} = 1.51 \times 10^6$ cm^2/sV. With the electron densities and mobilities now established, the fabrication of the device can proceed as described in Sec. 4.2, followed by the characterization of its transport properties.

5.2 Contacts and Pinch-off

Drag devices are fabricated with eight electrical contacts — four per wire — to maximize the likelihood of obtaining at least two good contacts per wire. The initial step in characterizing these devices involves evaluating the quality of the contacts. This is achieved by measuring the resistance between all possible pairs of contacts. The measurement setup used for this characterization is illustrated in Fig. 5.2 a).

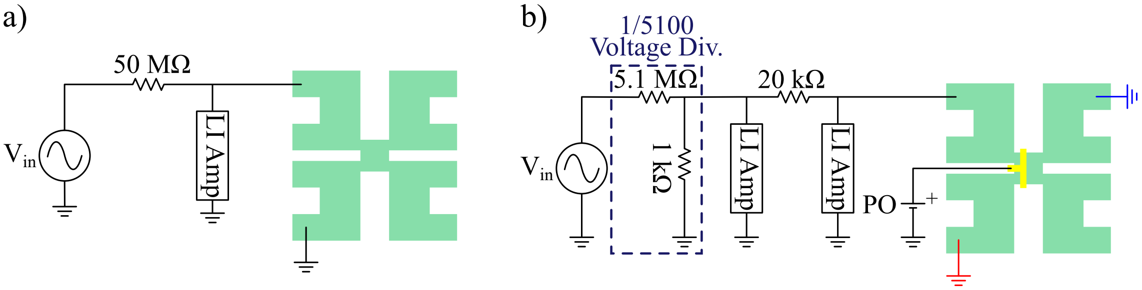

Figure 5.2: a) Contacts measurement circuit. b) Pinch-off measurement circuit. A sinusoidal signal at 54.32 Hz, generated by an SR830 lock-in amplifier (LI Amp), is used as the input excitation in both measurement circuits. The signal has a root-mean-square (RMS) amplitude of $V_{in} = 1$ V. The gate voltages are applied using a Keithley 2400 SourceMeter unit, enabling simultaneous monitoring of gate leakage currents during the measurements.

Once the optimal contact configuration has been established, the next step is to characterize the device's response to the two pinch-off (PO) gates. These gates are designed to deplete the 2DEG closest to each gate across the entire mesa without affecting the more distant 2DEG. When both the top (TPO) and bottom (BPO) gates are appropriately biased, the top and bottom 2DEGs can be independently connected to four terminals each. To fully characterize the PO gates, it is therefore essential to verify that both the TPO and BPO gates can fully pinch-off the 2DEGs in two directions: perpendicular to the QWs, and parallel to the QWs[2]. This verification is performed using the circuit shown in Fig. 5.2 b), where the blue ground configuration is used for measurements in the perpendicular direction, and the red ground configuration is used for the parallel direction.

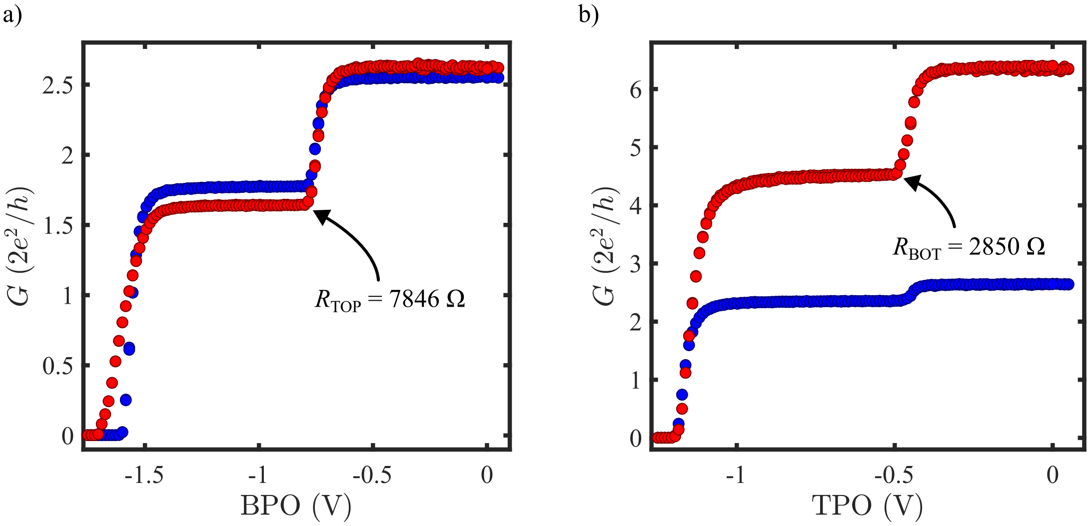

Figure 5.3: Pinch-off measurement data for device B28C1-C. Parallel measurements are shown in red, and perpendicular measurements are shown in blue. a) Sweep of the bottom pinch-off (BPO) gate. b) Sweep of the top pinch-off (TPO) gate. In panel b), the parallel measurement exhibits significantly higher conductance than the other traces. This is attributed to one of the contacts on the top wire side having a substantially higher resistance than the others. Since the conductance in the TPO gate sweep is measured using the bottom wire contacts, this asymmetry in contact resistance affects the observed signal here. The only configuration not using this higher resistance contact is the perpendicular (blue) one in b).

Pinch-off measurements are presented in Fig. 5.3 for device B28C1-C, with panel a) showing the bottom pinch-off (BPO) gate sweep and panel b) the top pinch-off (TPO) gate sweep. Two distinct conductance plateaus are observed as the BPO or TPO gate voltage is swept toward negative values. The higher plateau corresponds to the conductance of two parallel 2DEGs, while the lower plateau reflects the conductance of a single 2DEG.

The lowest conductance plateau in the parallel configuration provides a direct

---

[2] For example, to confirm both the presence of two distinct 2DEGs and the proper functioning of the gate, the TPO gate must be capable of fully pinching off both 2DEGs in the direction parallel to the QW when conductance is measured using the bottom QW contacts.

measurement of the total series resistance, which includes both the resistance of the remaining 2DEG and the wiring resistance[3]. Red data points represent measurements taken in the parallel configuration, while blue points correspond to the perpendicular configuration.

During the sweep, the current flowing through the gate is also monitored to ensure that the PO gates are not leaking[4]. A device is considered to pass the contact and PO gate characterization step if the following conditions are met: no gate leakage current exceeding a few nanoamperes is detected, exactly two conductance plateaus are observed, and the total resistance of any 2DEG, including wiring is, less than 12 kΩ [5]. Devices may fail this characterization step in various ways. Appendix E provides a comprehensive list of observed failure modes.

5.3 Tunneling

The proximity of the two 2DEGs plays a critical role in determining the tunneling behavior between them. As the separation between the layers decreases, a correspondingly higher potential barrier is required to effectively suppress interlayer tunneling. Given that tunneling resistance decreases exponentially with decreasing barrier width, precise control over both the width and height of the barrier is essential. These parameters are defined during the heterostructure growth process. Consequently, experimental verification of the barrier's effectiveness is necessary to ensure that tunneling remains negligible and does not interfere with the Coulomb drag measurements.

---

[3] This value will be used in later subband measurements, where it is subtracted from the total measured conductance to reveal evenly spaced conductance plateaus corresponding to the quantized subbands of the QWs.

[4] Leakage tests are also performed on the plunger (PL) gates using the Keithley 2400 SourceMeter in the same configuration.

[5] A threshold of kΩ is chosen because higher resistances would hinder the resolution of a single quantum of conductance, thereby limiting the ability to observe quantized transport phenomena.

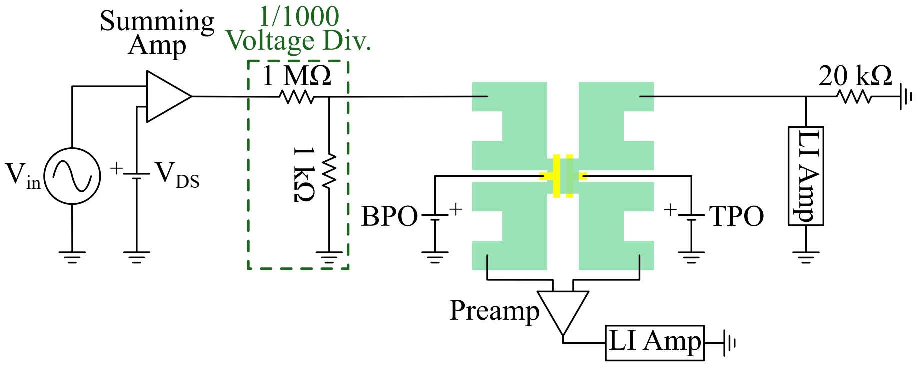

Figure 5.4: Tunneling measurement circuit. The AC input signal is a sine wave of 54.32 Hz with a RMS amplitude of $V_{in} = 0.3$ V. A DC drain-source voltage, V_{DS}, ranging from -2 V to 2 V, is generated using a GS610 source measure unit (Yokogawa) and combined to the input signal via a summing amplifier. The summing amplifier is a SIM980 module, and the preamplifier is a SIM910 module, both from Stanford Research Systems (SRS). Gate voltages are supplied by two SIM928 isolated voltage sources, also from SRS[6].

Negative voltages are applied to the TPO and BPO gates to assess the effectiveness of the interlayer barrier and to identify the gate potentials that maximize the resistance between the two 2DEGs. This characterization is performed using the transconductance measurement circuit shown in Fig. 5.4. The pinch-off (PO) sweep data, presented in Fig. 5.3, serves as an initial reference for selecting appropriate gate voltages. As illustrated in Fig. 5.3 a), the BPO gate begins to deplete the bottom 2DEG at approximately 0.8 V, while Fig. 5.3 b) indicates that the TPO gate pinches off the top 2DEG at around 0.48 V. Tunneling characterization is therefore conducted in the vicinity of these gate voltages.

Tunneling transconductance measurements for device B28C1-C are presented in Fig. 5.5. Our criterion for negligible tunneling is that the resistance between the two 2DEGs must exceed 10 MΩ when a bias voltage of 1 mV is applied across them. This condition corresponds to the yellow region in Fig. 5.5. The data shows that

---

[6] The SIM928 is an isolated voltage source that generates its DC output using internal batteries, making it currently one of the cleanest voltage sources available in its price range. Although it does not provide current measurement functionality, this limitation is not critical in our setup, as gate leakage has already been characterized and confirmed to be negligible. As an isolated source, the SIM928 requires its negative terminal to be referenced to the same ground as the rest of the circuit to ensure that a well-defined and stable potential is applied to the gates.

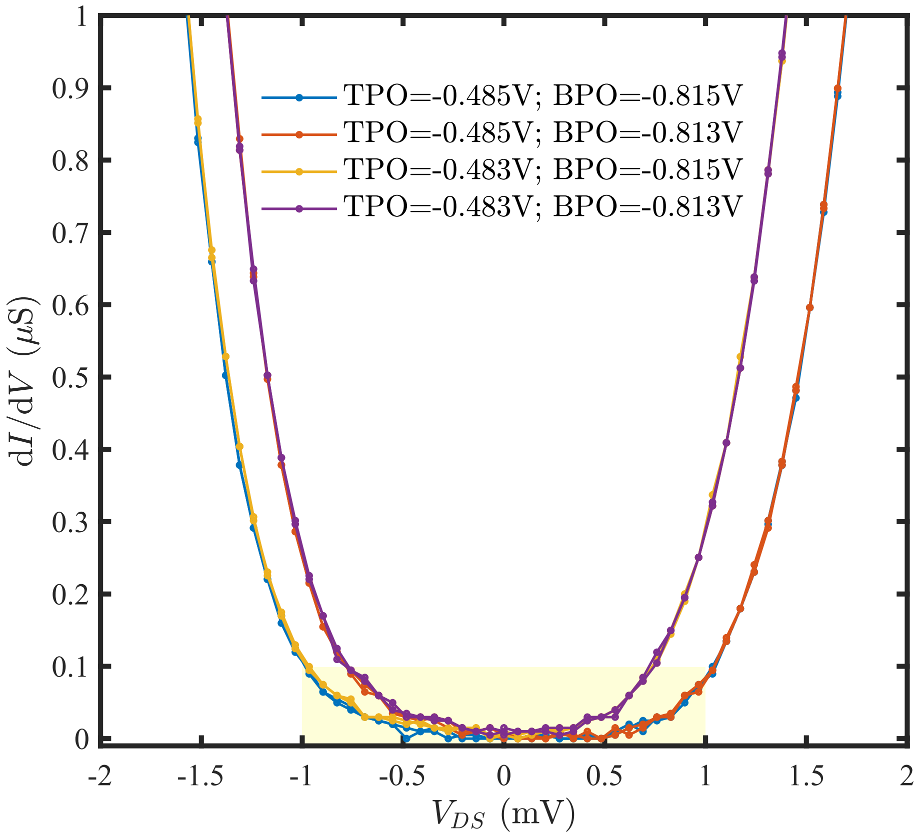

Figure 5.5: Tunneling transconductance measurement for device B28C1-C. The yellow region indicates the parameter space where the tunneling resistance between the two 2DEGs exceeds 10 MΩ under an applied bias of 1 mV, satisfying the criterion for negligible interlayer tunneling.

the only PO gate voltages satisfying this criterion are TPO = -0.485 V and BPO = -0.815 V. Gate voltages more negative than these values will also meet the tunneling criterion, resulting in two electrically isolated 2DEGs. However, lowering the gate voltages further depletes the 2DEG beneath the gates, thereby increasing the lateral separation between the undepleted regions and, consequently, the minimum achievable distance between the QWs. Since maximizing the Coulomb drag effect requires minimizing the interwire separation, the optimal PO gate voltages are the smallest negative values that still satisfy the tunneling suppression criterion.

5.4 Subbands and Their Linearities

With the effect of the PO gates characterized and their optimal voltages determined, the PO gate will typically always be activated to these potentials during all subsequent measurements. Characterization of the plunger (PL) gates can now proceed. Since the plunger gates define the QWs themselves (see Fig. 4.4), their characterization is integral to understanding the QWs behavior. This is performed using two distinct measurement circuits, as shown in Fig. 5.6. Circuit a) is used to map the subband structure of both wires as a function of the top and bottom plunger gate voltages (TPL and BPL) while circuit b) is used to confirm the subband features and assess their linearity.

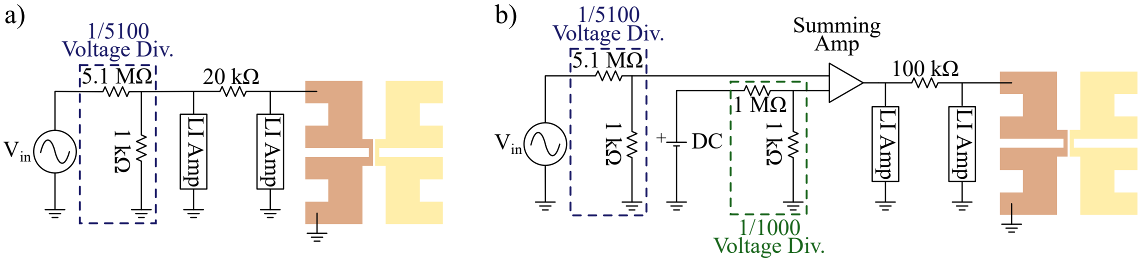

Figure 5.6: Subband characterization circuits. a) Subband mapping circuit. Both QWs are measured simultaneously using two distinct AC signals at 54.32 Hz and 43.21 Hz. b) Subband linearity measurement circuit. The summing amp is a SIM980; all DC voltage sources are SIM928 units. In both circuits, the RMS amplitude of the input signal is $V_{in} = 0.3$ V.

5.4.1 Subband Mapping

To characterize the subband structure of the two QWs, simultaneous conductance measurements in each wire using distinct excitation frequencies while independently varying the potential applied to the two PL gates are performed[7]. The conductances of the top and bottom QWs in device B28C1-C are presented in Fig. 5.7 panels a) and b), respectively. To gain further insight into the subband structure, the

---

[7] The TPL and BPL mesh is determined through an initial coarse square mapping of the conductance in both wires. This provides an estimate of the PL voltage ranges where the conductance is non-negligible in each wire.

derivatives of the conductances with respect to the corresponding PL gate voltage are computed. These derivatives, which more clearly reveal the onset of subbands, are shown in panels c), d), e), and f) of Fig. 5.7.

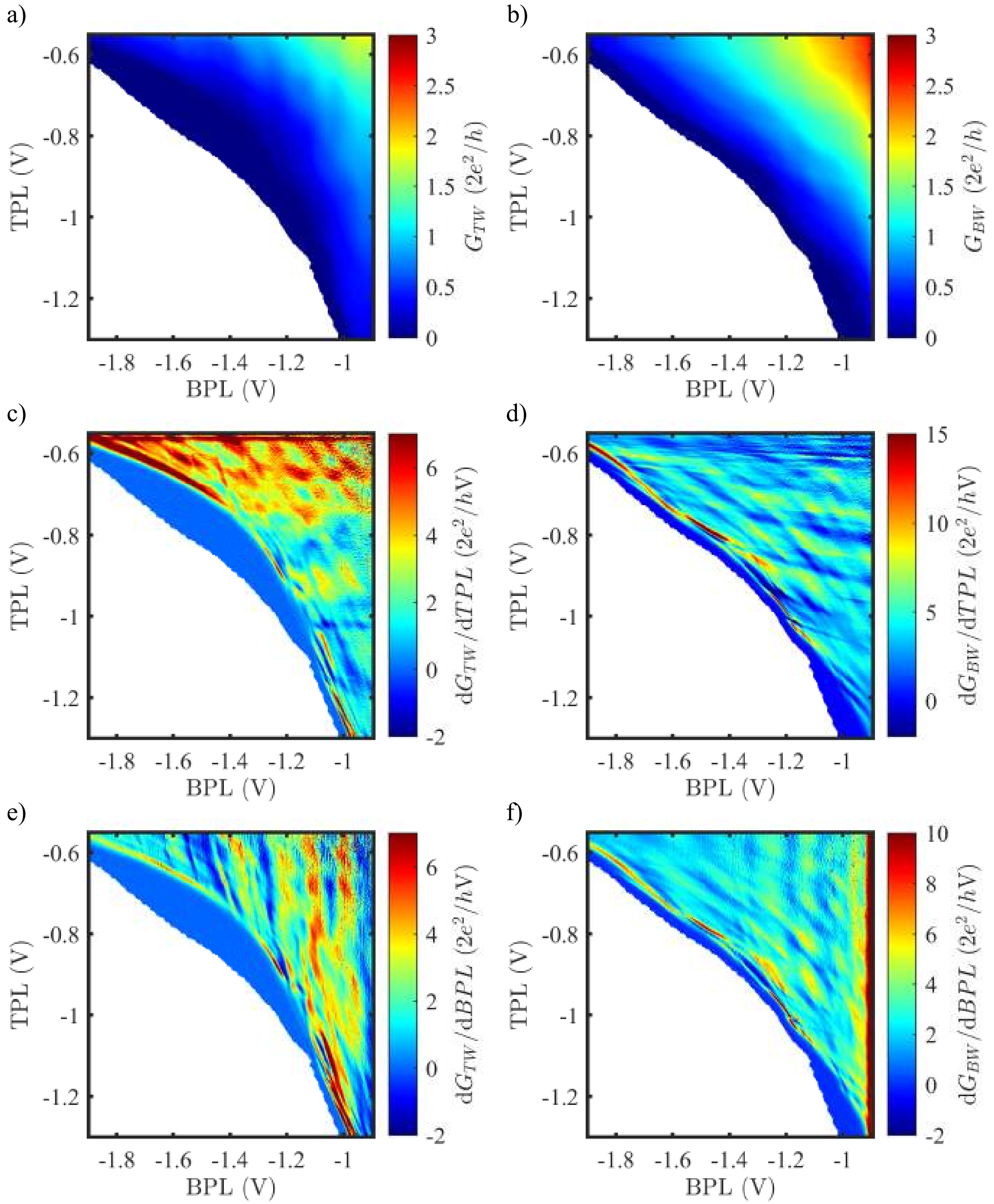

Figure 5.7: Subband mapping. a) and b) Conductances of the top and bottom wires, respectively, as a function of PL gate voltages. The conductance values have been corrected for series resistance contributions from the wiring and the 2DEG, as determined from the PO gate sweep. c) and d) Derivatives of the conductances of the top and bottom wires, respectively, with respect to TPL voltage. e) and f) Derivatives of the conductances of the top and bottom wires, respectively, with respect to BPL voltage.

An interesting regime previously studied by Laroche occurs when both QWs are tuned to their first subbands simultaneously [76]. In device B28C1-C, a region where not only the first subbands are aligned, but the second subbands also coincide, was identified and is shown in Fig. 5.8. The subbands are identified by locating evenly spaced conductance plateaus in the QW conductance traces.

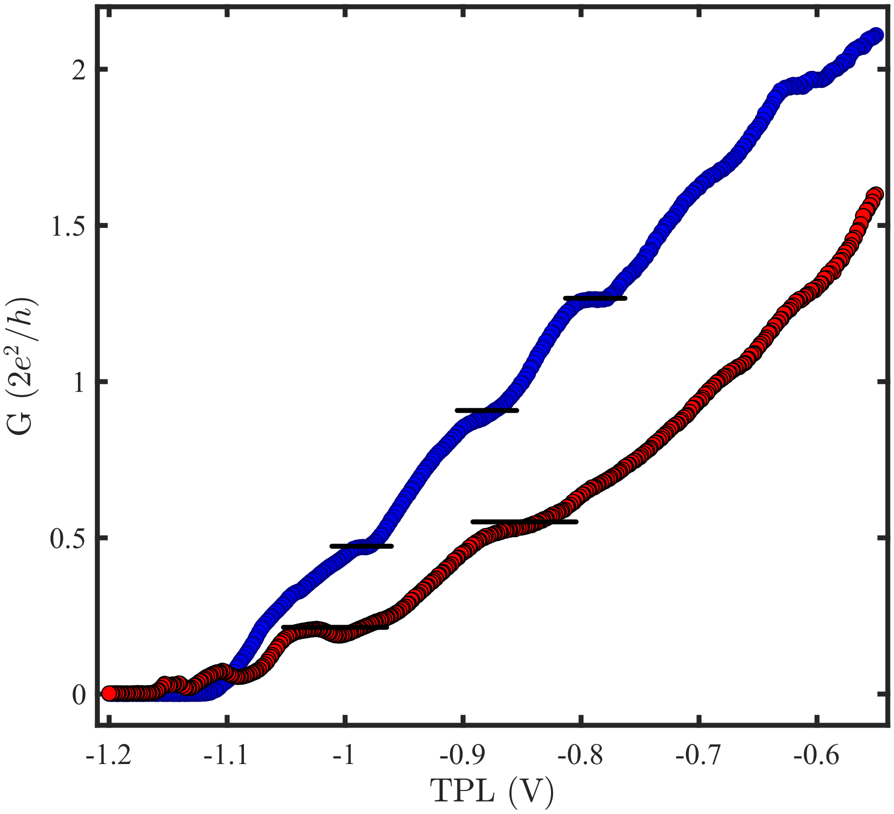

Figure 5.8: Cut of subband mapping at BPL = -1.065 V. The top wire is red, and the bottom wire is blue. Black lines indicate the subband. The conductance values have been corrected for series resistance contributions from the wiring and the 2DEG, as determined from the PO gate sweep. Two resonance peaks are visible below the first subband in the top wire (red).

The conductance values associated with the first subbands are lower than the expected quantized value of $2e^2/h$ for ballistic QWs, indicating the presence of disorder in the system. Additionally, the top wire exhibits local conductance enhancements below the first subband, possibly due to quantum interference and resonant tunneling effects in disordered QWs [110, 111]. A smaller plateau is also observed below the first subband of the bottom QW, reminiscent of the 0.7 structure commonly seen in clean ballistic QWs and QPCs [14, 31]. As TPL approaches zero, the conductances of both wires increase rapidly and monotonically until they reach their corresponding 2DEG conductance. This data is omitted for clarity.

5.4.2 Subband Linearity

Further confirmation of the subband structure can be obtained by examining the effect of a DC bias on the conductance of the QWs. The measurement setup shown in circuit b) of Fig. 5.6 is used to generate a waterfall plot, displaying the conductance of both QWs as a function of applied DC bias and subband occupancy. The resulting data, presented in Fig. 5.9, provides additional insights into the energy spacing and linearity of the subbands.

The bottom wire exhibits a predominantly linear conductance response over the range of applied DC biases, with three distinct conductance plateaus corresponding to the first three subbands. These plateaus are highlighted in Fig. 5.9 a) using purple, blue, and pink circles. No zero-bias anomaly is observed in either QW. However, the top wire exhibits nonlinear characteristics suggestive of fractional conductance states around 1/2 and 3/2 of the first subband, which occur when multiple subbands fall within the bias window [14, 31], as explained in Fig. 2.4. The first and second subbands of the top wire are indicated by purple and blue circles, respectively.

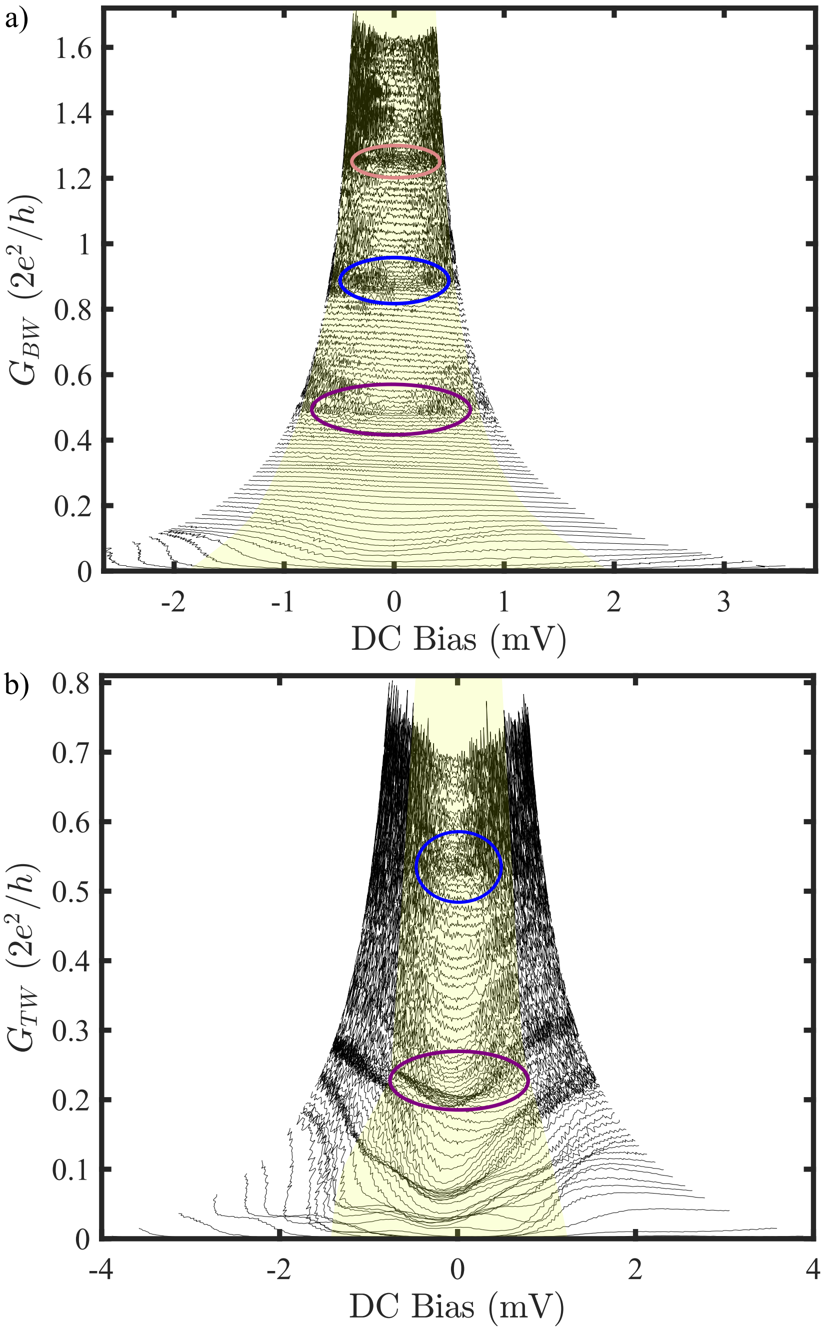

Figure 5.9: Bias spectroscopy measurements of the conductance of B28C1-C at BPL = -1.065 V. a) Bottom wire conductance-bias sweeps at different TPL voltages starting at -0.7 V (top curve) to -1.051 V in increments of 4 mV per curve. b) Top wire conductance-bias sweeps at different TPL voltages starting at -0.78 V (top curve) to -1.2 V in increments of 4 mV per curve. The curves are not offset — conductance decreases when charging the gate negatively. The purple circle indicates the first subband, blue the second, and pink the third. The approximate region of linearity is indicated in yellow.

5.5 Coulomb Drag Measurements

With the QWs characterized, Coulomb drag measurements can take place. The drag characterization is performed using the symmetric drag voltage measurement circuit shown in Fig. 5.10[8]. A virtual ground, symmetrically positioned between two 500 kΩ resistors, is employed to minimize the influence of spurious potentials that may develop between the reservoirs of the drag wire.

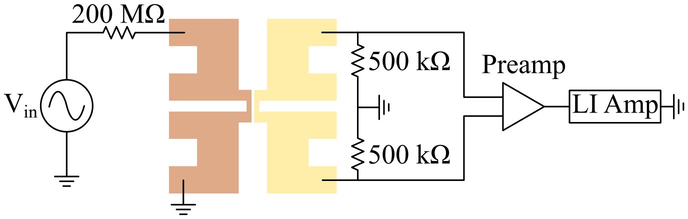

Figure 5.10: Drag measurement circuit. The preamplifier is a SIM910.

The first step in characterizing the drag signal involves measuring it as a function of subband occupancy, using the same plunger PL voltage values as in Fig. 5.8. The resulting drag signal is shown in Fig. 5.11, superimposed on the QWs conductance traces for the corresponding TPL voltages. Peaks in the positive drag signal are observed at the onset of the first (purple) and second (blue) subbands, consistent with the findings of Laroche [76] and Debray *et al.* [36]. These features provide further confirmation of the subband identification. A summary of the parameters used for the Coulomb drag measurements is presented in Appendix G.

5.5.1 Coulomb Drag Tests

Coulomb drag in one-dimensional systems has been the subject of extensive experimental investigation, leading to the establishment of formal criteria for identifying and validating the drag regime under study [36, 39, 42, 44, 112]. Four principal

---

[8] A symmetric drive circuit, shown in Appendix F, was also tested. This circuit also enabled the application of a voltage difference between the drive and drag wires. No significant variation in the measured signal was observed when using this fully symmetrical configuration. Applying a voltage difference between the drag and drive wires also did not produce any unexpected changes in the signal, aside from those consistent with the corresponding variation in gate voltages.

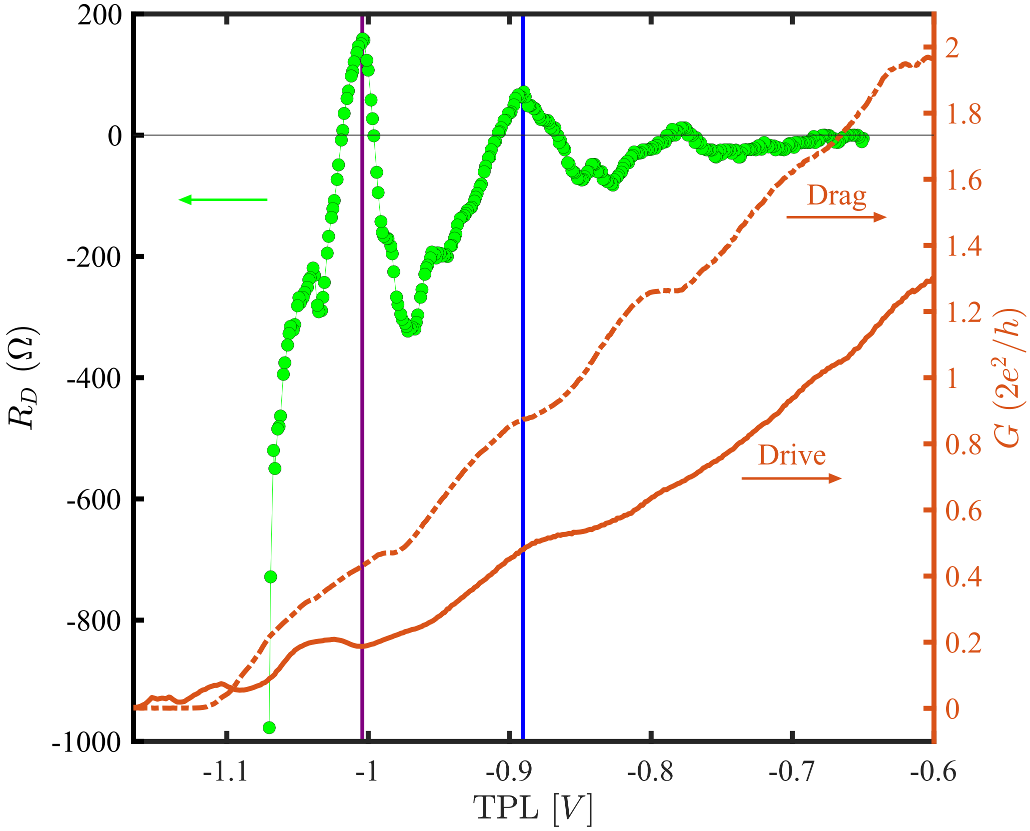

Figure 5.11: Subband alignment confirmation with drag signal for BPL = -1.065 V. Input voltage is $V_{in} = 0.3$ V ($I_{in} = 1.5$ nA). The purple line shows the peak associated with the first subbands, and the blue line shows the peak associated with the second subbands.

consistency checks are commonly employed to characterize the drag signal: verification of the reciprocity relation, linearity with respect to drive current, frequency independence, and confirmation of negligible inter-wire tunneling. The results of these tests for B28C1-C are presented in Figs. 5.12, 5.13, 5.14, and 5.15.

Reciprocity Relation Verification

The verification of reciprocity relations comprises two distinct tests: probe symmetry and Onsager reciprocity. The main results of this thesis are related to these tests and are discussed in greater detail in Chapter 6.

Probe symmetry testing involves reversing both the drive and drag probes simultaneously and verifying whether the drag signal remains invariant. In Fig. 5.12,

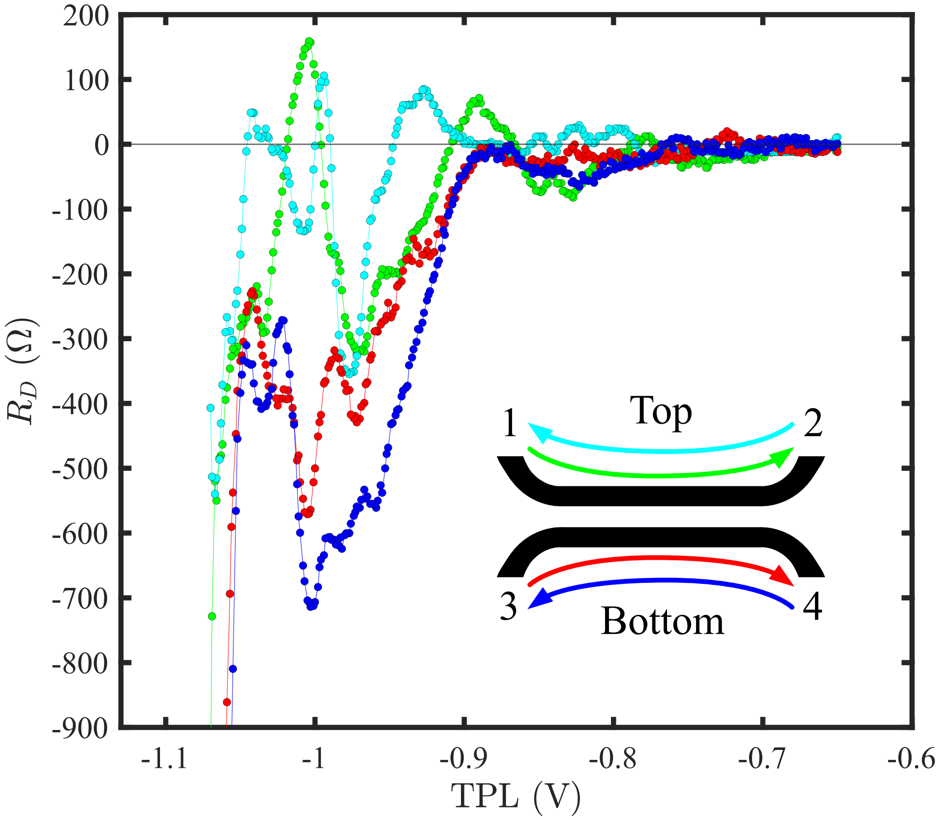

Figure 5.12: Reciprocity tests. Arrows correspond to drive current directions. Green: drive wire current flowing from 1 to 2, drag voltage difference between 3 and 4. Cyan: drive 2 to 1, drag 4 and 3. Red: drive 3 to 4, drag 1 and 2. Blue: drive 4 to 3, drag 2 and 1. The drive current is fixed at 1.5 nA.

this corresponds to comparing the green and cyan traces, as well as the red and blue traces. While the red and blue signals exhibit close agreement, except for a localized deviation between -1 V and -0.9 V, the green and cyan traces show a more pronounced discrepancy. Flipping only the drag-side probes results in a signal of the same magnitude but the opposite sign, as expected. The observed symmetry breaking arises only when the direction of the drive current is reversed.

Onsager reciprocity is tested by interchanging the roles of the drive and drag wires. In Fig. 5.12, this corresponds to comparing the green and red traces, as well as the cyan and blue traces. Both pairs exhibit significant deviations. These deviations are probably due to differences in the potential landscape in each QW.

Symmetric drive circuits were tested to ensure that the observed Onsager reciprocity breaking is not due to circuit asymmetries.

While reciprocity breaking is expected to occur in the charge-fluctuation model of Coulomb drag, recent studies, including the present work, suggest the existence of a more intricate regime. In this regime, nonreciprocal rectification of charge fluctuations and momentum transfer consistent with Luttinger liquid behavior may coexist [45].

Linearity Verification

Establishing the linearity of the Coulomb drag signal is essential for determining the upper limit of the drive current beyond which Joule heating or finite-length effects become significant, as discussed at the end of Sec. 2.3.2. Given the high sensitivity of the drag signal to temperature, it is critical to ensure that the measurement process does not introduce thermal artifacts. A linearity map, such as the one shown in Fig. 5.13, confirms the linear response across the full range of subband occupancies. The inset highlights the linearity when both wires are tuned to the onset of the first subband (top inset) and the second subband (bottom inset). The drag signal in the 1–1 configuration remains linear up to approximately 10 nA (rms), while the 2–2 configuration maintains linearity up to approximately 6 nA (rms).

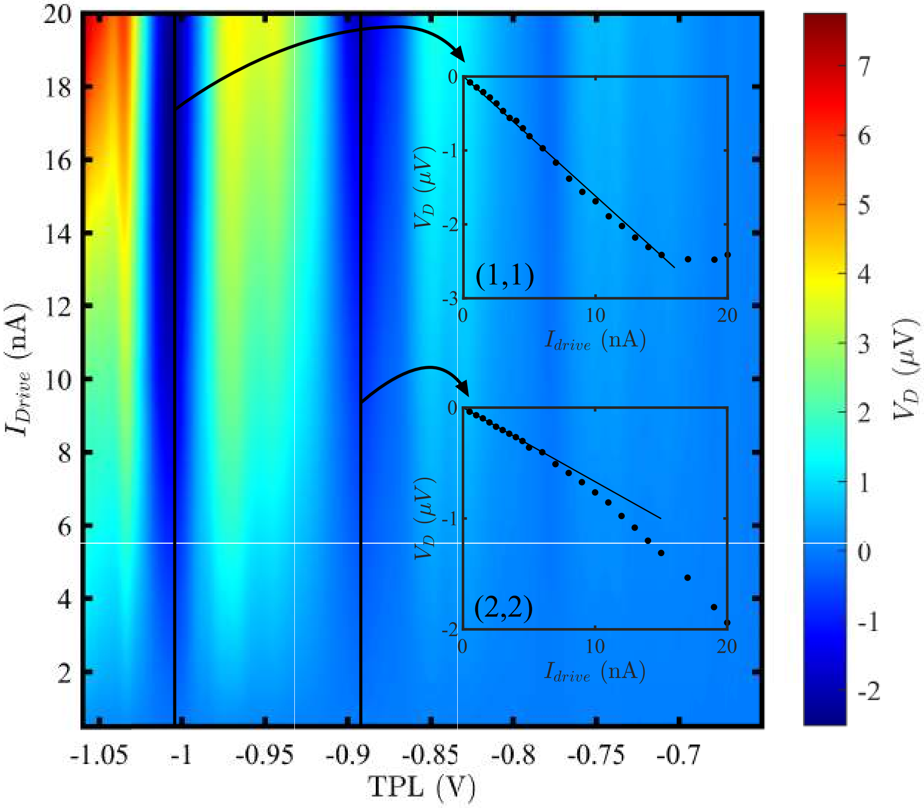

Figure 5.13: Linearity of the green configuration in Fig. 5.12 across all subband occupations. Insets: linearity when both wires are in the first subband (top) and when both wires are in the second subband (bottom). Currents are rms values.

Frequency independence

To ensure that capacitive effects in the device and measurement circuit are negligible, the frequency dependence of the drag signal needs to be verified. As shown in Fig. 5.14, measurements performed at frequencies ranging from 12 Hz to 99 Hz reveal no significant variation, confirming that the chosen measurement frequency is sufficiently low.

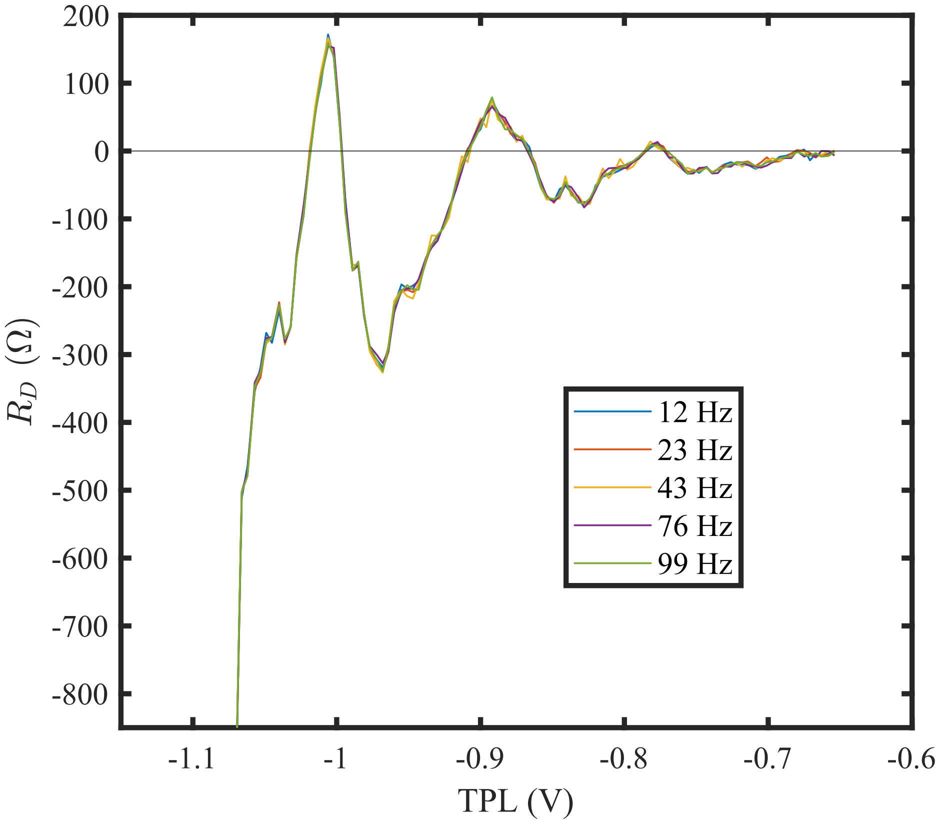

Figure 5.14: Frequency independence of the green configuration in Fig. 5.12. The drive current is 1.5 nA.

Tunneling Contribution Estimation

To rule out parasitic tunneling contributions, the drag voltage is compared to the voltage expected from our criteria of 10 MΩ for the tunneling resistance between the wires. This estimate, shown as the dashed blue line in Fig. 5.15, is based on the known resistance of the QWs and the drive current used. The measured drag voltage (solid blue line) significantly exceeds the estimated tunneling voltage for TPL > -1.05 V, indicating that tunneling is negligible in this regime. This estimate represents an upper bound, as the actual tunneling resistance exceeds 10 MΩ, as demonstrated in Fig. 5.5. Thus, the observed signal can be confidently attributed to Coulomb drag, rather than to spurious contributions from interlayer tunneling.

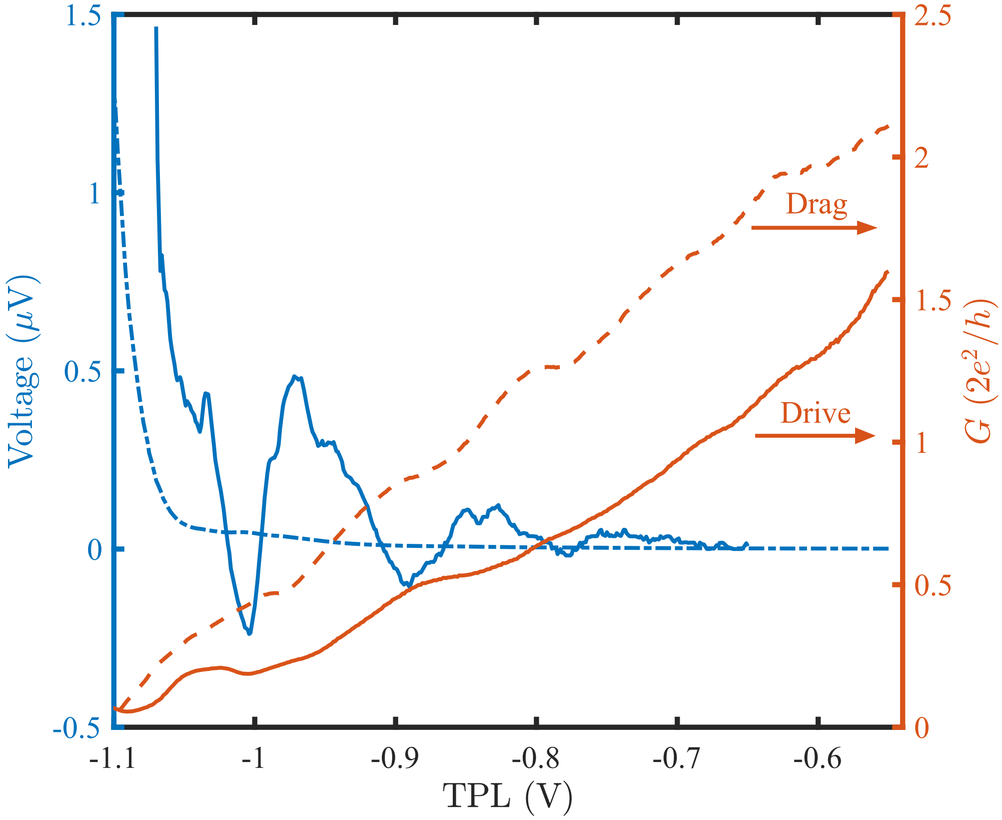

Figure 5.15: Comparison between the measured drag voltage in the green configuration in Fig. 5.12 (solid blue line) and the estimated tunneling-induced voltage (dashed blue line), assuming a 10 MΩ tunneling resistance between the wires. The drive current is 1.5 nA.

5.5.2 Temperature dependence

As discussed in Sec. 2.3, the temperature dependence of the drag signal provides critical insight into the underlying drag mechanism. Different theoretical models predict distinct temperature scalings for the drag resistance, allowing experimental data to be compared against these predictions to identify the operative regime. In particular, momentum-transfer models involving drag between Luttinger liquids predict an upturn in the drag signal at temperatures below a characteristic crossover temperature T^*. In contrast, Fermi liquid models predict a linear dependence, $R_D \sim T$, while models based on rectification of charge fluctuations yield a quadratic dependence, $R_D \sim T^2$ for ballistic QPCs, and an inverse dependence, $R_D \sim 1/T$ for diffusive QWs. The temperature dependence of all subband occupancies at BPL = -1.065 V, for all four possible probe and drive current configurations, is shown in Fig. 5.16.

The temperature mapping in configuration a) of Fig. 5.16 reveals that the drag signal remains positive from base temperature up to 1.2 K in regions where both QWs' first and second subbands are aligned. As the temperature increased, these positive drag peaks broaden while their amplitude diminishes. Continuous temperature sweeps of these two subband occupancy regimes were also performed and are shown in Fig. 5.17 and 5.18. The remaining three probe and current configurations exhibit qualitatively similar behavior: thermal broadening of the drag peaks and a reduction in peak amplitude with increasing temperature.

For both continuous temperature sweeps in the 1-1 and 2-2 subband-aligned regimes (Fig. 5.17 and Fig. 5.18), an upturn in the drag signal was observed as the temperature decreases[9]. In both cases, an exponential and a power-law were fitted to a selected temperature range (highlighted in yellow), chosen based on the quality

---

[9] The presence of an upturn was confirmed in other devices fabricated from wafer VA0486 by measuring the drag signal up to 8.4 K. This measurement was not performed on the present device, as thermal cycling to such temperatures was found to slightly alter the device state, thereby compromising reproducibility.

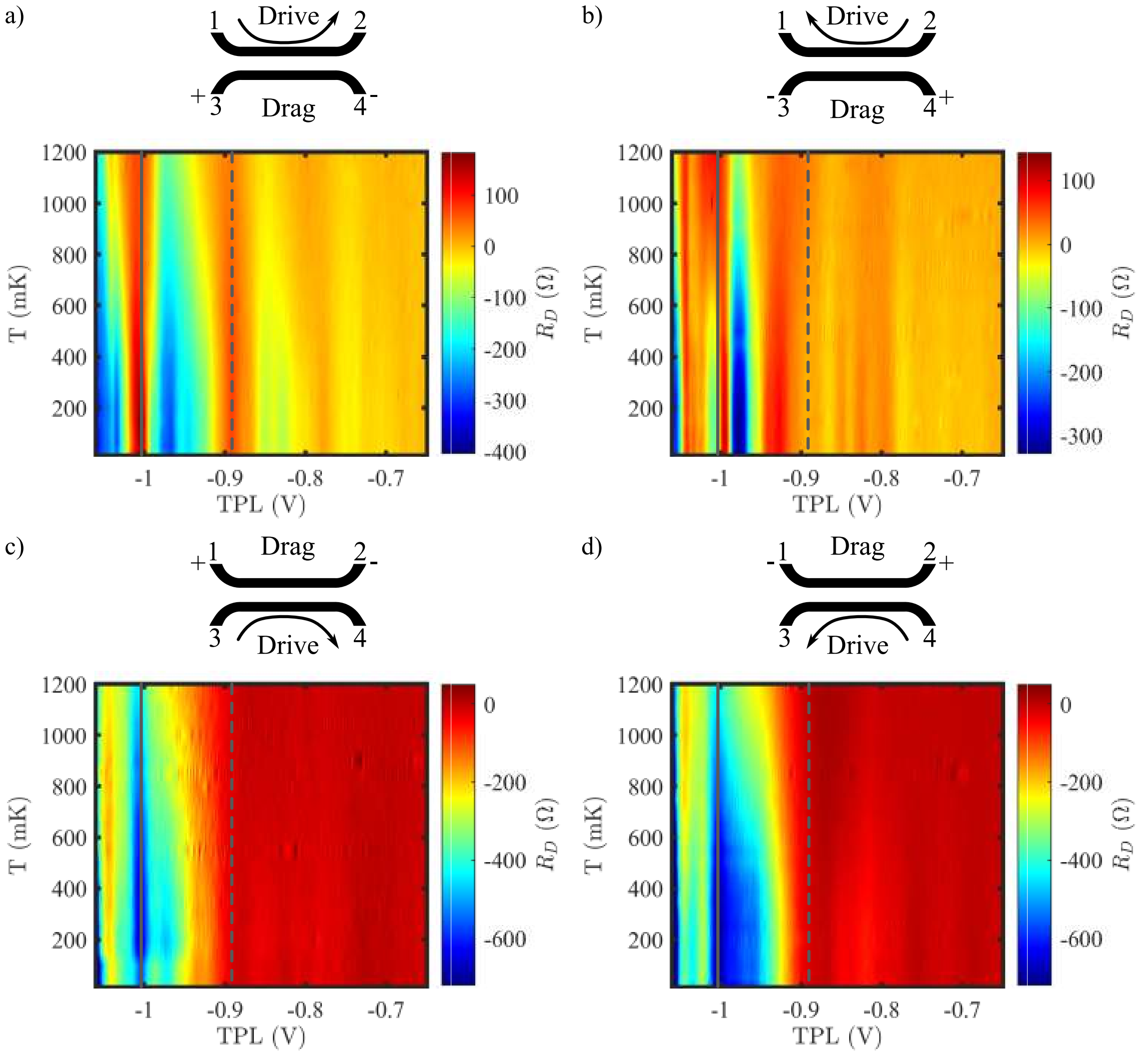

Figure 5.16: Temperature dependence mapping of the drag signal over all subband occupancies at BPL = -1.065 V for B28C1-C measured with V_{in} = 0.3 V (1.5 nA). a) Drive wire current flowing from 1 to 2, drag voltage difference between 3 and 4. b) Drive 2 to 1, drag 4 and 3. c) Drive 3 to 4, drag 1 and 2. d) Drive 4 to 3, drag 2 and 1. The solid grey lines indicate where the first subbands of both QWs are aligned, while the dashed grey lines correspond to the alignment of the second subbands.

of the fit. The exponential fit was performed to identify possible signatures of the strong-coupling regime, while the power-law fit was used to probe contributions from backscattering, charge fluctuations, spin-incoherent behavior, or forward-scattering mechanisms.

The exponential and power-law fits were done over the same temperature ranges:

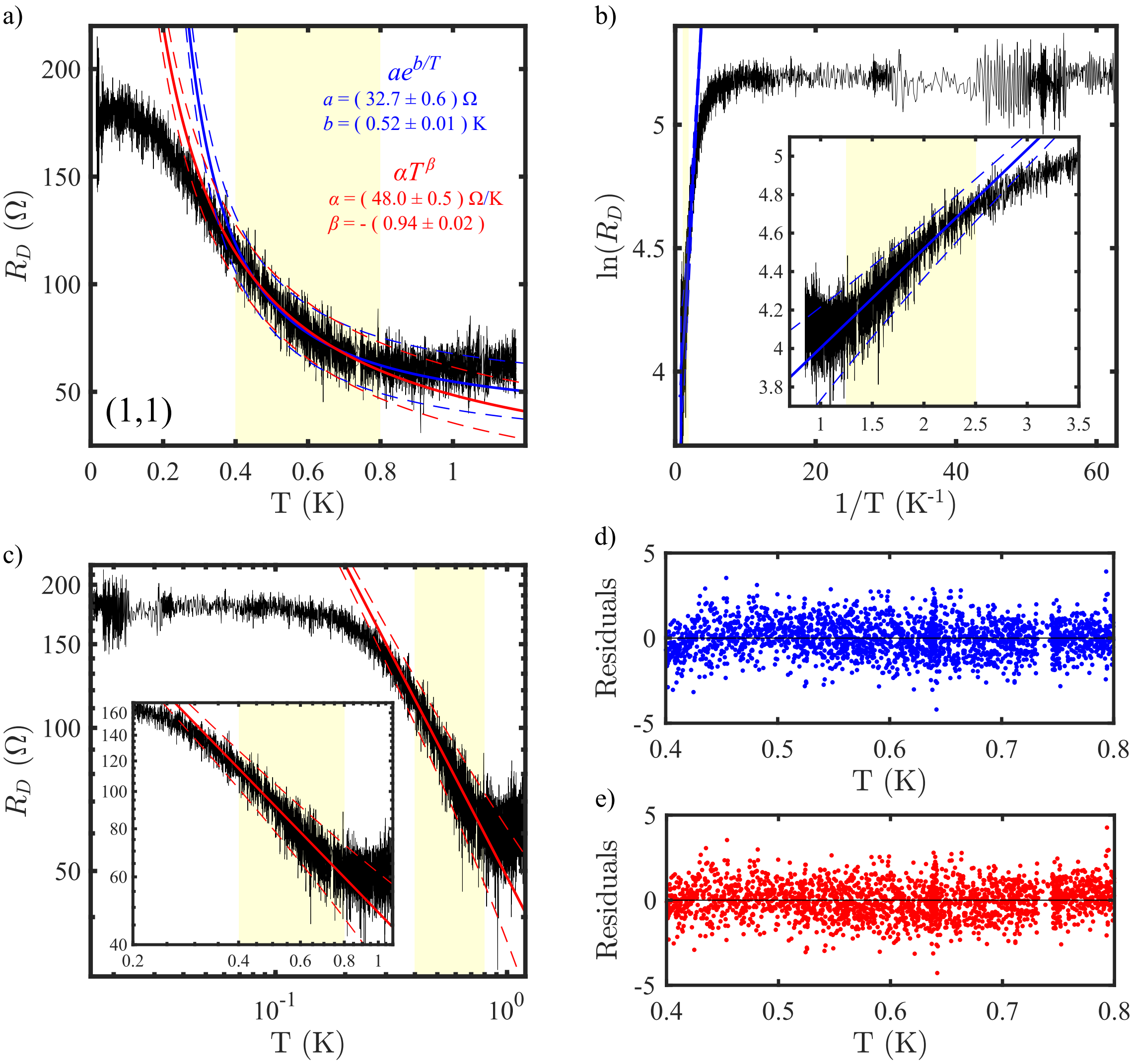

Figure 5.17: Continuous temperature dependence of the drag signal with both wires in their first subband for configuration a) in Fig. 5.16. a) Coulomb drag signal: measured values are shown in black, the exponential fit in blue, and the power-law fit in red. The fits are performed over the data within the yellow-shaded region. Dashed lines indicate the 95% prediction bounds for the respective fits. b) Coulomb drag signal plotted on an Arrhenius scale. c) Coulomb drag signal plotted on a log-log scale. Insets provide a zoomed-in view of the fit region. d) Standardized residuals for the exponential fit. e) Standardized residuals for the power-law fit. BPL = -1.065 V, TPL = -1.005 V, and V_{in} = 0.3 V. Uncertainties on the fitting parameters are statistical and are determined from the fit.

from 0.4 K to 0.8 K for the 1–1 data, and from 0.7 K to 1.3 K for the 2–2 data. To reveal any exponential behavior, the drag resistance is plotted in Arrhenius form (Figs. 5.17 b and 5.18 b), where an exponential dependence manifests as a linear trend. Similarly, the drag resistance is also plotted in log–log form (Figs. 5.17 c and

5.18 c), where a power-law dependence appears as a linear trend.

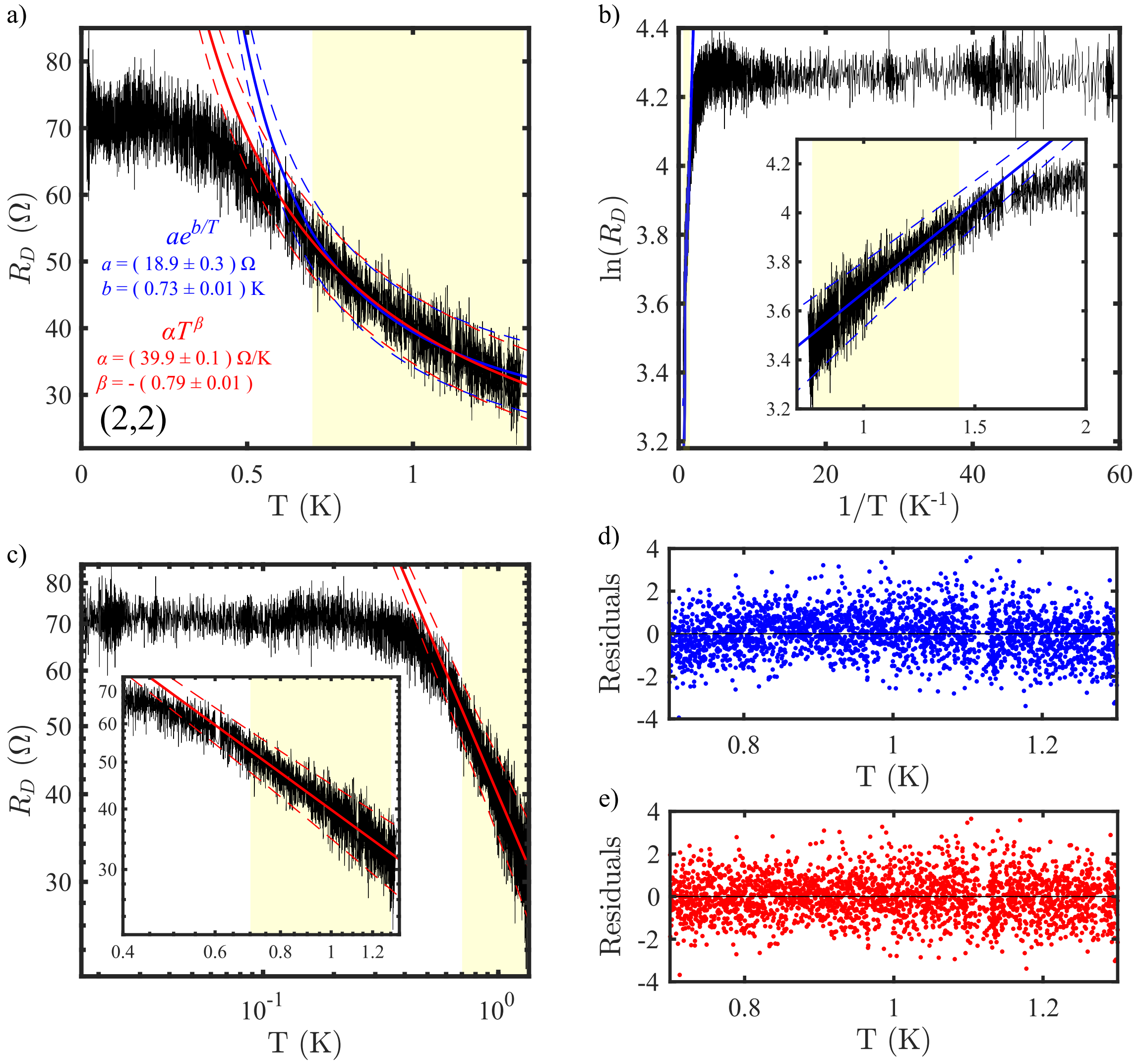

Figure 5.18: Continuous temperature dependence of the drag signal with both wires in their second subband for configuration a) in Fig. 5.16. a) Coulomb drag signal. b) Coulomb drag signal plotted on an Arrhenius scale. c) Coulomb drag signal plotted on a log-log scale. d) Standardized residuals for the exponential fit. e) Standardized residuals for the power-law fit. Same parameters as in Fig. 5.17 except TPL = -0.890 V. Uncertainties on the fitting parameters are statistical and are determined from the fit.

An exponential increase in the drag signal with decreasing temperature is expected within the reciprocal momentum-transfer framework for Coulomb drag between matched-density Luttinger liquids, particularly in the low-temperature regime with strong coupling $T < T^{*}$. The b parameter obtained from the exponential fit over the selected temperature range provides an experimental estimate for T^{*}. For the 1–1 case, we find $T^* \sim b = (0.52 \pm 0.01)$ K, and for the 2-2 case, $T^* \sim b = (0.73 \pm 0.01)$ K. The exponential behavior is expected to hold as long as the charge carriers remain in thermal equilibrium with the cryostat[10] and the thermal length satisfies $L_T < L$. As the temperature approaches T^*, deviations from exponential scaling are anticipated, with increasing contributions from power-law behavior associated with forward-scattering processes, as previously observed in Ref. [76] or contributions from spin-incoherent processes (Eq. 2.23) and backscattering under weaker interaction (Eq. 2.19).

A power-law increase in the drag signal with decreasing temperature is expected within three models of Coulomb drag: backscattering for $T > T^*$, forward scattering for $T > T_F$, and charge fluctuations between diffusive QWs. The β parameter obtained from the power-law fit over the selected temperature range provides a clue for discarding some of these models. For the 1–1 case, we find $\beta = -(0.94 \pm 0.02)$, and for the 2–2 case, $\beta = -(0.79 \pm 0.01)$. The forward-scattering model predicts a power-law increase in drag with decreasing temperature, with an exponent of $-3/2$ for $T > T_F$. Both experimentally determined exponents differ from this prediction, thereby ruling out the forward-scattering model for this temperature range. The 1–1 exponent of $-(0.94 \pm 0.02)$ agrees with charge-fluctuation models in diffusive QWs and with a backscattering model under weak interaction ($T > T^*$). The 2–2 exponent of (0.79 ± 0.01) could only be explained by a backscattering model at weak interaction, but the observed nonreciprocity of the signal suggests otherwise.

In all three models predicting power-law behavior, this behavior holds as long as the charge carriers remain in thermal equilibrium with the cryostat and as long as the temperature does not break coherence in the QWs and reduce the screening length[11] to a point where no Coulomb drag can occur. This imposes both lower and upper bounds on the expected behavior, making it necessary to perform fits over a selected temperature range when searching for either exponential or power-law

---

[10] Assuming negligible self-heating of the QWs.

[11] The screening length is the distance over which electric fields are screened by mobile charges.

scaling.

The characterization of the drag signal presented in this chapter does not allow for the identification of a single mechanism responsible for the observed Coulomb drag. Instead, the data suggest a combined-process scenario in which multiple regimes contribute to the signal. From the fits shown in Figs. 5.17 b) and 5.18 b), both exponential and power-law models appear to adequately describe the drag resistance over the selected temperature range. However, the residuals of the power-law fits (Figs. 5.17 e and 5.18 e) are slightly more randomly distributed around zero than those of the exponential fits (Figs. 5.17 d and 5.18 d). This difference is more pronounced in the 2–2 data, where the moving average of the residuals from the exponential fit curves downward in an inverse-parabolic shape centered around 1 K, indicating a less-than-ideal fit. The reduced exponential character of the 2–2 data may suggest that increased screening, *i.e.* a decreased screening length, in higher subbands leads to a diminished contribution from the strong coupling Luttinger liquid mechanism, which is associated with exponential temperature dependence, to the overall drag signal.

In our system, when the drive wire operates in the first or second subband, the conditions $L_v \leq L = 5\mu\text{m}$ and $L_T \leq L$ are satisfied for temperatures $T \geq$ 300 mK. This ensures that $L_T, L_V, \lambda_F < L$, placing the system within the regime where Luttinger liquid behavior is expected to dominate. However, the observed breakdown of reciprocity suggests that additional mechanisms may also contribute significantly to the drag response. As will be discussed in Chapter 6, the drag signal can be tuned to satisfy reciprocity relations through the application of a DC current bias.

Reciprocal and nonreciprocal Components Extraction

Recently introduced by Laroche's group [46], the extraction of the reciprocal and nonreciprocal components of the drag resistance enables independent analysis of the nonlinear (nonreciprocal) contribution — thought to arise from rectification of quantum shot noise — and the linear (reciprocal) contribution, which may originate from near-equilibrium thermal noise rectification due to electron-hole asymmetry or conventional momentum-transfer drag between Luttinger liquids [44]. This approach is primarily a data-analysis method rather than a measurement procedure, provided that each drag measurement is performed in all four possible drive-current configurations, as illustrated in Fig. 5.16.

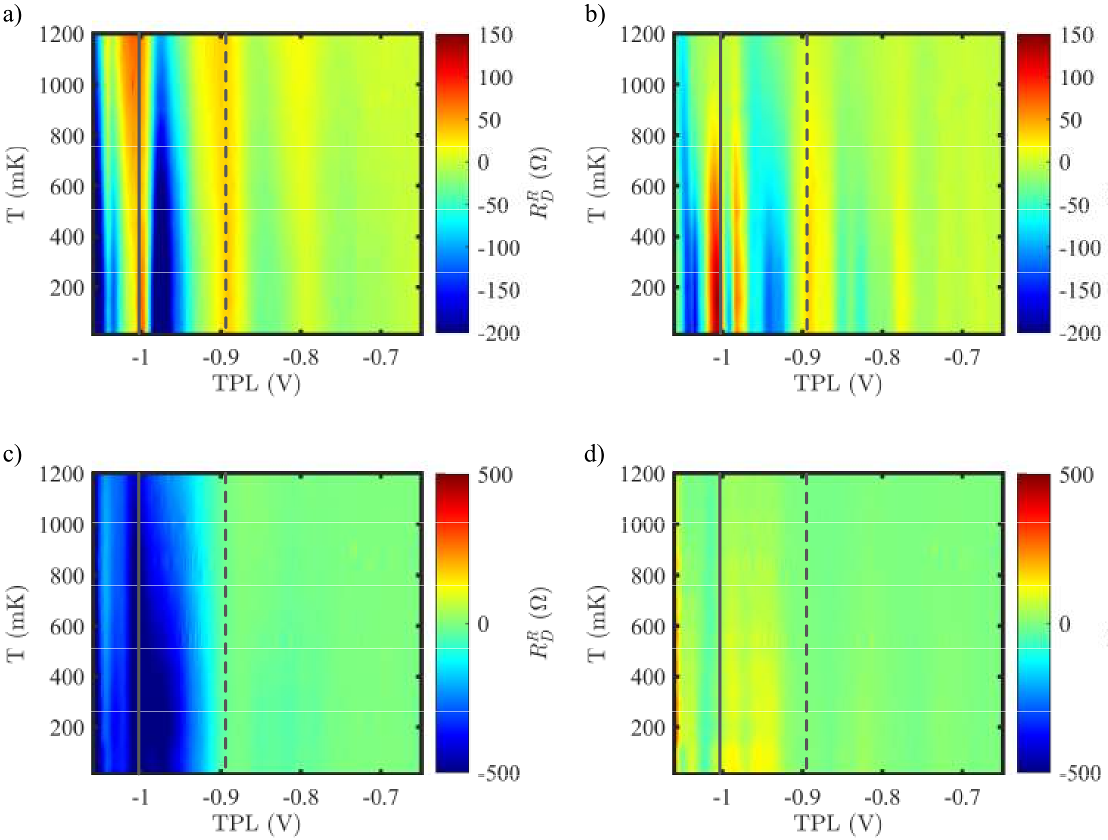

Figure 5.19: Temperature-dependent mapping of reciprocal and nonreciprocal components of Coulomb drag resistance across all subband occupancies. a) and b): Reciprocal and nonreciprocal components, respectively, with the drive current applied to the top QW. c) and d): Reciprocal and nonreciprocal components, respectively, with the drive current applied to the bottom QW. Solid grey lines mark the alignment of the first subbands of both QWs, while dashed grey lines indicate the alignment of the second subbands.

By taking the sum and the difference between probe symmetry signals — for example, configurations a) and b) in Fig. 5.16 — we can extract these components.

The reciprocal component is given by

$$R_D^R = \frac{R_D^{a)} + R_D^{b)}}{2}, \tag{5.2}$$

and the nonreciprocal component is given by

$$R_D^{NR} = \frac{R_D^{a)} - R_D^{b)}}{2}, \tag{5.3}$$

where $R_D^{a)}$ and $R_D^{b)}$ are the drag resistance value corresponding to Fig. 5.16 a) and Fig. 5.16 b), respectively.

Fig. 5.19 shows the results of extracting these components for the temperature-dependent data of Fig. 5.16. Across all subband occupancies, when the drive current is applied to the top QW, R_D^{NR} generally exhibits stronger temperature dependence than R_D^R. Conversely, when the drive current is applied to the bottom QW, both R_D^{NR} and R_D^R show weaker temperature dependence, except near the 1–1 configuration, where R_D^R becomes significantly temperature dependent.

Cuts at 1–1 and 2–2 of the data in Fig. 5.19 are shown in Fig. 5.20. When the drive current is applied to the top wire (Figs. 5.20 a and b), R_D^{NR} at both 1–1 and 2–2 is significantly more temperature dependent than R_D^R. Furthermore, R_D^{NR} increases as temperature decreases, more prominently for the 1–1 data. In contrast, R_D^R for the 1–1 data decreases with temperature until it reaches a nearly constant value around 0.5 K down to 15 mK. R_D^R for the 2–2 data shows a similar trend to R_D^{NR}. When the drive current is applied to the bottom wire, only R_D^R for the 1–1 case exhibits noticeable temperature dependence. Switching the drive current between the top and bottom wires, therefore, changes both the dominant component of the drag signal and the temperature dependence of these components.

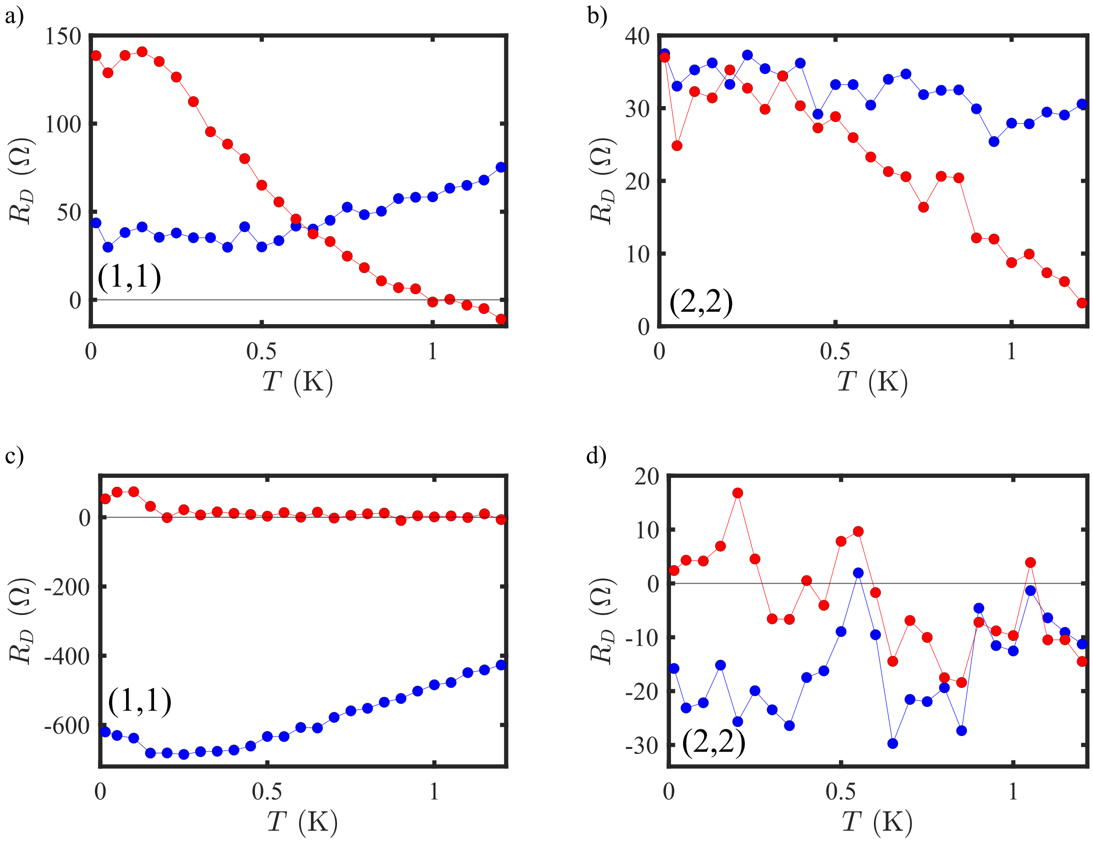

Figure 5.20: Reciprocal (blue) and nonreciprocal (red) components of Coulomb drag resistance at subband alignments 1–1 (a, c) and 2–2 (b, d) as a function of temperature. a) and b): Drive current applied to the top QW. c) and d): Drive current applied to the bottom QW.

5.6 Conclusion

This concludes the characterization of the Coulomb drag devices. Standard transport quantities such as density and mobility were evaluated, device-specific verifications were performed, and the Coulomb drag signal was characterized. Although the observed drag signal cannot be explained by a single model — due to its temperature dependence and the breakdown of reciprocity relations — both exponential and power-law fits adequately describe the data over the selected range. The parameters obtained from the fits on the 1–1 data are consistent with Coulomb drag between matched-density strongly coupled Luttinger liquids, charge-fluctuation models in diffusive quantum wires, and a backscattering model under weak interaction. In the 2–2 case, a backscattering model with weak interaction appears to dominate the temperature dependence, but the observed nonreciprocity of the signals, in both the 1-1 and 2-2 cases, indicates that additional mechanisms must also play a significant role. A more definitive conclusion regarding the dominant mechanism could, in principle, be reached if the reciprocity of the drag signal were improved. This was serendipitously achieved through DC bias spectroscopy measurements of Coulomb drag, as described in Chapter 6. Nevertheless, as will be shown, the contributing regimes remain challenging to disentangle.

6

Current Bias Spectroscopy of the Coulomb Drag Resistance

Bias spectroscopy measurements of QW conductance have provided profound insights into the physics of charge carriers in low-dimensional systems (see, for example, Refs. [11, 53, 54]). In this chapter, the first bias spectroscopy measurements of the Coulomb drag resistance between two QWs are presented. We begin by describing the measurement scheme and we then present the experimental results. The Coulomb drag test results are then analyzed under a configuration of DC biases that greatly improves the reciprocity relations. This is followed by a series of tests confirming that the system of QW operates within the linear regime of conductance and that DC tunneling is also negligible. The temperature dependence of this enhanced reciprocity drag regime is then studied in detail.

6.1 Bias Spectroscopy Measurement Scheme

Bias spectroscopy measurements of the Coulomb drag resistance were performed using the circuit shown in Fig. 6.1 wherein a small AC signal was superimposed onto a DC component with a summing amplifier[1]. The combined signal was then fed into the standard drag circuit depicted in Fig. 5.10. A 200 MΩ resistor was set in series with the drive wire to effectively make the input side of the drag circuit a voltage-controlled current source. Consequently, variations in the drive wire resistance have a negligible impact on the drive current. Specifically, an increase of 10 MΩ in the drive wire resistance results in less than a 5% reduction in drive current[2]. All DC voltage sources for the gates and the drive signal were SIM928 modules. The AC signal was a 54.32 Hz frequency sine wave generated by an SR830 lock-in amplifier, which also served to measure the drag voltages after preamplification by a SIM910. Unless otherwise specified, the AC input voltage was set to 0.3 V, yielding an AC drive current of approximately 1.5 nA.

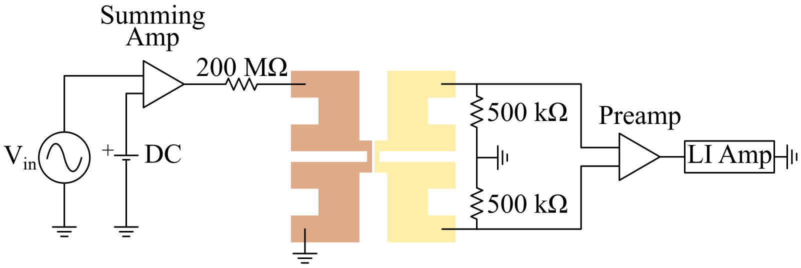

Figure 6.1: Coulomb drag bias spectroscopy measurement circuit.

The results of the bias spectroscopy measurements of the Coulomb drag resistance for the four contact configurations are shown in Fig. 6.2. Dashed lines indicate the DC current values at which the reciprocity relations are most closely satisfied (see Fig. 6.4 for the corresponding data along those lines). Each contact configuration exhibited a distinct response to DC biasing; however, a closer correspondence was observed between probe-symmetry pairs (left-right), particularly when one of

---

[1] The same SIM900 preamplifier used in other circuits was employed here.

[2] Drive wire resistances in the order of MΩ and above are not considered here, as they correspond to conductance values well below the first quantized plateau.

the mappings is vertically reflected. Biasing the drive wire appeared to compensate for the reciprocity-breaking voltage or current contributions, possibly arising from nonlinear rectification of charge fluctuations. The optimal DC bias values for improved reciprocity were found to be: -10 nA for panel a), +10 nA for panel b), +21.94 nA for panel c), and -21.94 nA for panel d).

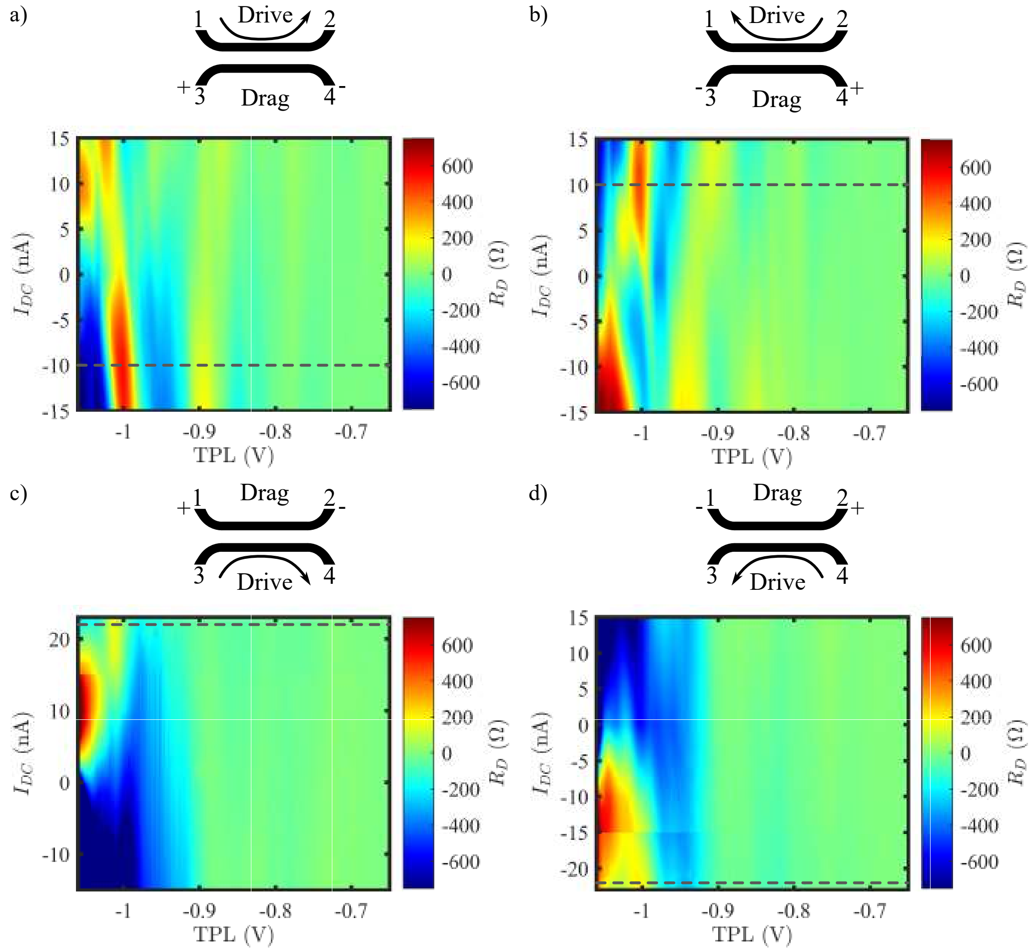

Figure 6.2: Bias spectroscopy measurements of the Coulomb drag in the four possible configurations of contacts. a) AC drive wire current flowing from 1 to 2, drag voltage difference between 3 and 4. b) Drive 2 to 1, drag 4 and 3. c) Drive 3 to 4, drag 1 and 2. d) Drive 4 to 3, drag 2 and 1. Grey dashed lines indicate the DC current values at which the reciprocity relations are most closely satisfied.

The effect of the bias on both drag regimes — namely reciprocal (R_D^R) and nonreciprocal (R_D^{NR}) — can be studied by extracting them in the same manner as in Fig. 5.19. The results are shown in Fig. 6.3. Whether the drive current is applied to the top QW (Figs. 6.3 a and b) or the bottom QW (Figs. 6.3 c and d), the R_D^R component is symmetric about zero bias, whereas R_D^{NR} is not. The nonreciprocal components appear to be antisymmetric, with a more pronounced anti-symmetry in Fig. 6.3 d) than in Fig. 6.3 b). In Fig. 6.3 b), R_D^{NR} appears slightly smaller for positive bias current than for negative bias current.

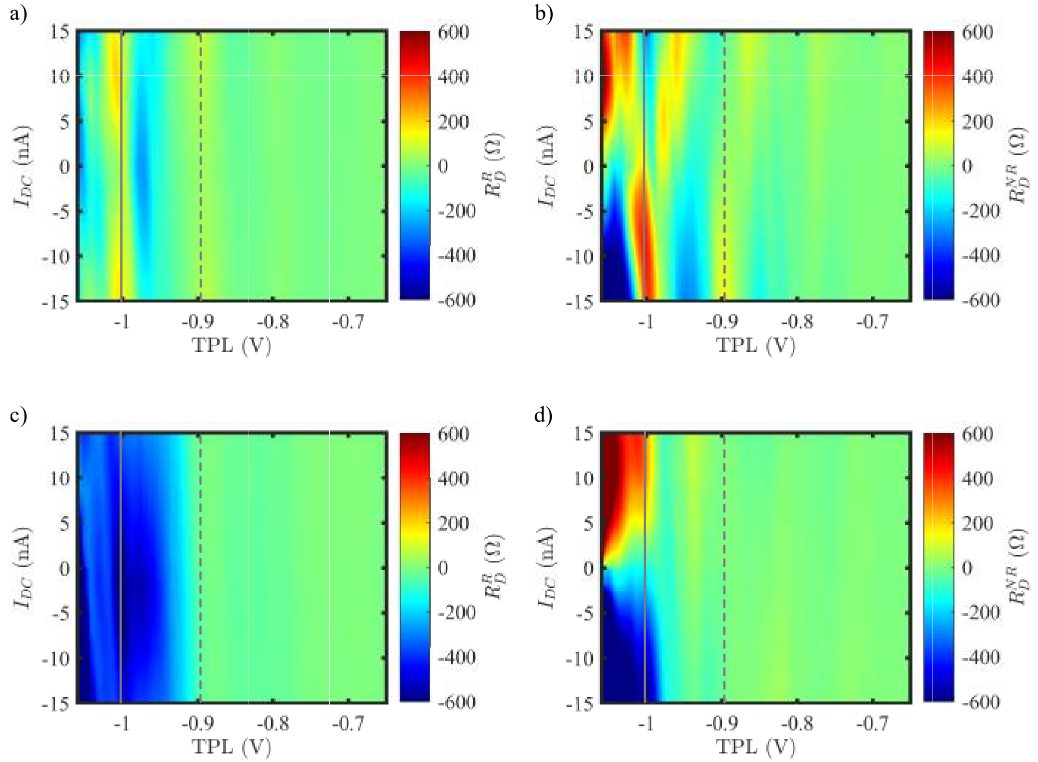

Figure 6.3: DC current bias-dependent mapping of reciprocal and nonreciprocal components of Coulomb drag resistance across all subband occupancies. a) and b): Reciprocal and nonreciprocal components, respectively, with the drive current applied to the top QW. c) and d): Reciprocal and nonreciprocal components, respectively, with the drive current applied to the bottom QW. Solid grey lines mark the alignment of the first subbands of both QWs, while dashed grey lines indicate the alignment of the second subbands.

The observation of a DC bias that greatly improves reciprocity, as shown in Fig. 6.2, lends support to the hypothesis that DC biasing mitigates possible nonlinear rectification of fluctuations that would otherwise significantly influence the signal. Nevertheless, the precise mechanism by which drive wire biasing enhances reciprocity remains unclear at this time and warrants further theoretical investigation.

6.2 Drag Consistency Tests

To confirm the newly observed reciprocity improved drag signal indeed corresponds to a Coulomb drag effect, the four drag tests were performed using the same methodology as in the initial characterization of the unbiased drag signal. The results of these tests are presented in Figs. 6.4, 6.5, 6.6 and 6.7.

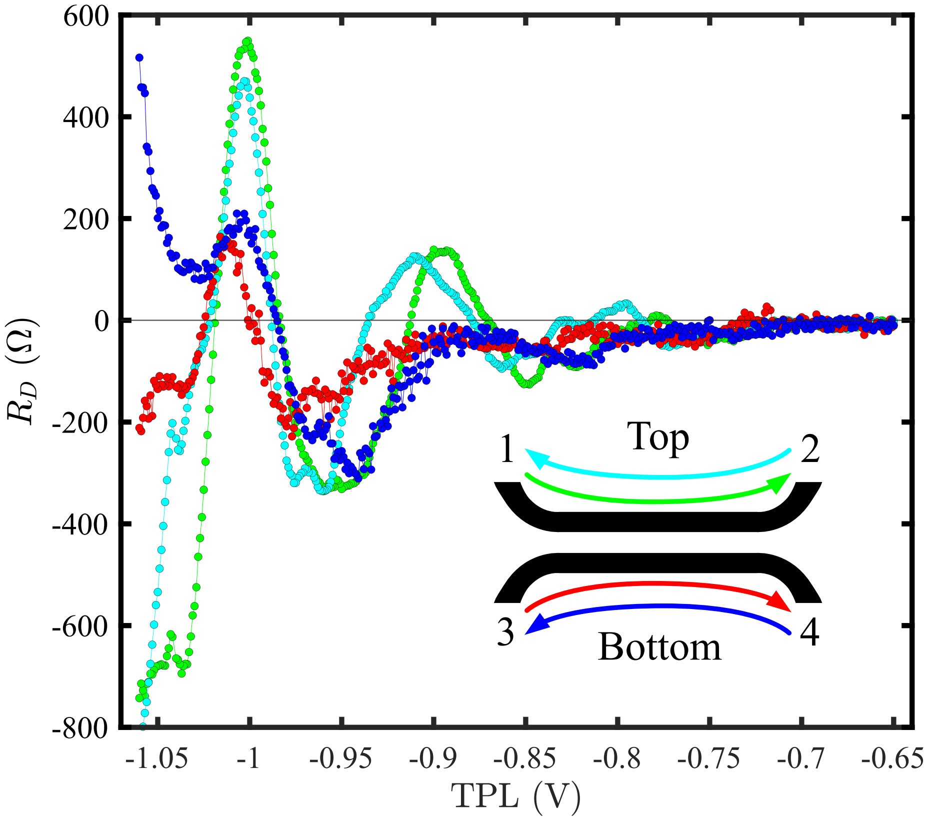

Figure 6.4: DC biased drag reciprocity verification. Arrows correspond to drive current directions. Green: drive wire current flowing from 1 to 2, drag voltage difference between 3 and 4 (-10 nA bias). Cyan: drive 2 to 1, drag 4 and 3 (+10 nA bias). Red: drive 3 to 4, drag 1 and 2 (+21.94 nA bias). Blue: drive 4 to 3, drag 2 and 1 (-21.94 nA bias).

Fig. 6.4 shows the measured drag signals for the four contact configurations, each biased with the optimal DC bias satisfying the reciprocity relations. Probe symmetry is nearly respected, except in the voltage range -0.97 V $<$ TPL $<$ -0.9 V where deviations were observed in both signal pairs (green with cyan and red with blue). We note that a more pronounced discrepancy between the red and blue signals emerged below -1.05 V; however, this region may include contributions beyond Coulomb drag. As shown in Fig. 6.7, AC tunneling becomes significant below this TPL voltage, potentially influencing the drag signal. Additionnally, the possible formation of a Wigner crystal in low-density QWs may begin to affect the signal for TPL below -1.05 V [55]. Onsager reciprocity was more closely satisfied when the drive wire was appropriately DC biased, supporting the hypothesis that nonlinear rectification effects can be mitigated through DC bias tuning. Notably, the amplitude of the signal was smaller when the bottom wire was used as the drive wire. This could be due in part to the unmatched density of the two QWs.

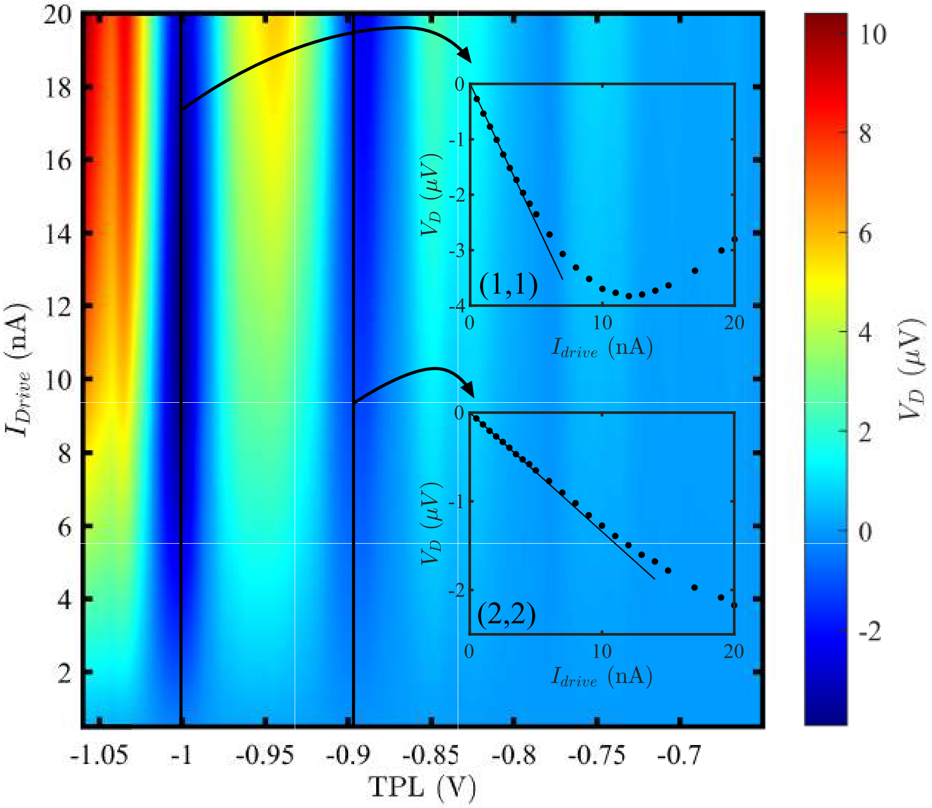

Figure 6.5: DC biased linearity of the green configuration in Fig. 6.4 across all subband occupations. Insets: linearity when both wires are in the first subband (top) and when both wires are in the second subband (bottom). Currents are rms values.

The linearity of the drag signal was investigated across all four contact configurations using their respective optimal DC bias values. For conciseness, only the results for the green configuration are presented here in Fig. 6.5. The top inset demonstrates that the drag response remained linear up to an AC drive current of ∼5 nA at the onset of the first subband. Similarly, the bottom inset shows that linearity was preserved up to roughly 7 nA at the onset of the second subband. These observations confirm that the 1.5 nA AC signal used is sufficiently small to exclude contributions from self-heating and that finite-size effects are negligible.

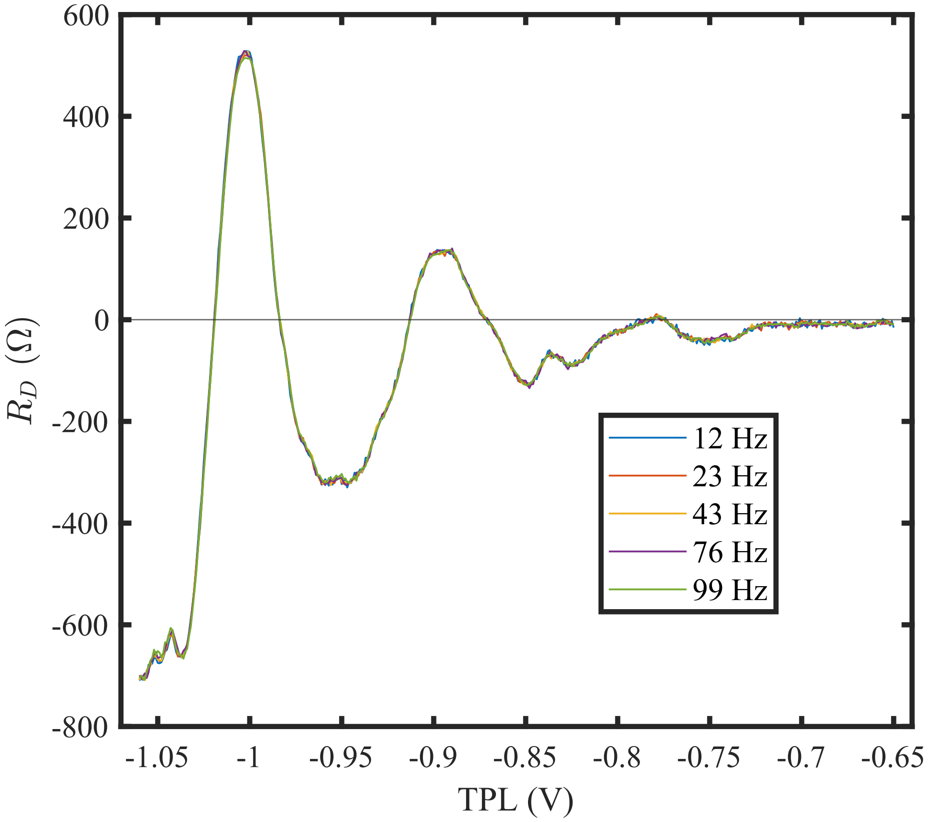

Figure 6.6: Frequency independence of the green configuration in Fig. 6.4. The drive current is 1.5 nA.

As shown in Fig. 6.6, the drag signal remained entirely independent of the drive signal frequency within the range of 12 Hz to 99 Hz, confirming that the measurement circuit does not exhibit significant stray capacitance effects within this range. Finally, Fig. 6.7 shows that the measured drag voltage (solid blue line) significantly exceeds the estimated tunneling voltage for TPL > -1.05 V, indicating that tunneling is negligible in this regime.

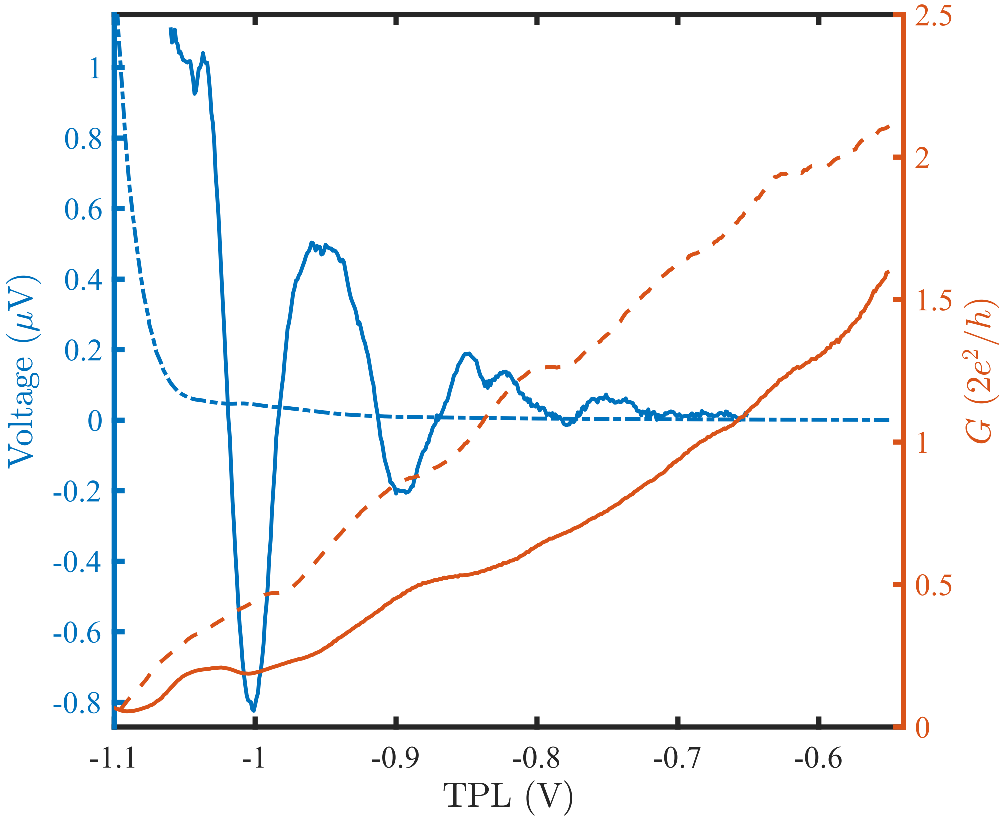

Figure 6.7: Comparison between the measured drag voltage in the green configuration in Fig. 6.4 (solid blue line) and the estimated tunneling-induced voltage (dashed blue line), assuming a 10 MΩ tunneling resistance between the wires. The drive current is 1.5 nA.

6.3 Quantum Wires Verifications

In bias spectroscopy measurements of QW conductance, the DC bias is applied as a voltage, consistent with the nature of conductance measurements, where the voltage is fixed and the current is measured. In contrast, DC bias spectroscopy of Coulomb drag resistance requires a current bias, as resistance measurements involve fixing the current and measuring the resulting voltage. Consequently, it is essential to verify that the DC voltage drop across the QWs, induced by the applied DC current bias in Coulomb drag resistance measurements, remains within the valid operational range of the wires. Specifically, the subband structure, subband linearity, and tunneling all need to be verified at the specific DC current bias used.

When DC bias is applied to the drive wire, its subband structure is expected to shift, as illustrated in Fig. 6.8. As shown in the figure, the DC bias values used to improve reciprocity — indicated by colored points corresponding to each contact configuration — did not significantly alter the positions of the subbands. Moreover, these DC biases remained within the linear transport regime of both QWs at the subband onsets. However, below the first subband, the applied DC current biases pushed the conduction regime of the QW outside the observed linear region, indicating the presence of a more complex transport regime.

To further confirm the linearity of the drive wires at the optimal biases in the first and second subbands, the DC voltages across each wire as a function of the DC current are plotted in Fig. 6.9. These voltage differences are shown for TPL voltages corresponding to the first (purple) and second (blue) subbands. The gray lines indicate the DC bias values used to optimize reciprocity in each configuration. All of these bias values fall within the linear regions of the respective V–I curves. A slight nonlinearity is observed in the V–I curve of the first subband of the top wire Fig. 6.9 b). This nonlinearity is symmetric about zero bias and results in a modest reduction of the effective DC voltage across the wire compared to the ideal linear case.

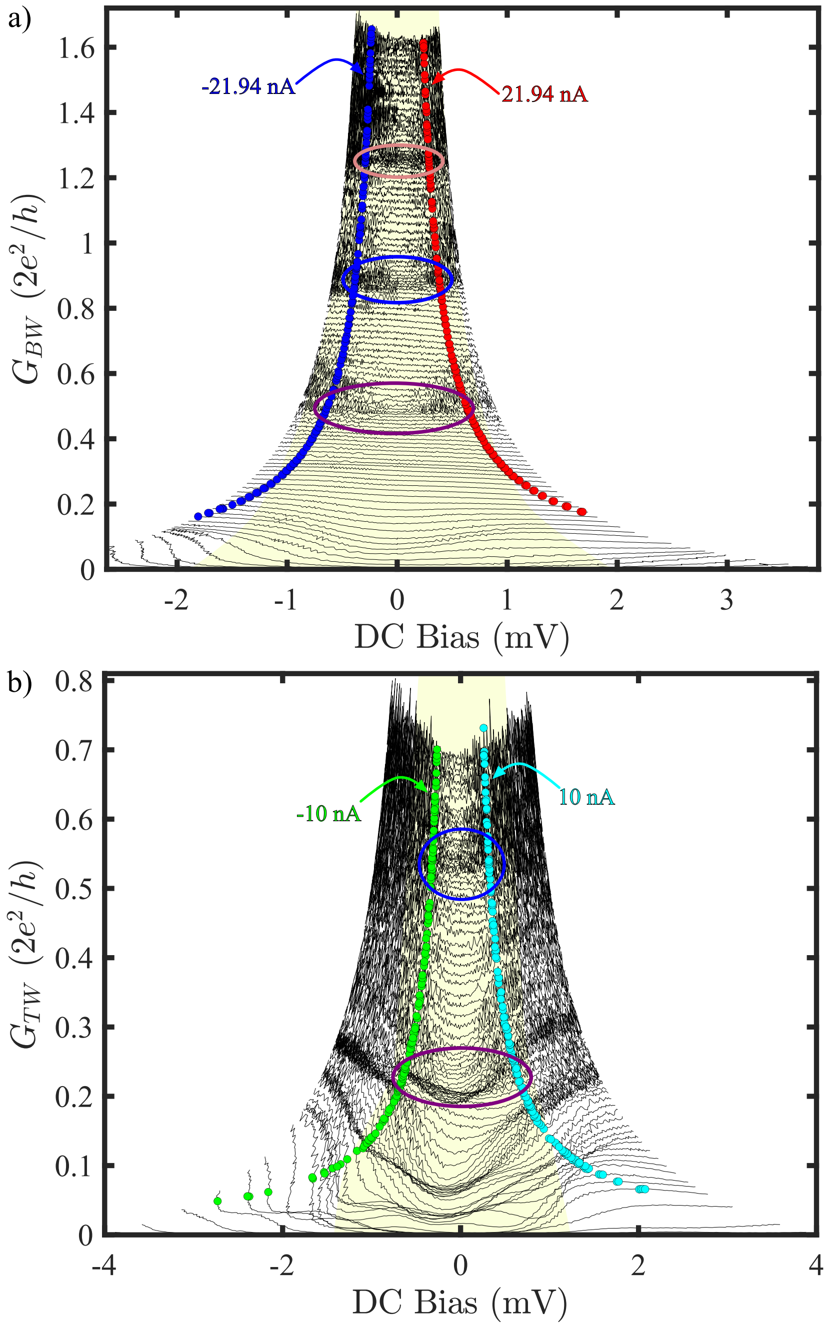

Figure 6.8: Bias spectroscopy measurements of the QWs conductance. a) Conductance-bias sweeps of the bottom wire at various TPL voltages. The DC bias values used to optimize reciprocity are indicated as colored points corresponding to the red and blue contact configurations. b) Conductance-bias sweeps of the top wire at various TPL voltages. The DC bias values used to optimize reciprocity are indicated as colored points corresponding to the green and cyan contact configurations.

Finally, it is essential to ensure that the DC voltage across each QW remains within the bounds defined by the tunneling criteria outlined in Sec. 5.3. Specifically, the tunneling resistance between the two wires must exceed 10 MΩ for DC bias voltages within the range of ±1 mV (see Fig. 5.5). As shown in Fig. 6.9, the voltages resulting from the DC current biases used to optimize reciprocity — indicated by the gray reference lines — were all within this ±1 mV range. This confirms that the applied DC biases do not violate the tunneling constraint and that the drag measurements are conducted in a regime where inter-wire DC tunneling remains negligible.

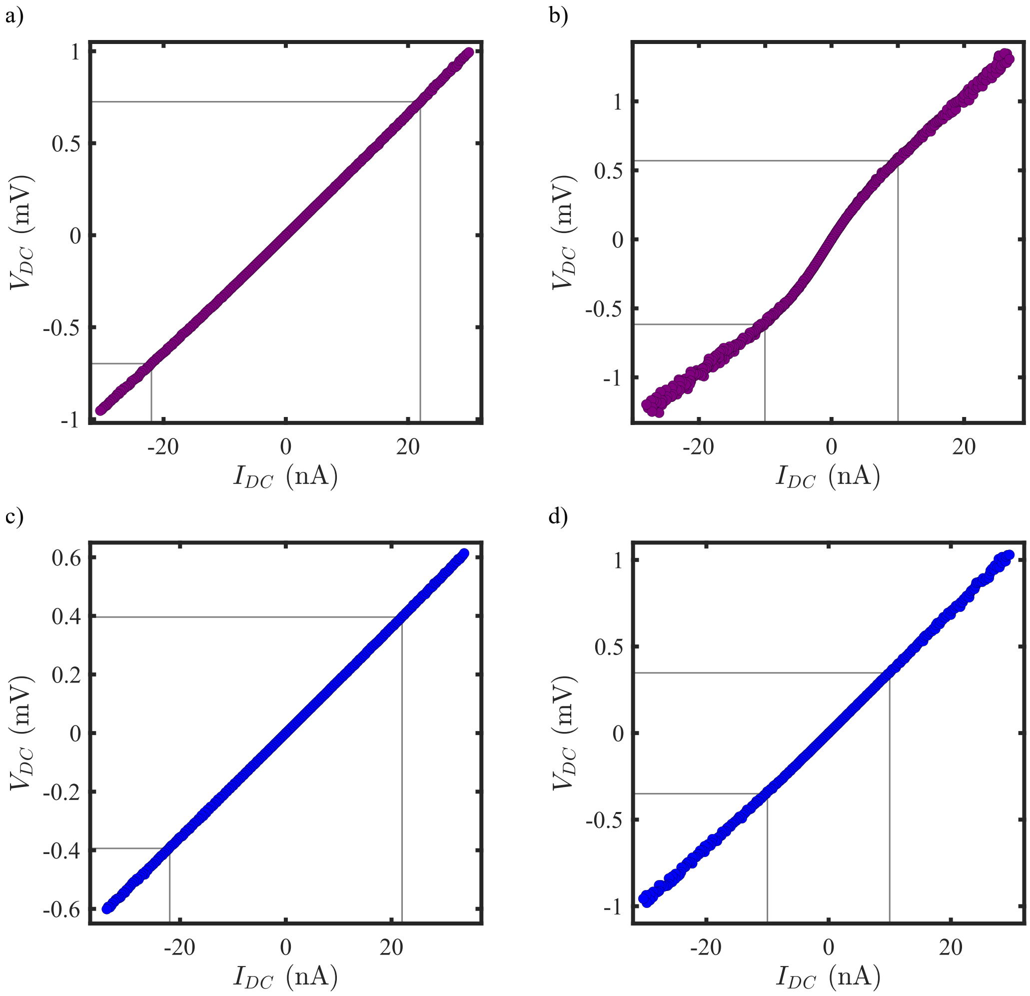

Figure 6.9: QW DC Linearity. a) First subband of the bottom wire TPL = -1.003 V. b) First subband of the top wire TPL = -1.003 V. c) Second subband of the bottom wire TPL = -0.896 V. d) Second subband of the top wire TPL = -0.896 V. In all four of these plots BPL = -1.065 V

6.4 Temperature Dependence

Fig. 6.10 presents the temperature dependence of the Coulomb drag signal under the same optimized reciprocity conditions as in Fig. 6.4 across all subbands and contact configurations. In each configuration, a distinct peak in the drag resistance was observed at the alignment of the first subbands, and this peak remained positive across the entire measured temperature range. Thermal broadening of the peak was evident in all four configuration. Only panel c) showed a slight increase in peak amplitude with increasing temperature; however, this increase was comparable to the noise level. Compared to the unbiased case shown in Fig. 5.16, the temperature mappings under DC bias were notably more consistent across configurations, showing that DC biasing enhanced the reciprocity of the drag response over the full temperature range tested here.

As in the unbiased case, continuous temperature sweeps were performed for both the 1–1 (Fig. 6.11) and 2–2 (Fig. 6.12) subband-aligned regimes corresponding to configuration a) in Fig. 6.10. In both cases, an upturn in the drag signal was observed as the temperature decreased. As before, exponential and power-law fits were applied to a selected temperature range (highlighted in yellow), chosen based on the quality of the fit.

The exponential and power-law fits were applied over the same temperature range, from 0.9 K to 1.3 K, for both the 1–1 and 2–2 datasets. To reveal any exponential behavior, the drag resistance is presented in Arrhenius form (Figs. 6.11 b and 6.12 b), where an exponential dependence appears as a linear trend. Similarly, the drag resistance is plotted in log–log form (Figs. 6.11 c and 6.12 c), where a power-law dependence manifests as a linear trend.

The parameter b obtained from the exponential fit over the selected temperature range for the 1–1 configuration is $T^* \sim b = (1.50 \pm 0.01)$ K, while for the 2–2 configuration it is $T^* \sim b = (1.73 \pm 0.03)$ K. The power-law fit yields $\beta = -(1.40 \pm 0.01)$

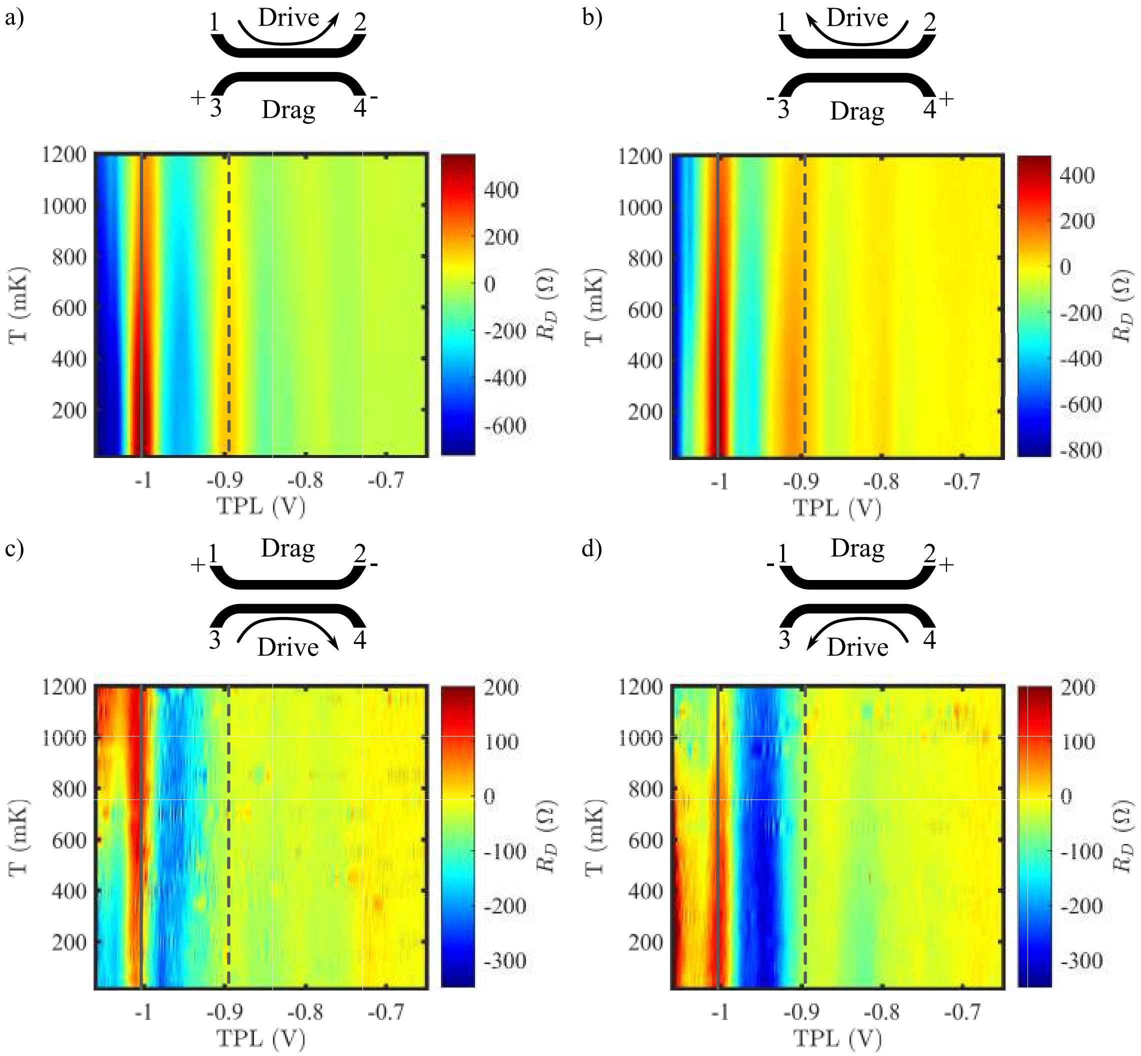

Figure 6.10: Temperature dependence of the Coulomb drag signal under reciprocity-optimized DC bias across all subband occupancies at BPL = -1.065 V for device B28C1-C measured with $V_{in} = 0.3$ V (1.5 nA). a) Drive wire current flowing from 1 to 2 with DC bias of -10 nA, drag voltage difference between 3 and 4 (green configuration). b) Drive 2 to 1 with DC bias of 10 nA, drag 4 and 3 (cyan configuration). c) Drive 3 to 4 with DC bias of 21.94 nA, drag 1 and 2 (red configuration). d) Drive 4 to 3 with DC bias of -21.94 nA, drag 2 and 1 (blue configuration). The solid grey lines indicate the alignment of the first subbands, while the dashed grey lines mark the alignment of the second subbands.

for the 1–1 case and $\beta = -(1.62 \pm 0.03)$ for the 2–2 case. Unlike the unbiased case discussed in Chapter 5, both values of β are reasonably close to the $-3/2$ exponent predicted by the forward-scattering model for $T > T_F$. Therefore, the forward-scattering model at $T > T_F$ and the backscattering model at $T > T^*$ are both

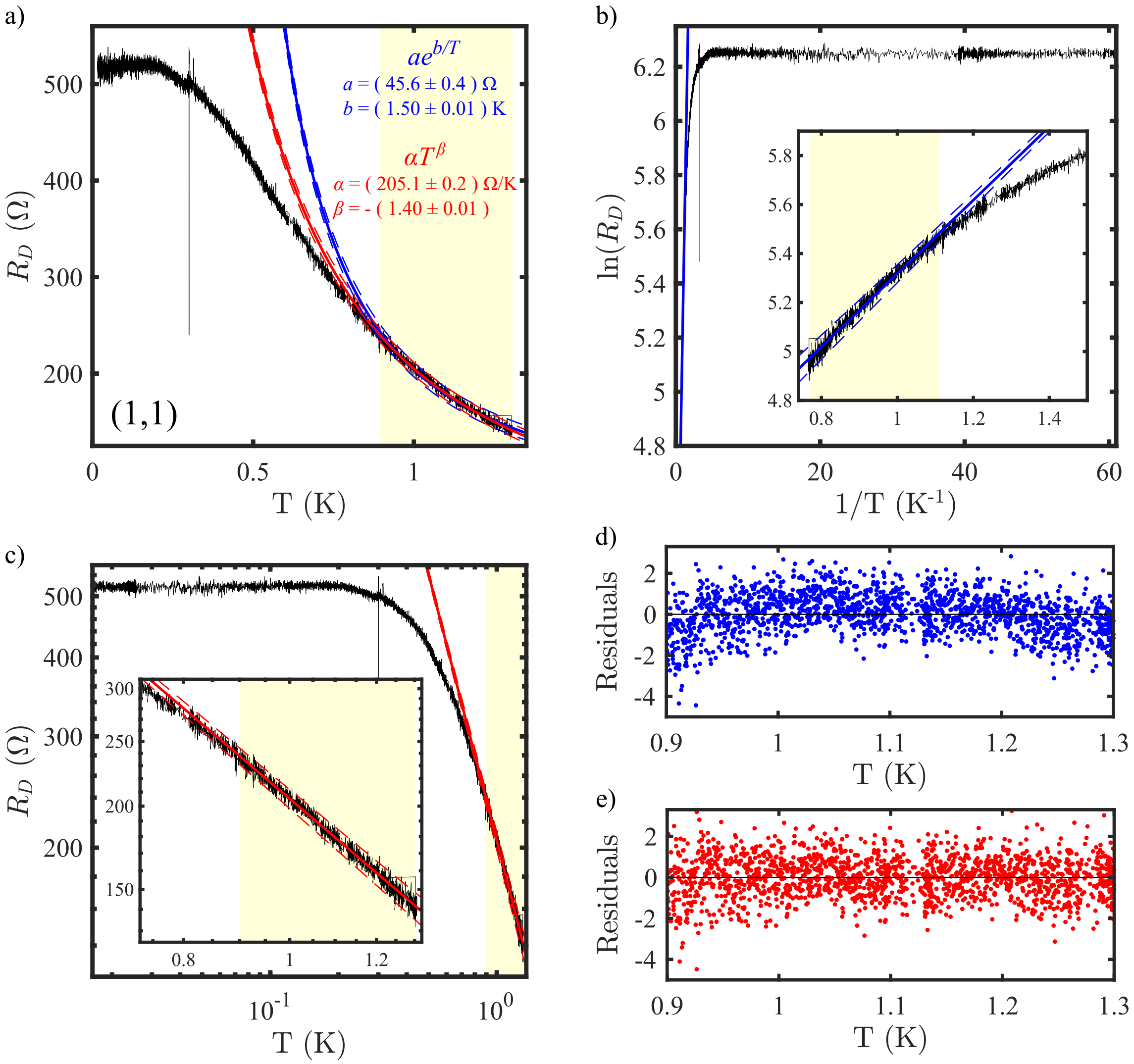

Figure 6.11: Continuous temperature dependence of the DC-biased drag signal with both wires in their first subband for configuration a) in Fig. 6.10. a) Coulomb drag signal: measured values are shown in black, the exponential fit in blue, and the power-law fit in red. The fits are performed over the data within the yellow-shaded region. Dashed lines indicate the 95% prediction bounds for the respective fits. b) Coulomb drag signal plotted on an Arrhenius scale. c) Coulomb drag signal plotted on a log-log scale. Insets provide a zoomed-in view of the fit region. d) Standardized residuals for the exponential fit. e) Standardized residuals for the power-law fit. Measurement parameters: BPL = -1.065 V, TPL = -1.003 V, I_{DC} = -10 nA, and V_{in} = 0.3 V. Uncertainties on the fitting parameters are statistical and are determined from the fit.

consistent with the observed signal. However, these β values deviate significantly from the -1 exponent expected for charge-fluctuation models in diffusive quantum wires, indicating that this model is not consistent with the observations. Since non-

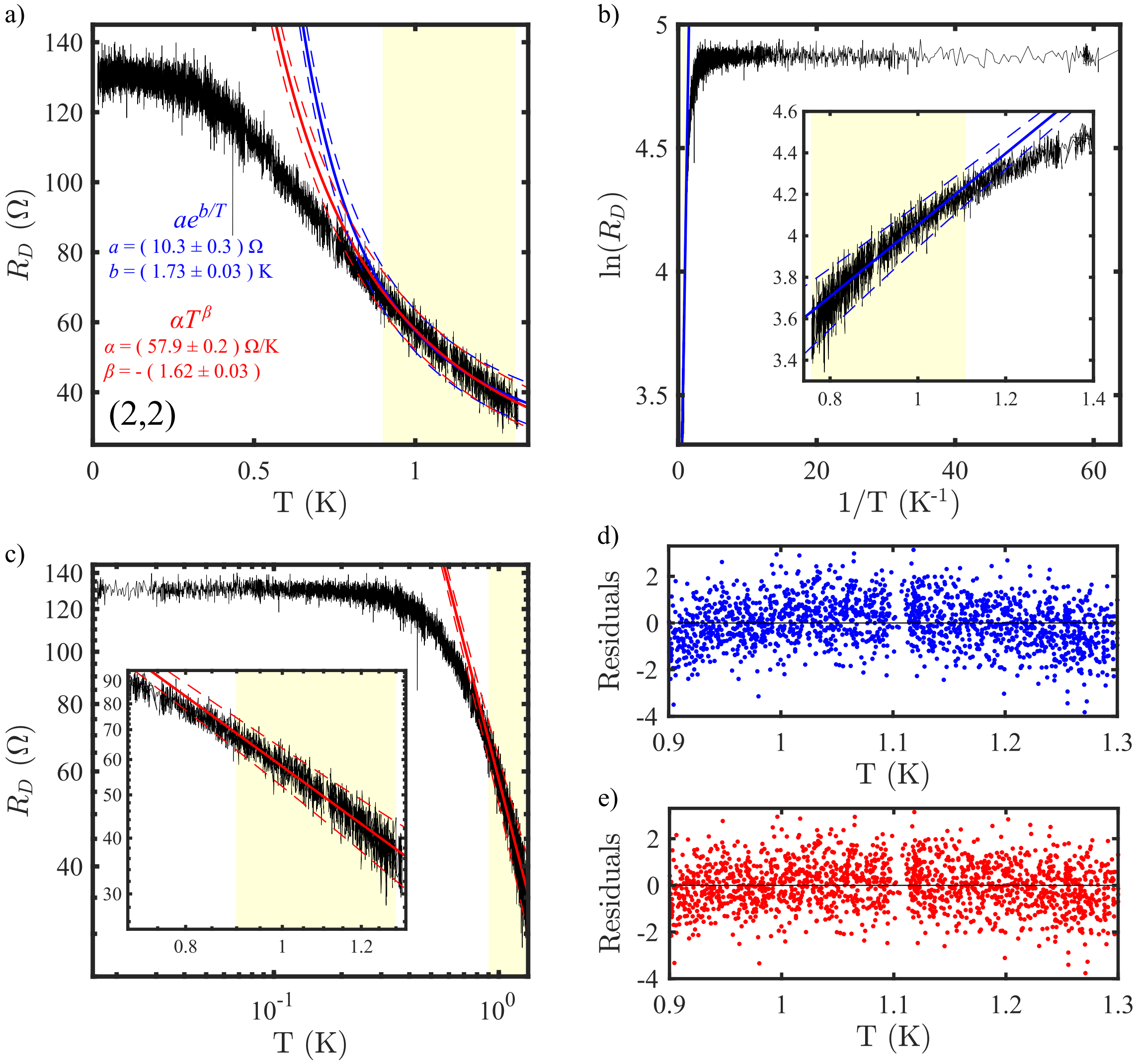

Figure 6.12: Continuous temperature dependence of the DC-biased drag signal with both wires in their second subband for configuration a) in Fig. 6.10. a) Coulomb drag signal. b) Coulomb drag signal plotted on an Arrhenius scale. c) Coulomb drag signal plotted on a log-log scale. d) Standardized residuals for the exponential fit. e) Standardized residuals for the power-law fit. Same parameters as in Fig. 6.11 except TPL = -0.896V. Uncertainties on the fitting parameters are statistical and are determined from the fit.

reciprocal signals can only be explained by charge-fluctuation models, the absence of a strong contribution from this regime in the temperature dependence is consistent with the improved reciprocity observed under DC bias. This, in turn, suggests that reciprocity-breaking contributions from nonlinear charge fluctuation rectifications are effectively suppressed by the application of an appropriate DC current bias.

The characterization of the drag signal presented in this chapter does not allow the identification of a single model responsible for the observed Coulomb drag. Over the selected temperature range, the data remain consistent with three theoretical frameworks: the strongly coupled Luttinger liquid model, the backscattering model, and the forward-scattering model. However, the residuals from the fits to the 1–1 data, shown in Figs. 6.11 d) and e), indicate that the power-law fits exhibit a slightly more random distribution of the residual around zero compared to the exponential fits. A similar trend is observed for the 2–2 data in Figs. 6.12 d) and e), although the effect is less pronounced. These observations suggest that the temperature dependence is more likely described by a backscattering or forward-scattering model than by an interlocked charge density wave in a strongly coupled Luttinger liquid.

As in Sec. 5.5.2, the reciprocal and nonreciprocal components of the drag signal can be extracted from the data in Fig. 6.10. Fig. 6.13 shows the results of this extraction for the temperature-dependent data of Fig. 6.10. Unlike the unbiased case (Fig. 5.19), the R_D^R components are similar regardless of whether the top or bottom QW is used as the drive wire. Furthermore, the R_D^{NR} components vary less with subband occupancy than the R_D^R components, an effect that is more pronounced when the top QW is the drive wire. Thermal broadening is evident in all components, independent of which QW is used as the drive wire.

Cuts at 1–1 and 2–2 from the data in Fig. 6.13 are shown in Fig. 6.14. When the drive current is applied to the top QW (Figs. 6.14 a and b), R_D^R at 1–1 exhibits significantly stronger temperature dependence than R_D^{NR}. In contrast, R_D^R at 2–2 and R_D^{NR} at both 1–1 and 2–2 display much weaker temperature dependence. When the bottom QW is the drive wire (Figs. 6.14 c and d), the temperature dependence of both R_D^R and R_D^{NR} in the 1–1 data is much more pronounced than in the 2–2 data; in fact, both components in the 2–2 case appear nearly independent of temperature. Unlike the case where the top QW is the drive wire, when the bottom QW is used, the R_D^R and R_D^{NR} components are of comparable magnitude but opposite sign. The increase in R_D^R and the decrease in R_D^{NR} in the biased 1–1 case, relative to

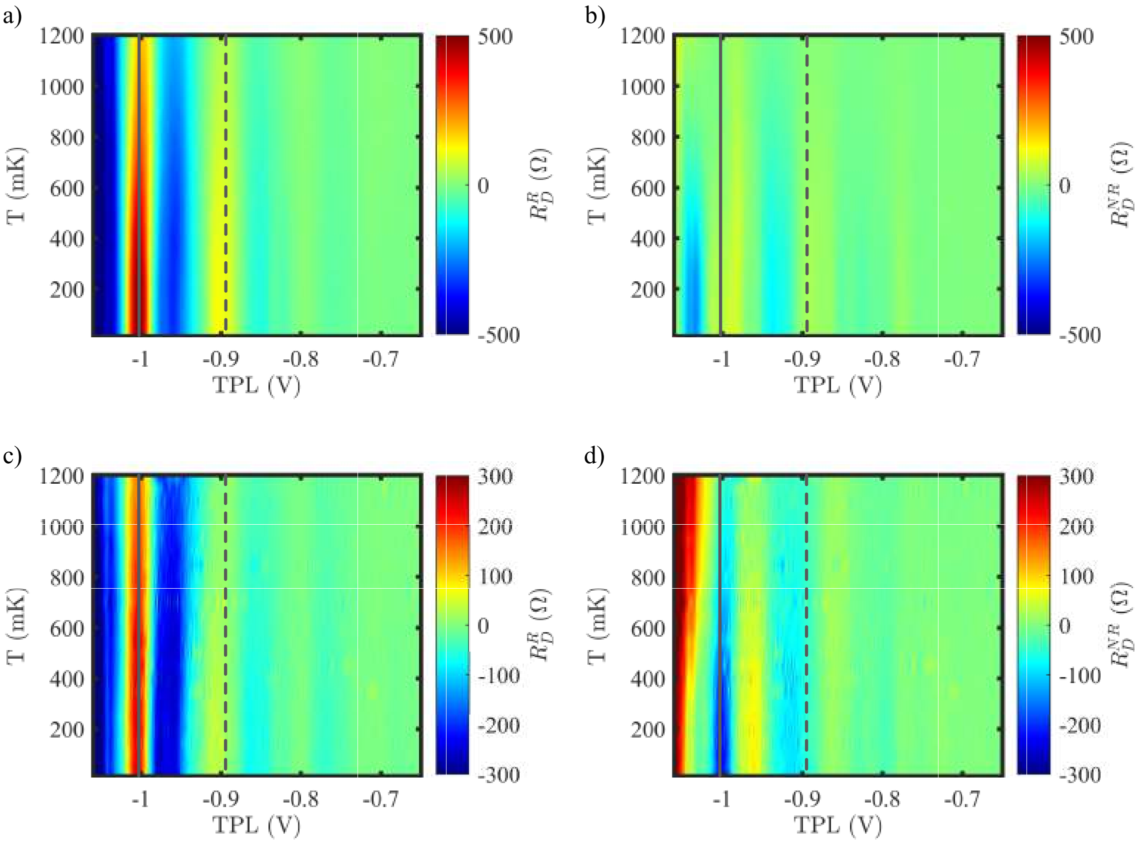

Figure 6.13: DC biased temperature-dependent mapping of reciprocal and nonreciprocal components of Coulomb drag resistance across all subband occupancies. a) and b): Reciprocal and nonreciprocal components, respectively, with the drive current applied to the top QW. c) and d): Reciprocal and nonreciprocal components, respectively, with the drive current applied to the bottom QW. Solid grey lines mark the alignment of the first subbands of both QWs, while dashed grey lines indicate the alignment of the second subbands.

the unbiased case, indicate that the reciprocal component becomes the dominant contribution to the drag signal under DC current bias.

The observed improvement in reciprocity upon applying a DC current bias has yet to be fully elucidated. A plausible explanation involves a compensation mechanism in which the DC bias counteracts the DC voltage generated by nonreciprocal rectification of fluctuations. However, further theoretical investigation is required to fully understand this mechanism. An alternative, phenomenological explanation is that the enhanced reciprocity arises from the increased kinetic energy of the drive and drag electrons induced by the DC bias current. In this picture, the higher elec-

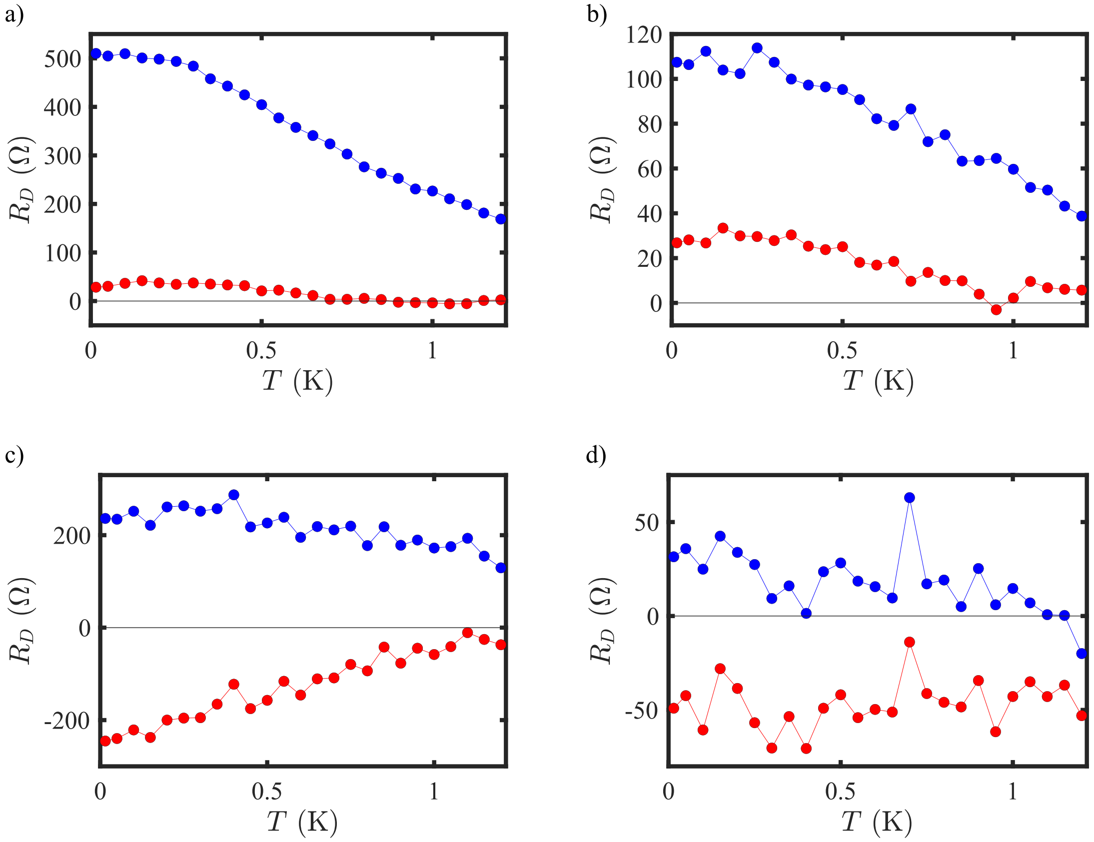

Figure 6.14: DC biased reciprocal (blue) and nonreciprocal (red) components of Coulomb drag resistance at subband alignments 1–1 (a, c) and 2–2 (b, d) as a function of temperature. a) and b): Drive current applied to the top QW. c) and d): Drive current applied to the bottom QW.

tron energies effectively reduce the influence of mesoscopic features responsible for reciprocity violations, rendering them less significant to the transport of the more energetic carriers. This scenario likewise requires further theoretical study to be properly assessed.

It is worth noting that the capability to selectively tune between reciprocal and nonreciprocal drag regimes was also demonstrated recently in a similar device architecture by Laroche's group [45]. In their study, the drag behavior could be modulated by tuning gate voltages and temperature, thereby enabling the study of nonlinear Coulomb drag between Luttinger liquids in the presence of disorder [46].

7

Conclusion and Outlook

7.1 Summary and Results

This thesis has investigated the interplay of electron-electron interaction in 1D system through the study of Coulomb Drag between vertically integrated QWs. While Luttinger liquid behavior was anticipated, the results revealed nonreciprocal behaviour, challenging the conventional expectation of reciprocity in our system. To investigate this unexpected behaviour, bias spectroscopy techniques were used to characterize the subband structure of the QWs. This led to the development of an equivalent bias spectroscopy method to probe the drag response under varying bias. These measurements demonstrated that reciprocity could be partially restored by applying an appropriate bias, suggesting that the initial nonreciprocity may arise from nonlinear rectification of charge fluctuation, which can be compensated by the applied DC bias. While the application of a DC bias clearly improves reciprocity, the underlying mechanism remains unclear and warrants further theoretical investigation.

This work was made possible by a custom-designed cryogenic infrastructure and a complex device fabrication process, which had to be adapted to the evolving constraints of CINT. The results presented here contribute to a deeper understanding of low-dimensional electron systems and open new avenues for probing exotic phenomena in strongly correlated quantum materials.

7.2 Future Work

There are many possible directions for research on Coulomb drag. Now that tunability between reciprocal and nonreciprocal drag has been demonstrated in three distinct ways — through the method presented in this work and those described in Ref. [45] — this field has become even more compelling. Of course, not all possible avenues can be covered here, but the following are some auspicious directions for future exploration.

As was previously done with laterally defined QWs by Debray's group and Yamamoto's group (Refs. [36,38]), a magnetic field study of the Coulomb drag signal in vertically integrated QWs would also be of great interest. Magnetic fields enhance electron correlations and enable exploration of the spin-resolved regime [113]. A careful evaluation of the magnetic field's effect on both the subband structure and the tunneling between wires would be necessary to ensure that the subbands are not significantly altered and that inter-wire tunneling remains negligible.

Performing thermal drag measurements between Luttinger liquids was one of the primary motivations behind this work. Now that both reciprocal and nonreciprocal drag can be selectively obtained, thermal drag in each regime could be explored. The most accessible starting point — requiring no modifications to the current device — would be to exploit the strong temperature dependence of Coulomb drag resistance as a thermometer, and use Joule heating to selectively warm the QWs. A measurement scheme similar to that used by Schmidt *et al.* [109] could be employed to thermally characterize the drag response. The next step would be to fully characterize the thermoelectric drag matrix described in Ref. [114], using a modified device equipped with electron temperature measurement capabilities in the 2DEG reservoirs near the QW, along with integrated heaters to selectively warm specific regions of the device. It is important to note that thermal conductance in a Luttinger liquid is expected to deviate significantly from Fermi liquid predictions [115]. In fact, violations of the Wiedemann–Franz law have been observed in one-dimensional systems [116]. Towards this end, additional details on thermal drag are provided in Appendix H.

7.3 Closing Remarks

The experimental results in this thesis have shown that the reciprocity of the Coulomb drag signal between two vertically integrated QWs can be improved by applying a specific DC current bias in the drive wire. This tunability enables the study of both reciprocal and nonreciprocal Coulomb drag simply by adjusting the DC bias, paving the way for compelling investigations of thermal drag and other effects in both regimes. Thermal drag could potentially be exploited to recover energy dissipated in electronic circuits, and the platform developed in this work provides a promising avenue to explore this possibility as suggested by Büttiker and Sánchez in a news and views article in nature nanotechnology [117] following a paper by the Gervais group.

A

Appendix A: Magnetic Field Distribution of the Tri-axis Magnet

A.1 Field Distribution from 6T in the z-direction

The magnetic field profile provided by Oxford Instruments for a 6 T field applied in the z-direction is shown in Fig. A.1. Panel a) displays the z-component of the magnetic field, B_z, while panel b) shows the radial component, B_r. Additionally, Fig. A.2 presents B_z as a function of the axial distance from the center of the magnetic field along the z-axis.

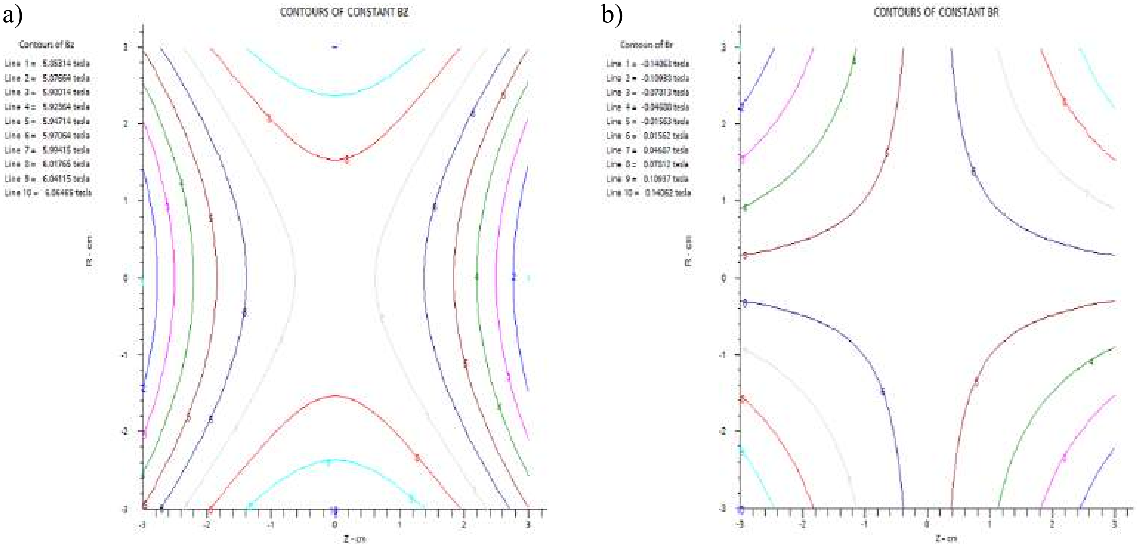

Figure A.1: Magnetic field profile at 6 T in the z-direction. a) z-component of the magnetic field, B_z. b) Radial component of the magnetic field, B_r. Figure courtesy of Oxford Instruments.

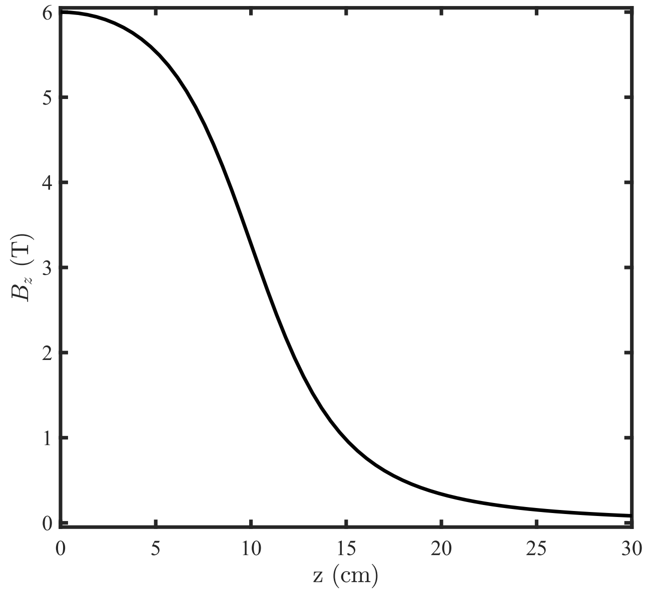

Figure A.2: z-component of the magnetic field, B_z, as a function of the axial distance from the field center (in the z-direction), under an applied magnetic field of 6 T along the z-axis.

A.2 Field from 1T in the x-direction

The magnetic field profile provided by Oxford Instruments for a 1 T field applied in the x-direction is shown in Fig. A.3. Panel a) displays the z-component of the magnetic field, B_z, while panel b) shows the radial component, B_r. Additionally, Fig. A.4 presents B_x as a function of the axial distance from the center of the magnetic field along the z-axis.

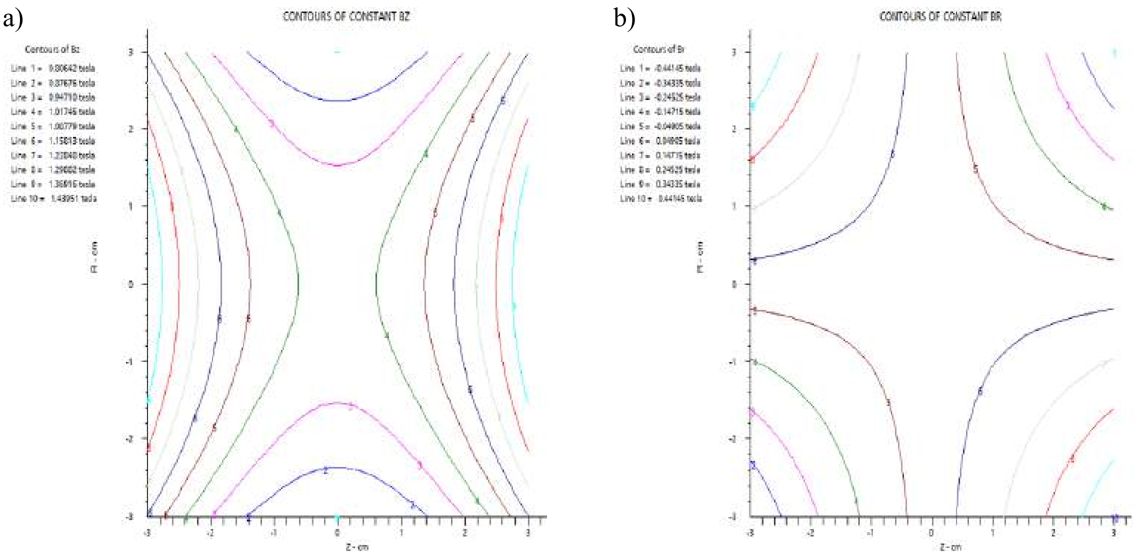

Figure A.3: Magnetic field profile at 1 T in the x-direction. a) z-component of the magnetic field, B_z. b) Radial component of the magnetic field, B_r. Figure courtesy of Oxford Instruments.

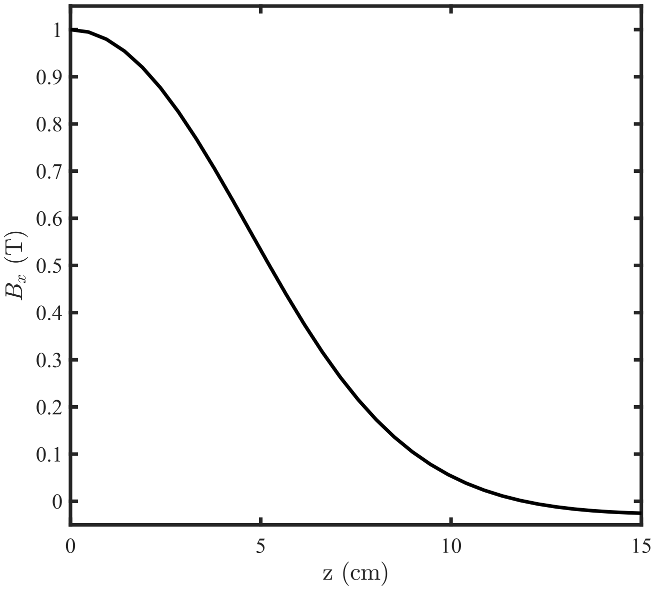

Figure A.4: x-component of the magnetic field, B_x, as a function of the axial distance from the field center (in the z-direction), under an applied magnetic field of 1 T along the x-axis.

B

Appendix B: Eddy Current Calculations

B.1 Drilled Vertical Plates

For a rectangular prism with a base width w, thickness d, and total volume V, placed in a time-varying magnetic field with rate of change $\dot{B}$, and composed of a material with electrical resistivity ρ_e, the heat generated by eddy current is given by

$$\dot{Q} = \frac{GV\dot{B}^2}{\rho_e}, \quad \text{with} \quad G = \frac{d^2}{16}\left(\frac{k^2}{1+k^2}\right), \tag{B.1}$$

where $k = w/d$ is the aspect ratio of the base. For a single drilled plate used in the tail of the Triton cryostat, subjected to a magnetic field variation of $\dot{B} = 0.25$ T/min, the heat generated by eddy currents is approximately [90]

$$\dot{Q} = \begin{cases} 41.3\ \text{nW} & \text{for coin silver} \\ 1.60\ \mu\text{W} & \text{for pure silver} \end{cases} . \tag{B.2}$$

B.2 Base Plates

For a disk of radius r, and total volume V, placed in a time-varying magnetic field with rate of change $\dot{B}$, and composed of a material with electrical resistivity ρ_e, the heat generated by eddy current is given by

$$\dot{Q} = \frac{GV\dot{B}^2}{\rho_e}, \quad \text{with} \quad G = \frac{r^2}{8}. \tag{B.3}$$

For the base plate used in the tail of the Triton cryostat, subjected to a magnetic field variation of $\dot{B} = 0.25$ T/min, the heat generated by eddy currents is approximately

$$\dot{Q} = \begin{cases} 6.507\ \mu\text{W} & \text{for coin silver} \\ 250.4\ \text{mW} & \text{for pure silver} \end{cases} . \tag{B.4}$$

C

Appendix C: Fabrication Recipe

The detailed fabrication recipe used for the devices produced from wafer VA0486 is provided in Figs. C.1, C.2, and C.3. Over the course of this Ph.D. project, a total of 80 chips were fabricated using six different wafers. Each chip contains three devices, resulting in a total of 240 fabricated devices. Of these, 160 devices were tested experimentally.

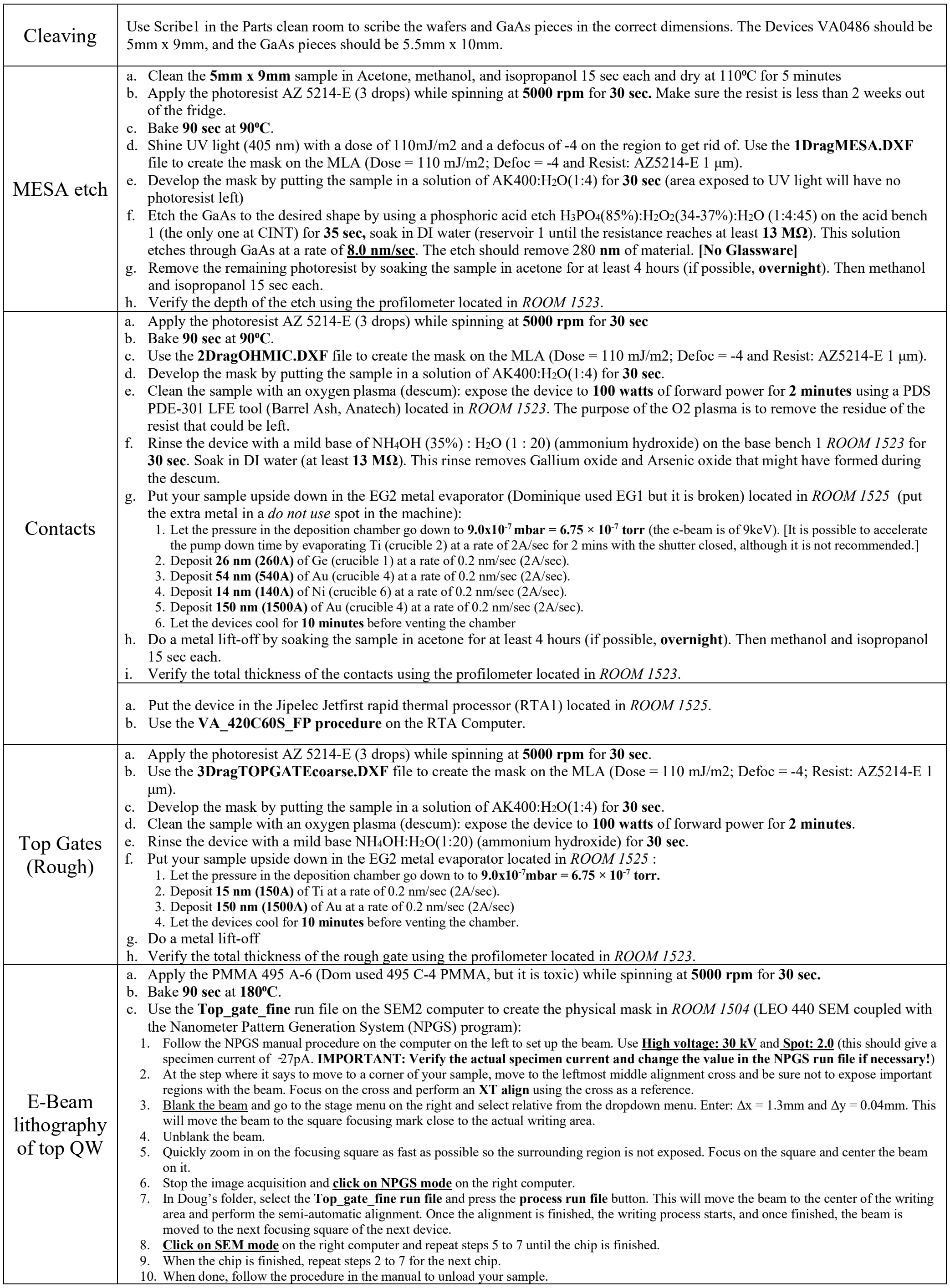

Cleaving	Use Scribe1 in the Parts clean room to scribe the wafers and GaAs pieces in the correct dimensions. The Devices VA0486 should be 5mm x 9mm, and the GaAs pieces should be 5.5mm x 10mm.
MESA etch	a. Clean the **5mm x 9mm** sample in Acetone, methanol, and isopropanol 15 sec each and dry at 110ºC for 5 minutes b. Apply the photoresist AZ 5214-E (3 drops) while spinning at **5000 rpm** for **30 sec.** Make sure the resist is less than 2 weeks out of the fridge. c. Bake **90 sec** at **90ºC**. d. Shine UV light (405 nm) with a dose of 110mJ/m2 and a defocus of -4 on the region to get rid of. Use the **1DragMESA.DXF** file to create the mask on the MLA (Dose = 110 mJ/m2; Defoc = -4 and Resist: AZ5214-E 1 µm). e. Develop the mask by putting the sample in a solution of AK400:H_2O(1:4) for **30 sec** (area exposed to UV light will have no photoresist left) f. Etch the GaAs to the desired shape by using a phosphoric acid etch H_3PO_4(85%):H_2O_2(34-37%):H_2O (1:4:45) on the acid bench 1 (the only one at CINT) for **35 sec,** soak in DI water (reservoir 1 until the resistance reaches at least **13 MΩ**). This solution etches through GaAs at a rate of **8.0 nm/sec**. The etch should remove 280 **nm** of material. **[No Glassware]** g. Remove the remaining photoresist by soaking the sample in acetone for at least 4 hours (if possible, **overnight**). Then methanol and isopropanol 15 sec each. h. Verify the depth of the etch using the profilometer located in *ROOM 1523*.
Contacts	a. Apply the photoresist AZ 5214-E (3 drops) while spinning at **5000 rpm** for **30 sec** b. Bake **90 sec** at **90ºC**. c. Use the **2DragOHMIC.DXF** file to create the mask on the MLA (Dose = 110 mJ/m2; Defoc = -4 and Resist: AZ5214-E 1 µm). d. Develop the mask by putting the sample in a solution of AK400:H_2O(1:4) for **30 sec**. e. Clean the sample with an oxygen plasma (descum): expose the device to **100 watts** of forward power for **2 minutes** using a PDS PDE-301 LFE tool (Barrel Ash, Anatech) located in *ROOM 1523*. The purpose of the O2 plasma is to remove the residue of the resist that could be left. f. Rinse the device with a mild base of NH_4OH (35%) : H_2O (1 : 20) (ammonium hydroxide) on the base bench 1 *ROOM 1523* for **30 sec**. Soak in DI water (at least **13 MΩ**). This rinse removes Gallium oxide and Arsenic oxide that might have formed during the descum. g. Put your sample upside down in the EG2 metal evaporator (Dominique used EG1 but it is broken) located in *ROOM 1525* (put the extra metal in a *do not use* spot in the machine): 1. Let the pressure in the deposition chamber go down to **$9.0x10^{-7}$ mbar = 6.75×10^{-7} torr** (the e-beam is of 9keV). [It is possible to accelerate the pump down time by evaporating Ti (crucible 2) at a rate of 2A/sec for 2 mins with the shutter closed, although it is not recommended.] 2. Deposit **26 nm (260A)** of Ge (crucible 1) at a rate of 0.2 nm/sec (2A/sec). 3. Deposit **54 nm (540A)** of Au (crucible 4) at a rate of 0.2 nm/sec (2A/sec). 4. Deposit **14 nm (140A)** of Ni (crucible 6) at a rate of 0.2 nm/sec (2A/sec). 5. Deposit **150 nm (1500A)** of Au (crucible 4) at a rate of 0.2 nm/sec (2A/sec). 6. Let the devices cool for **10 minutes** before venting the chamber h. Do a metal lift-off by soaking the sample in acetone for at least 4 hours (if possible, **overnight**). Then methanol and isopropanol 15 sec each. i. Verify the total thickness of the contacts using the profilometer located in *ROOM 1523*.
	a. Put the device in the Jipelec Jetfirst rapid thermal processor (RTA1) located in *ROOM 1525*. b. Use the **VA_420C60S_FP procedure** on the RTA Computer.
Top Gates (Rough)	a. Apply the photoresist AZ 5214-E (3 drops) while spinning at **5000 rpm** for **30 sec**. b. Use the **3DragTOPGATEcoarse.DXF** file to create the mask on the MLA (Dose = 110 mJ/m2; Defoc = -4; Resist: AZ5214-E 1 µm). c. Develop the mask by putting the sample in a solution of AK400:H_2O(1:4) for **30 sec**. d. Clean the sample with an oxygen plasma (descum): expose the device to **100 watts** of forward power for **2 minutes**. e. Rinse the device with a mild base NH_4OH:H_2O(1:20) (ammonium hydroxide) for **30 sec**. f. Put your sample upside down in the EG2 metal evaporator located in *ROOM 1525* : 1. Let the pressure in the deposition chamber go down to to **$9.0x10^{-7}$mbar = 6.75×10^{-7} torr.** 2. Deposit **15 nm (150A)** of Ti at a rate of 0.2 nm/sec (2A/sec). 3. Deposit **150 nm (1500A)** of Au at a rate of 0.2 nm/sec (2A/sec) 4. Let the devices cool for **10 minutes** before venting the chamber. g. Do a metal lift-off h. Verify the total thickness of the rough gate using the profilometer located in *ROOM 1523*.
E-Beam lithography of top QW	a. Apply the PMMA 495 A-6 (Dom used 495 C-4 PMMA, but it is toxic) while spinning at **5000 rpm** for **30 sec.** b. Bake **90 sec** at **180ºC**. c. Use the **Top_gate_fine** run file on the SEM2 computer to create the physical mask in *ROOM 1504* (LEO 440 SEM coupled with the Nanometer Pattern Generation System (NPGS) program): 1. Follow the NPGS manual procedure on the computer on the left to set up the beam. Use **High voltage: 30 kV** and **Spot: 2.0** (this should give a specimen current of ~27pA. **IMPORTANT: Verify the actual specimen current and change the value in the NPGS run file if necessary!**) 2. At the step where it says to move to a corner of your sample, move to the leftmost middle alignment cross and be sure not to expose important regions with the beam. Focus on the cross and perform an **XT align** using the cross as a reference. 3. Blank the beam and go to the stage menu on the right and select relative from the dropdown menu. Enter: Δx = 1.3mm and Δy = 0.04mm. This will move the beam to the square focusing mark close to the actual writing area. 4. Unblank the beam. 5. Quickly zoom in on the focusing square as fast as possible so the surrounding region is not exposed. Focus on the square and center the beam on it. 6. Stop the image acquisition and **click on NPGS mode** on the right computer. 7. In Doug's folder, select the **Top_gate_fine run file** and press the **process run file** button. This will move the beam to the center of the writing area and perform the semi-automatic alignment. Once the alignment is finished, the writing process starts, and once finished, the beam is moved to the next focusing square of the next device. 8. **Click on SEM mode** on the right computer and repeat steps 5 to 7 until the chip is finished. 9. When the chip is finished, repeat steps 2 to 7 for the next chip. 10. When done, follow the procedure in the manual to unload your sample.

Figure C.1: Device fabrication recipe 1/3.

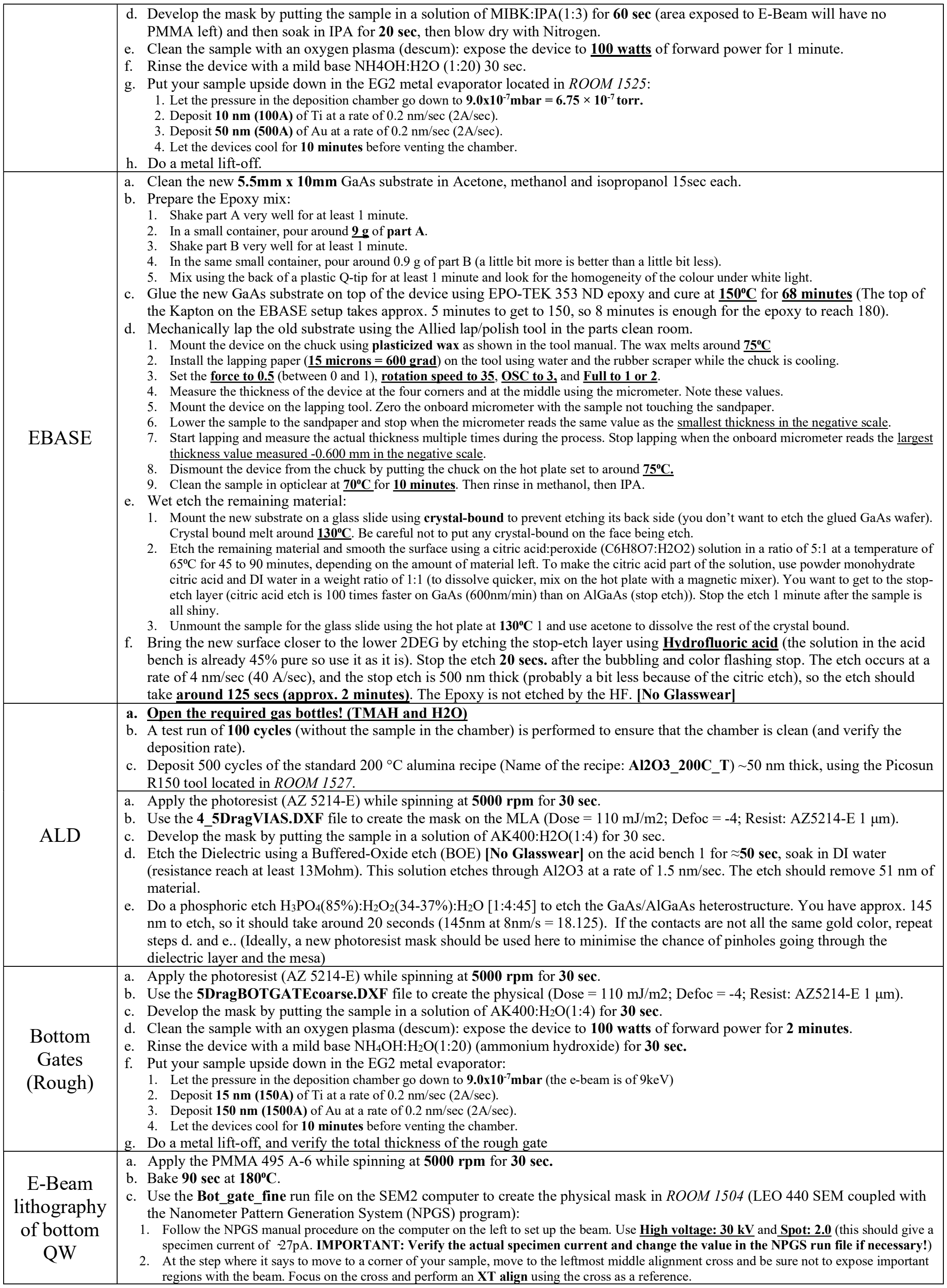

	d. Develop the mask by putting the sample in a solution of MIBK:IPA(1:3) for **60 sec** (area exposed to E-Beam will have no PMMA left) and then soak in IPA for **20 sec**, then blow dry with Nitrogen.
	e. Clean the sample with an oxygen plasma (descum): expose the device to **100 watts** of forward power for 1 minute.
	f. Rinse the device with a mild base NH4OH:H2O (1:20) 30 sec.
	g. Put your sample upside down in the EG2 metal evaporator located in *ROOM 1525*:
	  1. Let the pressure in the deposition chamber go down to **$9.0x10^{-7}$mbar = 6.75×10^{-7} torr.**
	  2. Deposit **10 nm (100A)** of Ti at a rate of 0.2 nm/sec (2A/sec).
	  3. Deposit **50 nm (500A)** of Au at a rate of 0.2 nm/sec (2A/sec).
	  4. Let the devices cool for **10 minutes** before venting the chamber.
	h. Do a metal lift-off.

EBASE	a. Clean the new **5.5mm x 10mm** GaAs substrate in Acetone, methanol and isopropanol 15sec each.
	b. Prepare the Epoxy mix:
	  1. Shake part A very well for at least 1 minute.
	  2. In a small container, pour around **9 g** of **part A**.
	  3. Shake part B very well for at least 1 minute.
	  4. In the same small container, pour around 0.9 g of part B (a little bit more is better than a little bit less).
	  5. Mix using the back of a plastic Q-tip for at least 1 minute and look for the homogeneity of the colour under white light.
	c. Glue the new GaAs substrate on top of the device using EPO-TEK 353 ND epoxy and cure at **150ºC** for **68 minutes** (The top of the Kapton on the EBASE setup takes approx. 5 minutes to get to 150, so 8 minutes is enough for the epoxy to reach 180).
	d. Mechanically lap the old substrate using the Allied lap/polish tool in the parts clean room.
	  1. Mount the device on the chuck using **plasticized wax** as shown in the tool manual. The wax melts around **75ºC**
	  2. Install the lapping paper (**15 microns = 600 grad**) on the tool using water and the rubber scraper while the chuck is cooling.
	  3. Set the **force to 0.5** (between 0 and 1), **rotation speed to 35**, **OSC to 3,** and **Full to 1 or 2**.
	  4. Measure the thickness of the device at the four corners and at the middle using the micrometer. Note these values.
	  5. Mount the device on the lapping tool. Zero the onboard micrometer with the sample not touching the sandpaper.
	  6. Lower the sample to the sandpaper and stop when the micrometer reads the same value as the smallest thickness in the negative scale.
	  7. Start lapping and measure the actual thickness multiple times during the process. Stop lapping when the onboard micrometer reads the largest thickness value measured -0.600 mm in the negative scale.
	  8. Dismount the device from the chuck by putting the chuck on the hot plate set to around **75ºC.**
	  9. Clean the sample in opticlear at **70ºC** for **10 minutes**. Then rinse in methanol, then IPA.
	e. Wet etch the remaining material:
	  1. Mount the new substrate on a glass slide using **crystal-bound** to prevent etching its back side (you don't want to etch the glued GaAs wafer). Crystal bound melt around **130ºC**. Be careful not to put any crystal-bound on the face being etch.
	  2. Etch the remaining material and smooth the surface using a citric acid:peroxide (C6H8O7:H2O2) solution in a ratio of 5:1 at a temperature of 65ºC for 45 to 90 minutes, depending on the amount of material left. To make the citric acid part of the solution, use powder monohydrate citric acid and DI water in a weight ratio of 1:1 (to dissolve quicker, mix on the hot plate with a magnetic mixer). You want to get to the stop-etch layer (citric acid etch is 100 times faster on GaAs (600nm/min) than on AlGaAs (stop etch)). Stop the etch 1 minute after the sample is all shiny.
	  3. Unmount the sample for the glass slide using the hot plate at **130ºC** 1 and use acetone to dissolve the rest of the crystal bound.
	f. Bring the new surface closer to the lower 2DEG by etching the stop-etch layer using **Hydrofluoric acid** (the solution in the acid bench is already 45% pure so use it as it is). Stop the etch **20 secs.** after the bubbling and color flashing stop. The etch occurs at a rate of 4 nm/sec (40 A/sec), and the stop etch is 500 nm thick (probably a bit less because of the citric etch), so the etch should take **around 125 secs (approx. 2 minutes)**. The Epoxy is not etched by the HF. **[No Glasswear]**

ALD	**a. Open the required gas bottles! (TMAH and H2O)** b. A test run of **100 cycles** (without the sample in the chamber) is performed to ensure that the chamber is clean (and verify the deposition rate). c. Deposit 500 cycles of the standard 200 °C alumina recipe (Name of the recipe: **Al2O3_200C_T**) ~50 nm thick, using the Picosun R150 tool located in *ROOM 1527*.
	a. Apply the photoresist (AZ 5214-E) while spinning at **5000 rpm** for **30 sec**. b. Use the **4_5DragVIAS.DXF** file to create the mask on the MLA (Dose = 110 mJ/m2; Defoc = -4; Resist: AZ5214-E 1 µm). c. Develop the mask by putting the sample in a solution of AK400:H2O(1:4) for 30 sec. d. Etch the Dielectric using a Buffered-Oxide etch (BOE) **[No Glasswear]** on the acid bench 1 for ≈**50 sec**, soak in DI water (resistance reach at least 13Mohm). This solution etches through Al2O3 at a rate of 1.5 nm/sec. The etch should remove 51 nm of material. e. Do a phosphoric etch H_3PO_4(85%):H_2O_2(34-37%):H_2O [1:4:45] to etch the GaAs/AlGaAs heterostructure. You have approx. 145 nm to etch, so it should take around 20 seconds (145nm at 8nm/s = 18.125). If the contacts are not all the same gold color, repeat steps d. and e.. (Ideally, a new photoresist mask should be used here to minimise the chance of pinholes going through the dielectric layer and the mesa)

Bottom Gates (Rough)	a. Apply the photoresist (AZ 5214-E) while spinning at **5000 rpm** for **30 sec**.
	b. Use the **5DragBOTGATEcoarse.DXF** file to create the physical (Dose = 110 mJ/m2; Defoc = -4; Resist: AZ5214-E 1 µm).
	c. Develop the mask by putting the sample in a solution of AK400:H_2O(1:4) for **30 sec**.
	d. Clean the sample with an oxygen plasma (descum): expose the device to **100 watts** of forward power for **2 minutes**.
	e. Rinse the device with a mild base NH_4OH:H_2O(1:20) (ammonium hydroxide) for **30 sec.**
	f. Put your sample upside down in the EG2 metal evaporator:
	  1. Let the pressure in the deposition chamber go down to **$9.0x10^{-7}$mbar** (the e-beam is of 9keV)
	  2. Deposit **15 nm (150A)** of Ti at a rate of 0.2 nm/sec (2A/sec).
	  3. Deposit **150 nm (1500A)** of Au at a rate of 0.2 nm/sec (2A/sec).
	  4. Let the devices cool for **10 minutes** before venting the chamber.
	g. Do a metal lift-off, and verify the total thickness of the rough gate

E-Beam lithography of bottom QW	a. Apply the PMMA 495 A-6 while spinning at **5000 rpm** for **30 sec.**
	b. Bake **90 sec** at **180ºC**.
	c. Use the **Bot_gate_fine** run file on the SEM2 computer to create the physical mask in *ROOM 1504* (LEO 440 SEM coupled with the Nanometer Pattern Generation System (NPGS) program):
	  1. Follow the NPGS manual procedure on the computer on the left to set up the beam. Use **High voltage: 30 kV** and **Spot: 2.0** (this should give a specimen current of ~27pA. **IMPORTANT: Verify the actual specimen current and change the value in the NPGS run file if necessary!**)
	  2. At the step where it says to move to a corner of your sample, move to the leftmost middle alignment cross and be sure not to expose important regions with the beam. Focus on the cross and perform an **XT align** using the cross as a reference.

Figure C.2: Device fabrication recipe 2/3.

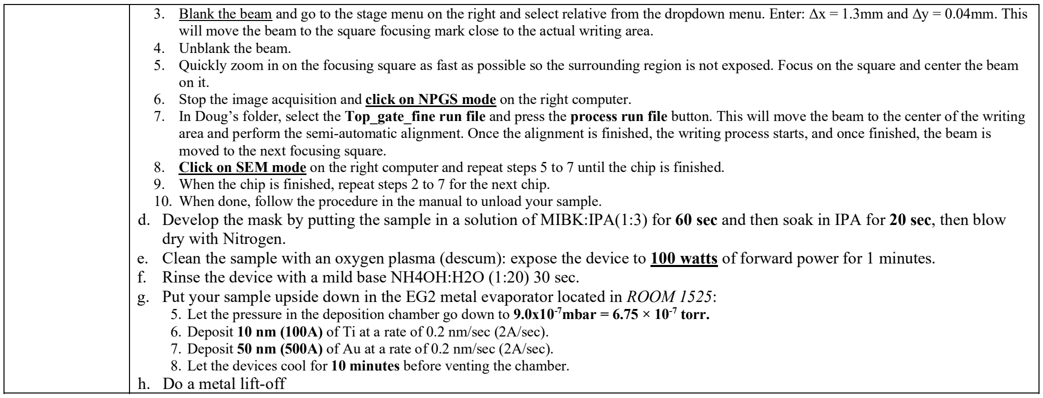

3. Blank the beam and go to the stage menu on the right and select relative from the dropdown menu. Enter: Δx = 1.3mm and Δy = 0.04mm. This will move the beam to the square focusing mark close to the actual writing area.
4. Unblank the beam.
5. Quickly zoom in on the focusing square as fast as possible so the surrounding region is not exposed. Focus on the square and center the beam on it.
6. Stop the image acquisition and **click on NPGS mode** on the right computer.
7. In Doug's folder, select the **Top_gate_fine run file** and press the **process run file** button. This will move the beam to the center of the writing area and perform the semi-automatic alignment. Once the alignment is finished, the writing process starts, and once finished, the beam is moved to the next focusing square.
8. **Click on SEM mode** on the right computer and repeat steps 5 to 7 until the chip is finished.
9. When the chip is finished, repeat steps 2 to 7 for the next chip.
10. When done, follow the procedure in the manual to unload your sample.

d. Develop the mask by putting the sample in a solution of MIBK:IPA(1:3) for **60 sec** and then soak in IPA for **20 sec**, then blow dry with Nitrogen.

e. Clean the sample with an oxygen plasma (descum): expose the device to **100 watts** of forward power for 1 minutes.

f. Rinse the device with a mild base NH4OH:H2O (1:20) 30 sec.

g. Put your sample upside down in the EG2 metal evaporator located in *ROOM 1525*:

5. Let the pressure in the deposition chamber go down to **9.0x10^{-7}mbar = 6.75 × 10^{-7} torr.**
6. Deposit **10 nm (100A)** of Ti at a rate of 0.2 nm/sec (2A/sec).
7. Deposit **50 nm (500A)** of Au at a rate of 0.2 nm/sec (2A/sec).
8. Let the devices cool for **10 minutes** before venting the chamber.

h. Do a metal lift-off

Figure C.3: Device fabrication recipe 3/3.

D

Appendix D: Devices Nomenclature

Given the large number of devices fabricated during this Ph.D. project, a clear and consistent nomenclature is essential to ensure traceability of both devices and experimental results. Devices were fabricated in batches, each consisting of multiple chips. Each batch was assigned a unique number, which appears as the first element in the device name. For example, a device fabricated in batch 16 will have a name beginning with B16. Within each batch, individual chips were also numbered. The second number in the device name corresponds to the chip number, so a device located on chip 2 of batch 16 is designated B16C2. The final part of the device name identifies which of the three devices on the chip is being referenced, as defined in Fig. D.1. For instance, the leftmost device on chip 2 of batch 16 is referred to as B16C2-L.

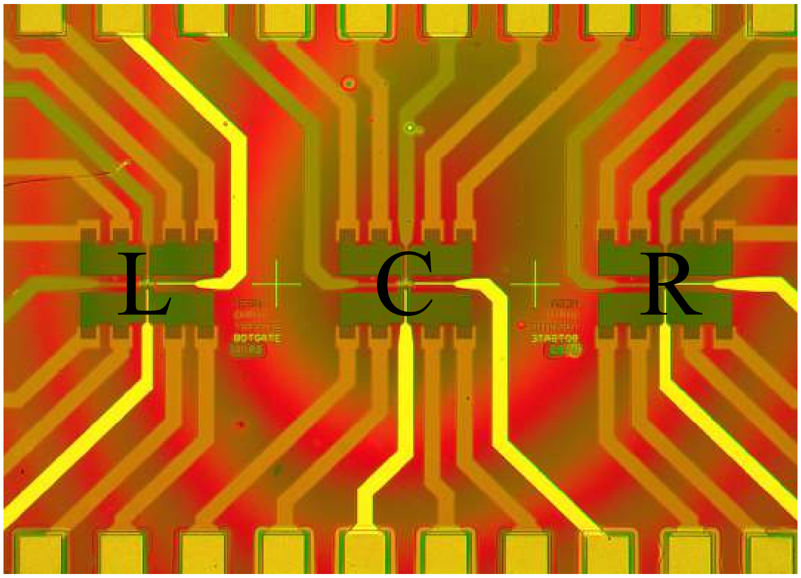

Figure D.1: Photograph of a completed chip containing three vertically integrated 1D–1D drag devices. The nomenclature for each device on this specific chip is written on top of each device: L for the left device, C for the center device, and R for the right device.

E

Appendix E: Observed Failures of Devices

Drag devices can fail through various mechanisms. Table E.1 summarizes the observed failure modes along with plausible explanations. A noteworthy observation is that vertically integrated QWs fabricated using the EBASE procedure exhibit high sensitivity to the warm-up rate and have a limited number of thermal cycles before degradation occurs. In some cases, devices ceased functioning between two consecutive cooldowns. Prior to failure, these devices displayed well-defined subband structures and measurable drag signals; however, upon the next cooldown, the 2DEG would get pinched off before any subband structure could be observed. This phenomenon was observed in four devices from different fabrication batches. The precise aging mechanism responsible for this behavior remains unclear, but data reported in [118] suggest that it may be caused by trapped charges or dopants that

Symptoms	Possible Causes
High contact resistance	Bad metal deposition; inadequate annealing; vias not etched sufficiently.
Gates have no effect	Faulty e-beam lithography; bad metal liftoff; physical damage to gates.
Gate leakage	Faulty e-beam lithography; compromised ALD layer; soldering errors (short between contact pads).
PO gate sweeps have less or more then two plateau	Bad wafer; bad location on the wafer; improper mesa etch; bad ALD layer.
Hysteresis in gate sweeps	Bad wafer; bad location on the wafer; bad ALD layer.
PL gates are pinching off the 2DEG with no subband structure	Bad e-beam lithography; excessive gate-to-2DEG distance; insufficient PL–PO gate spacing; device degradation due to repeated thermal cycling or rapid warm-up.
Tunneling resistance fails to meet the 10 MΩ criterion	Bad wafer; bad location on the wafer.
Drift in the drag signal or conductance	Bad wafer; bad location on the wafer; bad ALD layer; bad lithography (resist or PMMA residue).

Table E.1: Observed failure mechanisms in drag devices and their possible causes.

weaken the confining potential.

F

Appendix F: Layer Potential Difference

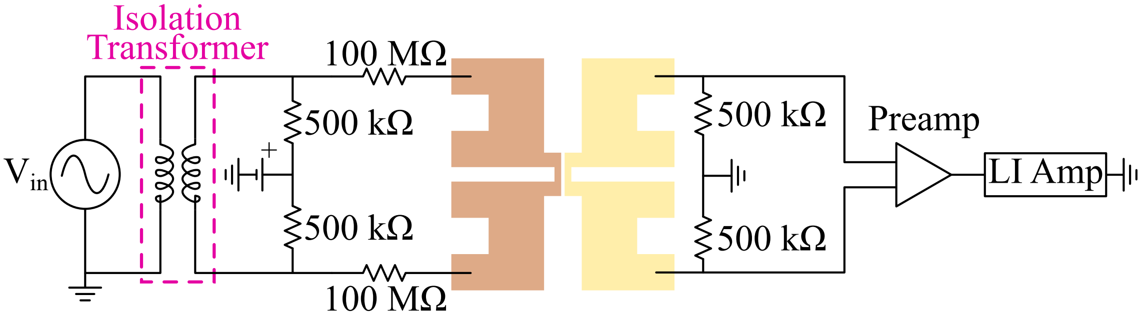

Figure F.1: The symmetric drive and layer potential difference circuit enables the generation of a potential difference between the two wires by applying a voltage at the location of the virtual ground on the drive side.

G

Appendix G: Summary of Drag Measurements Parameters

Parameters	**Values**
Average density	$n_e = 1.73 \times 10^{11}$ cm^{-2}
Combined mobility	$\mu_e = 798\,484$ cm^2/sV
Wire length	5 μm
Interwire leakage resistance	10 MΩ
Series resistance corrections	$R_{TOP} = 7846\ \Omega$; $R_{BOT} = 2850\ \Omega$
Base Temperature	15 mK
Input signal: Sinusoidal	$V_{in} = 0.3$ V$_{RMS}$ ($I_{in} = 1.5$ nA$_{RMS}$) at 54.32 Hz
PO gate voltages	TPO = -0.485 V; BPO = -0.815 V;
PL gate voltages	TPL = [-1.070, -0.654] V; BPL = -1.065 V

Table G.1: Summary of drag measurements parameters

H

Appendix H: Notes on Thermal Drag Theory

H.1 Thermal Transport in Quantum Wires

H.1.1 Thermal Conductance

In short quantum wires, the Wiedemann–Franz law was found to hold except in the $0.7 \times \frac{2e^2}{h}$ conductance plateau [119]. Thus, in the first subband of the quantum wire, we have

$$K_{QW}(T) = \frac{2\pi^2 k_B^2}{3h} T. \tag{H.1}$$

However, in a long quantum wire with a clean 1D subband, and in the absence of backscattering, Luttinger liquid behavior is expected. Spin–charge separation is predicted to modify the Wiedemann–Franz law. Indeed, the thermal conductance of a Luttinger liquid is given by

$$K_{LL}(T) = \frac{1}{Th}\sum_{n=1}^{N}\int_0^\infty d\epsilon \epsilon^2 \left(-\frac{\partial f_B}{\partial \epsilon}\right) t_n(\epsilon), \tag{H.2}$$

where $f_B = (\exp\{\epsilon/k_B T\} - 1)^{-1}$ is the Bose–Einstein distribution of plasmons, and $t_n(\epsilon)$ is the transmission probability of a plasmon through the nth mode of the Luttinger liquid [120]. Note that this thermal conductance still exhibits plateaus as the subband occupancy of the wire changes, but the height of these plateaus may depend on electron–electron interactions within certain temperature ranges.

H.1.2 Specific Heat

The specific heat of non-interacting fermions in one dimension is given by [61]

$$C_{QW}(T) \propto \frac{\pi T}{3 v_F}. \tag{H.3}$$

In contrast, for a Luttinger liquid with strong intrawire $1/r$ Coulomb interactions, there is a non-monotonic plasmon dispersion at finite momenta. The specific heat of such a system is expressed by Chou *et al.* in [121] as

$$C_{LL} = \frac{1}{\pi T^2}\int_{-\infty}^{\infty} dq \frac{\left[\omega_p(q)\right]^2 e^{\omega_p(q)/T}}{\left[e^{\omega_p(q)/T} - 1\right]^2}, \tag{H.4}$$

where $\omega_p(q) = v_F|q|\sqrt{1 + \frac{2e^2}{\pi v_F \kappa_{di}} K_0(|q| d_{QW})}$ is the plasmonic dispersion relation at momentum q, K_0 is the zeroth-order modified Bessel function of the second kind, κ_{di} is the dielectric constant of the material, and d_{QW} is the transverse width of the QW, which is necessary to avoid the singularity of the 1D Coulomb coupling [122].

It is found that the low-temperature suppression of the specific heat depends on the dimensionless parameter $\alpha = \frac{2e^2}{\pi v_F \kappa_{di}}$. Note that these results account only for the charge-sector contribution to the specific heat; additional contributions may arise from excitations outside the charge sector and from spinons, as discussed in [121].

H.2 Thermoelectric Drag

An electric field E generates an electrical current I^E and a thermal current I^T. Thus, the thermoelectric drag matrix for a pair of quantum wires is

$$\begin{bmatrix} E_1 \\ -\nabla T_1 \\ E_2 \\ -\nabla T_2 \end{bmatrix} = \begin{bmatrix} \rho_{11}^{EE} & \rho_{11}^{ET} & -\rho_{12}^{EE} & -\rho_{12}^{ET} \\ \rho_{11}^{TE} & \rho_{11}^{TT} & -\rho_{12}^{TE} & -\rho_{12}^{TT} \\ -\rho_{21}^{EE} & -\rho_{21}^{ET} & \rho_{22}^{EE} & \rho_{22}^{ET} \\ -\rho_{21}^{TE} & -\rho_{21}^{TT} & \rho_{22}^{TE} & \rho_{22}^{TT} \end{bmatrix} \begin{bmatrix} I_1^E \\ I_1^T \\ I_2^E \\ I_2^T \end{bmatrix}. \tag{H.5}$$

The terms ρ_{ii}^{EE} and ρ_{ii}^{TT} represent the electrical and thermal resistivities of a single wire, respectively. The cross terms ρ_{ii}^{ET} and ρ_{ii}^{TE} arise from thermoelectric effects within a wire; however, unless anharmonic interactions in the wire are non-negligible, these terms should vanish [115].

The upper-right part of this matrix can be expressed as

$$\begin{bmatrix} E_1 \\ -\nabla T_1 \end{bmatrix} = -\begin{bmatrix} \rho_{12}^{EE} & \rho_{12}^{ET} \\ \rho_{12}^{TE} & \rho_{12}^{TT} \end{bmatrix} \begin{bmatrix} I_2^E \\ I_2^T \end{bmatrix} = -\boldsymbol{\rho_{12}} \begin{bmatrix} I_2^E \\ I_2^T \end{bmatrix}, \tag{H.6}$$

with

$$\boldsymbol{\rho_{12}} = \int_0^\infty d\omega \int_0^\infty dk \frac{k^2 |U_{12}(k)|^2}{2\pi^2 k_B T} \frac{A_1(k,\omega) A_2(k,\omega)}{sinh^2\left(\frac{\omega}{2k_B T}\right)} \begin{bmatrix} \frac{1}{e^2 n_1 n_2} & \frac{3v_2}{\pi e n_1 k_B^2 T^2} \\ \frac{3v_1}{\pi e n_2 k_B^2 T} & \frac{9 v_1 v_2}{\pi^2 k_B^4 T^3} \end{bmatrix}, \tag{H.7}$$

where $A_i(k,\omega)$ is the spectral function of wire i, $U_{12}(k)$ is the interwire Coulomb coupling, and n_i and v_i denote the electron density and Luttinger velocity of wire i, respectively [114].

H.3 Wiedemann-Franz Law

The Wiedemann–Franz law states that the ratio of electrical to thermal conductivity in a system where both heat and charge currents are carried by the same particle or quasiparticle is directly proportional to temperature. The proportionality constant, known as the Lorenz constant, is $L_0 = \frac{\pi^2}{3}\left(\frac{k_B}{e}\right)^2$, where e is the charge of the carrier. Thus

$$\frac{\kappa}{\sigma} = L_0 T. \tag{H.8}$$

For the drag platform, an analogous Wiedemann–Franz-like relation can be defined as $\frac{K_{drag}}{G_{drag}} = L_{drag}T$, where L_{drag} is the drag Lorenz constant, $G_{drag} = \frac{1}{R_{drag}}$, and R_{drag} is the drag resistance, customarily defined as $R_{drag} = -\frac{V_{drag}}{I_{drive}}$. V_{drag} and I_{drive} are the measured voltage on the drag wire and the current sent in the drive wire, respectively. The drag Lorenz constant for parallel quantum wires was derived in Ref. [123] as

$$L_{drag} = \frac{\pi^2}{9}\frac{k_B^5 T^2}{e^2 n_1 n_2 v_1 v_2}. \tag{H.9}$$

References

[1] J. Bardeen, and W. H. Brattain, Three-electrode circuit element utilizing semiconductive materials, U.S. Patent No. 2524035A (Issued October 3, 1950).

[2] J. S. Kilby, Miniaturized electronic circuits, U.S. Patent No. 3138743A (Issued Febuary 6, 1959).

[3] K. S. Novoselov, A. K. Geim, S. V. Morozov, D. Jiang, Y. Zhang, S. V. Dubonos, I. V. Grigorieva, and A. A. Firsov, Electric Field Effect in Atomically Thin Carbon Films, Science **306**, 666 (2004).

[4] D. Hsieh, D. Qian, L. Wray, Y. Xia, Y. S. Hor, R. J. Cava, and M. Z. Hasan, A topological Dirac insulator in a quantum spin Hall phase, Nature **452**, 970 (2008).

[5] M. Greiner, I. Bloch, O. Mandel, T. W. Hänsch, and T. Esslinger, Exploring Phase Coherence in a 2D Lattice of Bose-Einstein Condensates, Phys. Rev. Lett. **87**, 160405 (2001).

[6] W. T. Sommer, Liquid Helium as a Barrier to Electrons, Phys. Rev. Lett. **12**, 271 (1964).

[7] F. D. M. Haldane, 'Luttinger liquid theory' of one-dimensional quantum fluids. I. Properties of the Luttinger model and their extension to the general 1D interacting spinless Fermi gas, J. Phys. C: Solid State Phys. **14**, 2585 (1981).

[8] D. C. Tsui, H. L. Stormer, and A. C. Gossard, Two-Dimensional Magnetotransport in the Extreme Quantum Limit, Phys. Rev. Lett. **48**, 1559 (1982).

[9] J. K. Jain, Composite-fermion approach for the fractional quantum Hall effect, Phys. Rev. Lett. **63**, 199 (1989).

[10] B. I. Halperin, P. A. Lee, and N. Read, Theory of the half-filled Landau level, Phys. Rev. B **47**, 7312 (1993).

[11] J. S. Meyer, and K. A. Matveev, Wigner crystal physics in quantum wires, J. Phys.: Condens. Matter **21**, 023203 (2009).

[12] M. Kim, A. Timmel, L. Ju, and X.-G. Wen, Topological chiral superconductivity beyond pairing in a Fermi liquid, Phys. Rev. B **111**, 014508 (2025).

[13] T. Han, *et al.*, Signatures of chiral superconductivity in rhombohedral graphene, Nature (2025).

[14] S.M. Cronenwett, Coherence, Charging and Spin Effects in Quantum Dots and Point Contacts, PhD thesis, Stanford University (2001)

[15] C. W. J. Beenakker, H. van Houten, Quantum Transport in Semiconductor Nanostructures, Solid State Physics **44**, 1 (1991).

[16] P. Mohanty, E. M. Q. Jariwala, and R. A. Webb, Intrinsic Decoherence in Mesoscopic Systems, Phys. Rev. Lett. **78**, 3366 (1997).

[17] C. Müller, J. Lisenfeld, A. Shnirman, and S. Poletto, Interacting two-level defects as sources of fluctuating high-frequency noise in superconducting circuits, Phys. Rev. B **92**, 035442 (2015).

[18] A. G. Huibers, J. A. Folk, S. R. Patel, C. M. Marcus, C. I. Duruöz, and J. S. Harris, Low-Temperature Saturation of the Dephasing Time and Effects of Microwave Radiation on Open Quantum Dots, Phys. Rev. Lett. **83**, 5090 (1999).

[19] E. Y. Andrei, *Two-Dimensional Electron Systems*, (Kluwer Academic Publishers, Dordrecht, 1997).

[20] Y. V. Sharvin, A Possible Method for Studying Fermi Surfaces, J. Exptl. Theoret. Phys. (U.S.S.R.) **48**, 984 (1965).

[21] H. van Houten, C. W. J. Beenakker, Quantum Point Contacts, Physics Today **49**, 22 (1996).

[22] D. A. Wharam, T. J. Thornton, R. Newbury, M. Pepper, H. Ahmed, J. E. F. Frost, D. G. Hasko, D. C. Peacockt, D. A. Ritchie and G. A. C. Jones, One-dimensional transport and the quantisation of the ballistic resistance, J. Phys. C: Solid State Phys. **23**, 209 (1988).

[23] B. J. van Wees, H. van Houten, C. W. J. Beenakker, J. G. Williamson, L. P. Kouwenhoven, D. van der Marel, and C. T. Foxon, Quantized conductance of point contacts in a two-dimensional electron gas, Phys. Rev. Lett. **60**, 848 (1988).

[24] R. Landauer, Spatial variation of currents and fields due to localized scatterers in metallic conduction, IBM Corp. **32**, 306 (1988).

[25] A. D. Stone, and A. Szafer, What is measured when you measure a resistance?—The Landauer formula revisited, IBM Corp. **32**, 384 (1988).

[26] E. Chatzikyriakou *et al.*, Unveiling the charge distribution of a GaAs-based nanoelectronic device: A large experimental dataset approach, Phys. Rev. Research **4**, 043163 (2022).

[27] E. Montie, *et al.*, Observation of the optical analogue of quantized conductance of a point contact. Nature **350**, 594 (1991).

[28] K. Delfanazari, *et al.*, Quantized conductance in hybrid split-gate arrays of superconducting quantum point contacts with semiconducting two-dimensional electron systems, Phys. Rev. Appl. **21**, 014051 (2024).

[29] H. van Houten, L. W. Molenkamp, C. W. J. Beenakker, and C. T. Foxon, Thermo-electric properties of quantum point contacts. Semicond. Sci. Technol. **7**, B215 (1992).

[30] K. J. Thomas, J. T. Nicholls, M. Y. Simmons, M. Pepper, D. R. Mace, and D. A. Ritchie, Possible Spin Polarization in a One-Dimensional Electron Gas. Phys. Rev. Lett. **77**, 135 (1996).

[31] A. P. Micolich, What lurks below the last plateau: experimental studies of the $0.7\times 2e^2/h$ conductance anomaly in one-dimensional systems, J. Phys.: Condens. Matter **23**, 443201 (2011).

[32] H. Steinberg, G. Barak, A. Yacoby, L. N. Pfeiffer, K. W. West, B. I. Halperin, and K. Le Hur, Charge fractionalization in quantum wires. Nature Physics **4**, 116 (2008).

[33] O. M. Auslaender, H. Steinberg, A. Yacoby, Y. Tserkovnyak, B. I. Halperin, K. W. Baldwin, L. N. Pfeiffer, and K. W. West, Spin-Charge Separation and Localization in One Dimension. Science **308**, 88 (2005).

[34] W. K. Hew, K. J. Thomas, M. Pepper, I. Farrer, D. Anderson, G. A. C. Jones, and D. A. Ritchie, Incipient Formation of an Electron Lattice in a Weakly Confined Quantum Wire. Phys. Rev. Lett. **102**, 056804 (2009).

[35] V. V. Deshpande, M. Bockrath, L. I. Glazman, and A. Yacoby, Electron liquids and solids in one dimension. Nature **464**, 209 (2010).

[36] P. Debray, V. Zverev, O. E. Raichev, R. Klesse, P. Vasilopoulos, and R. S. Newrock, Experimental studies of Coulomb drag between ballistic quantum wires. J. Phys.: Condens. Matter **13**, 3389 (2001).

[37] O. E. Raichev, Phonon-mediated drag between one-dimensional electron systems. Phys. Rev. B **64**, 035324 (2001).

[38] M. Yamamoto, M. Stopa, Y. Tokura, Y. Hirayama, and S. Tarucha, Coulomb drag between quantum wires: magnetic field effects and negative anomaly. Physica E **12**, 726 (2002).

[39] M. Yamamoto, M. Stopa, Y. Tokura, Y. Hirayama, and S. Tarucha, Negative Coulomb Drag in a One-Dimensional Wire. Science **313**, 204 (2006).

[40] M. Yamamoto, H. Takagi, M. Stopa, and S. Tarucha, Hydrodynamic rectified drag current in a quantum wire induced by Wigner crystallization. Phys. Rev. B **85**, 041308(R) (2012).

[41] D. Laroche, E.S. Bielejec, J.L. Reno, G. Gervais, and M.P. Lilly, Towards Coulomb drag in vertically coupled quantum wires with independent contacts. Physica E **40**, 1569 (2008).

[42] D. Laroche, G. Gervais, M. P. Lilly, and J. L. Reno, Positive and negative Coulomb drag in vertically integrated one-dimensional quantum wires. Nature Nanotech **6**, 793 (2011).

[43] D. Laroche, G. Gervais, M. P. Lilly, and J. L. Reno, 1D-1D Coulomb Drag Signature of a Luttinger Liquid. Science **343**, 631 (2014).

[44] R. Makaju, H. Kassar, S. M. Daloglu, A. Huynh, and D. Laroche, Nonreciprocal Coulomb drag between quantum wires in the quasi-one-dimensional regime. Phys. Rev. B **109**, 085101 (2024).

[45] M. Zheng, R. Makaju, R. Gazizulin, S. J. Addamane, and D. Laroche, Tunable reciprocal and nonreciprocal contributions to 1D Coulomb drag Nat. Commun., **16**, 6963 (2025).

[46] M. Zheng, R. Makaju, R. Gazizulin, A. Levchenko, S. J. Addamane, and D. Laroche, Quasi-1D Coulomb Drag in the Nonlinear Regime. Phys. Rev. Lett. **134**, 236301 (2025).

[47] A. Yu. Kitaev, Fault-tolerant quantum computation by anyons. Annals of Physics **303**, 2 (2003).

[48] L. D. Landau and E. M. Lifshitz, *Quantum Mechanics: Non-relativistic Theory*, (Pergamon Press, Oxford, 1991).

[49] L. I. Glazman and A. V. Khaetskii, Quantum conductance of a lateral microconstraint in a magnetic field, J. Phys.: Condens. Matter **1**, 5005 (1989).

[50] S. Datta, *Electronic Transport in Mesoscopic Systems*, (Cambridge University Press, Cambridge, 1995).

[51] R. de Picciotto, H. L. Stormer, L. N. Pfeiffer, K. W. Baldwin, and K. W. West, Four-terminal resistance of a ballistic quantum wire. Nature **411**, 51 (2001).

[52] E. Bielejec, J.L. Reno, S.K. Lyo, M.P. Lilly, Tunneling spectroscopy in vertically coupled quantum wires, Solid State Communications **147**, 79 (2008).

[53] V. Kumar, Y. Duo, P. See, J. P. Griffiths, D. A. Ritchie, I. Farrer, and S. Kumar, Correlation effects mediated by disorders in one-dimensional channels, Phys. Rev. B **112**, 035404 (2025).

[54] A. C. Mehta, C. J. Umrigar, J. S. Meyer, and H. U. Baranger, Zigzag Phase Transition in Quantum Wires, Phys. Rev. Lett. **110**, 246802 (2013).

[55] L. K. Saini,l K. Tankeshwar, and R. K. Moudgil, Dynamic correlations in coupled electron-electron and electron-hole quantum wire systems, Phys. Rev. B **70**, 075302 (2004).

[56] M. Reznikov, M. Heiblum, H. Shtrikman, and D. Mahalu, Temporal Correlation of Electrons: Suppression of Shot Noise in a Ballistic Quantum Point Contact, Phys. Rev. Lett. **75**, 3340 (1995).

[57] N. K. Patel, L. Martin-Moreno, M. Pepper, R. Newbury, J. E. F. Frost, D. A. Ritchie, G. A. C. Jones, J. T. M. B. Janssen, J. Singleton, and J. A. A. J. Perenboom, Ballistic transport in one dimension: additional quantisation produced by an electric field, J. Phys.: Condens. Matter **2**, 7247 (1990).

[58] N. K. Patel, J. T. Nicholls, L. Martin-Moreno, M. Pepper, J. E. F. Frost, D. A. Ritchie, and G. A. C. Jones, Evolution of half plateaus as a function of electric field in a ballistic quasi-one-dimensional constriction, Phys. Rev. B **44**, 13549 (1991).

[59] S. M. Cronenwett, H. J. Lynch, D. Goldhaber-Gordon, L. P. Kouwenhoven, C. M. Marcus, K. Hirose, N. S. Wingreen, and V. Umansky, Low-Temperature Fate of the 0.7 Structure in a Point Contact: A Kondo-like Correlated State in an Open System, Phys. Rev. Lett. **88**, 226805 (2002).

[60] S. M. Cronenwett, Coherence, Charging, and Spin Effects in Quantum Dots and Point Contacts, PhD thesis, Stanford university (2002)

[61] T. Giamarchi, *Quantum Physics in One Dimension*, (Clarendon Press, Oxford, 2003).

[62] S. I. Tomonaga, Remarks on Bloch's method of sound waves applied to many-fermion problems, Progr. Theor. Phys. **5**, 544 (1950).

[63] J. M. Luttinger, An exactly soluble model of a many-fermion system, J. Math. Phys. **4**, 1154 (1963).

[64] D. C. Mattis, and E. H. Lieb, Exact Solution of a Many-Fermion System and Its Associated Boson Field, J. Math. Phys. **6**, 304 (1965).

[65] F. D. M. Haldane, Effective Harmonic-Fluid Approach to Low-Energy Properties of One-Dimensional Quantum Fluids, Phys. Rev. Lett. **47**, 1840 (1981).

[66] P. M. T. Vianez *et al.*, Observing separate spin and charge Fermi seas in a strongly correlated one-dimensional conductor, Sci. Adv. **8**, eabm2781 (2022).

[67] M. Muhammad, Coulomb Drag Between One-Dimensional Electron Systems, PhD thesis, University of Cincinnati (2007).

[68] S. Tarucha, T. Honda, T. Saku, Reduction of quantized conductance at low temperatures observed in 2 to 10 μm-long quantum wires, Solid State Communications **94**, 413 (1995).

[69] D. L. Maslov, and M. Stone, Landauer conductance of Luttinger liquids with leads, Phys. Rev. B **52**, R5539 (1995).

[70] I. Safi, and H. J. Schulz, Transport in an inhomogeneous interacting one-dimensional system, Phys. Rev. B **52**, R17040 (1995).

[71] Y. Oreg, and A. M. Finkel'stein, dc transport in quantum wires, Phys. Rev. B **54**, R14265 (1996).

[72] M. I. Muradov, and V. L. Gurevich, On the temperature dependence of ballistic Coulomb drag in nanowires, J. Phys.: Condens. Matter **24**, 135304 (2012).

[73] G. A. Fiete, K. Le Hur, and L. Balents, Coulomb drag between two spin-incoherent Luttinger liquids, Phys. Rev. B **73**, 165104 (2006).

[74] R. Klesse and A. Stern, Coulomb drag between quantum wires, Phys. Rev. B **62**, 16912 (2000).

[75] P. Debray, V. N. Zverev, V. Gurevich, R. Klesse, and R. S. Newrock, Coulomb drag between ballistic one-dimensional electron systems, Semicond. Sci. Technol. **17**, R21 (2002).

[76] D. Laroche, Coulomb Drag in Vertically-Integrated One-Dimensional Quantum Wires, PhD thesis, McGill University (2013).

[77] C. Zhou and H. Guo, Coulomb drag between quantum wires: A nonequilibrium many-body approach, Phys. Rev. B **99**, 035423 (2019).

[78] A. P. Dmitriev, I. V. Gornyi, and D. G. Polyakov, Coulomb drag between ballistic quantum wires, Phys. Rev. B **86**, 245402 (2012).

[79] A. P. Dmitriev, I. V. Gornyi, and D. G. Polyakov, Ultranarrow resonance in Coulomb drag between quantum wires at coinciding densities, Phys. Rev. B **94**, 085404 (2016).

[80] T. Fuchs, R. Klesse, and A. Stern, Coulomb drag between quantum wires with different electron densities, Phys. Rev. B **71**, 045321 (2005).

[81] M. Pustilnik, E. G. Mishchenko, L. I. Glazman, and A. V. Andreev, Coulomb Drag by Small Momentum Transfer between Quantum Wires, Phys. Rev. Lett. **91**, 126805 (2003).

[82] D. N. Aristov, Luttinger liquids with curvature: Density correlations and Coulomb drag effect, Phys. Rev. B **76**, 085327 (2007).

[83] J. Peguiron, C. Bruder, and B. Trauzettel, Temperature Dependence of Coulomb Drag Between Finite-Length Quantum Wires, Phys. Rev. Lett. **99**, 086404 (2007).

[84] J. Peguiron, C. Bruder, and B. Trauzettel, Temperature Dependence of Coulomb Drag Between Finite-Length Quantum Wires, Phys. Rev. Lett. **99**, 086404 (2007).

[85] A. Levchenko, and A. Kamenev, Coulomb Drag in Quantum Circuits, Phys. Rev. Lett. **101**, 216806 (2008).

[86] R. Sánchez, R. López, D. Sánchez, and M. Büttiker, Mesoscopic Coulomb Drag, Broken Detailed Balance, and Fluctuation Relations, Phys. Rev. Lett. **104**, 076801 (2010).

[87] M. Faraday, *Experimental Researches in Chemistry and Physics*, (R. Taylor and W. Francis, London, 1959).

[88] E. Torricelli, *Opera Geometrica Evangelistae Torricellii*, (typis A. Masse & L. de Landis, Florentiae, 1644).

[89] O. von Guericke, *Experimenta Nova (ut vocantur) Magdeburgica de Vacuo Spatio*, (J. Jansson à Waesberge, Amsterdam, 1672).

[90] F. Pobell, *Matter and methods at low temperatures*, (Springer-Verlag, New York, 1992).

[91] Oxford Instrument, *Triton Cryofree Dilution Refrigerator: Principles of Operation*, (Oxford Instruments Nanotechnology Tools Ltd, Tubney Woods, 2016).

[92] J. A. Hedberg, Low Temperature Force Microscopy on a Deeply Embedded two Dimensional Electron Gas, PhD thesis, McGill University (2011).

[93] G. Ventura, and L. Risegari, *The art of cryogenics : low-temperature experimental techniques*, (Elsevier, Amsterdam, 2008).

[94] H. J. Pain, *The Physics of Vibration and Waves*, (John Wiley & Sons Ltd, West Sussex, 2005).

[95] C. W. Silva, *Vibration*, (Taylor & Francis Group, Boca Raton, 2006).

[96] K. P. Menard, *Dynamic Mechanical Analysis*, (Taylor & Francis Group, Boca Raton, 2008).

[97] C. R. Dean, A Study of the Fractional Quantum Hall Energy Gap at Half Filling, PhD thesis, McGill University (2008)

[98] C. T. Van Degrift, Coin silver as a construction material in low-temperature experiments, Physica B+C. **107**, 605 (1981).

[99] Copper.org, “C10200”, https://alloys.copper.org/alloy/C10200

[100] F. Fickett, Oxygen-free Copper at 4 K: Resistance and magnetoresistance, IEEE. **19**, 228 (1983).

[101] NIST, “Material Properties: OFHC Copper (UNS C10100/C10200)”, https://trc.nist.gov/cryogenics/materials/OFHC%20Copper/OFHC_Copper_rev1.htm

[102] R. C. Weast, M. J. Astle, and W. H. Beyer, *Handbook of chemistry and physics*, (CRC Press, Boca Raton, 1983).

[103] L. A. Hall, *Survey of Electrical Resistivity Measurements on 16 Pure Metals In the Temperature Range to 273°K*, (National Bureau of Standards, Boulder, 1968).

[104] K. Mendelssohn, and H. M. Rosenberg, The Thermal Conductivity of Metals at Low Temperatures I: The Elements of Groups 1, 2 and 3, Proc. Phys. Soc. A. **65**, 385 (1952).

[105] D. R. Smith, and F. R. Fickett, Low-Temperature Properties of Silver, J. Res Natl. Inst. Stand. Technol. **100**, 119 (1995).

[106] W. H. Warren, and W. G. Bader, Superconductivity Measurements in Solders Commonly Used for Low Temperature Research, Rev. Sci. Instrum. **40**, 180 (1969).

[107] Sandia National Laboratories, The Giants of The NuclearTesting Era: The works of Willis Whitfield, Sandia National Laboratories (2018).

[108] M.V. Weckwerth, J.A. Simmons, N.E. Harff, M.E. Sherwin, M.A. Blount, W.E. Baca, and H.C. Chui, Epoxy bond and stop-etch (EBASE) technique enabling backside processing of (Al)GaAs heterostructures, Superlattices and Microstructures **20**, 561 (1996).

[109] B. Schmidt, Specific Heat in the fractional Quantum Hall Regime, PhD thesis, McGill University (2019)

[110] K. Nikolić, and A. MacKinnon, Conductance and conductance fluctuations of narrow disordered quantum wires, Phys. Rev. B **50**, 11008 (1994).

[111] P.L. McEuen, B.W. Alphenaar, R.G. Wheeler, and R.N. Sacks, Resonant transport effects due to an impurity in a narrow constriction, Surface Science **229**, 312 (1990).

[112] B. N. Narozhny, and A. Levchenko, Coulomb Drag, Rev. Mod. Phys. **88**, 025003 (2016).

[113] A. C. Graham, M. Pepper, M. Y. Simmons, and D. A. Ritchie, Anomalous spin-dependent behavior of one-dimensional subbands. Phys. Rev. B **72**, 193305 (2005).

[114] G. Chiriacò, Thermal drag between two coupled quantum wires, PhD thesis, Università Di Pisa (2015)

[115] C. L. Kane, and M. P. A. Fisher, Thermal Transport in a Luttinger Liquid. Phys. Rev. Lett. **76**, 3192 (1996).

[116] N. Wakeham, A. F. Bangura, X. Xu, J.-F. Mercure, M. Greenblatt, and N. E. Hussey, Gross violation of the Wiedemann–Franz law in a quasi-one-dimensional conductor. Nat. Commun. **2**, 396 (2011).

[117] M. Büttiker and R. Sánchez, A closer look at charge drag. Nat. Nano. **6**, 757 (2011).

[118] H. E. W. Montagu, Interactions effects in weakly confined quasi one-dimensional quantum wire, PhD thesis, University College London (2016)

[119] J.T. Nicholls, and O. Chiatti, Thermal measurements of a one-dimensional wire in the quantum limit. J. Phys.: Condens. Matter. **20**, 164210 (2008).

[120] I. V. Krive, I. A. Romanovsky, E. N. Bogachek, A. G. Scherbakov, and U. Landman, Thermoelectric effects in a Luttinger liquid. Low Temp. Phys. **27**, 821 (2001).

[121] Y. Z. Chou, and S. Das Sarma, Nonmonotonic plasmon dispersion in strongly interacting Coulomb Luttinger liquids. Phys. Rev. B. **7**, 075430 (2020).

[122] S. Das Sarma, and W. Lai, Screening and elementary excitations in narrow-channel semiconductor microstructures. Phys. Rev. B. **32**, 1401 (1985).

[123] B. Bhandari, G. Chiriacò, P. A. Erdman, R. Fazio, and F. Taddei, Thermal drag in electronic conductors. Phys. Rev. B. **98**, 035415 (2018).